

ACTIVATION OF METAL NANOPARTICLE/POLYMER SYSTEMS VIA
PHOTOTHERMAL EFFECT TO DEVELOP SHAPE MEMORY POLYMERS



by
Merve Seyhan

Submitted to Graduate School of Natural and Applied Sciences
in Partial Fulfillment of the Requirements
for the Degree of Doctor of Philosophy in
Chemical Engineering

Yeditepe University
2016

ACTIVATION OF METAL NANOPARTICLE/POLYMER SYSTEMS VIA
PHOTOTHERMAL EFFECT TO DEVELOP SHAPE MEMORY POLYMERS

APPROVED BY:

Assoc. Prof. Dr. Seyda Malta

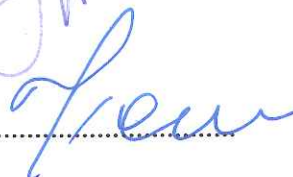
(Thesis Supervisor)


.....

Prof. Dr. Ebru Toksoy Öner


.....

Prof. Dr. Tarık Eren


.....

Prof. Dr. Zoya Tuiebekhova


.....

Assist. Prof. Dr. Erde Can


.....

DATE OF APPROVAL: ... / ... / ...

ACKNOWLEDGEMENTS

It is been a long journey since I had started my graduate education. There are lots of valuable people who walked with me during these years. First and foremost I would like to thank my advisor, Dr. Seyda Malta. 7 years ago, I would never have guessed that we could be a 'team' whereas now I can clearly see that, her presence always motivated me to look forward and believe not only in my work, but also in myself. She taught me how to be a tough scientist and a good teacher. I consider myself lucky to have the chance to work with her.

Words are not enough to express my feelings to Dr. Nihat Baysal and Dr. Deniz Rende. They have been my family in both Yeditepe and RPI since my last year at undergraduate education. I will always be grateful to them for their endless support, guidance, insight, kindness and friendship. If I am a successor today, it is because I got the chance to work with them. Another important person that I would like to mention is Dr. Rahmi Özişik. It was an excellent experience to study with his research group. I really owe a huge debt of gratitude to him for giving me the chance to work in RPI and use all its facilities. I would not be able to get my PhD without these four brilliant scientists.

10 years of studies in Yeditepe University gave me unforgettable memories, experiences and virtues that I will always be proud of. I enjoyed every single day of 10 years thanks to all present and former members of ChBE department. It was an honor for me to be in same the community with them. My colleagues and professors in Yeditepe will never be forgotten. I would like to thank, in particular, to Dr. Zoya Tuiebekhova and Dr. Ebru Toksoy Oner for their valuable feedback throughout my studies. As well as the important collaborations I had throughout my graduate career, the graduate and undergraduate students who helped me during my thesis are also very special. Dearest thanks to Ecem Yarar and Büge Yilmazer for Chapter 4; Berna Gürten and Nuran Fatoğlu for Chapter 5; Katherine Rickard for Chapter 6; Sera Erkeçoğlu for Chapter 7.

As the years go, there are only few people left to whom I can always lean on. No matter the distances, these people will be my lifelong friends without a doubt. Special thanks to

my special two; Burcu Erdoğan and Duygu Tecimođlu. I don't know if anybody else can complete my sentences except you two. Also I would like to send my bests to those great people not only classmate, home mate or colleague, but also a part of my family; Zeynep İyigündođdu, Cem Levent Altan and Ece Atlan. Last by not least, I am grateful for having Çađıl Arık, Ceren Akyol and Seçil Kavas in my life. I am so lucky that we all 'grew up' together and will be always side by side.

Although I was never good enough to make myself clear to them, my gratefulness for my mother and father will never end. I deeply thank them for always being there for me. To my fiancé Ahmet; I sincerely thank you for teaching me how to appreciate life and love somebody in all circumstances. Finally, I am very lucky to have the goofiest cat ever, Lokum. His presence always gives energy to me even though he is never aware of it. This work of mine is dedicated to my family.

ABSTRACT

ACTIVATION OF METAL NANOPARTICLE/POLYMER SYSTEMS VIA PHOTOTHERMAL EFFECT TO DEVELOP SHAPE MEMORY POLYMERS

Nanoparticles, known to have superior properties; are considered in a wide range of applications in the field of photonics, optoelectronics, biological and magnetic practices. Photothermal effect due to surface plasmon resonance in metal nanoparticles has become a great interest to be used for several applications in many disciplines. It is possible to find biological studies taking advantage of this effect in aqueous environment. However, there exist only a few interested in tracking and controlling the local temperature profile in solid medium. Although the morphology and crystallinity of polymers can be governed, in situ, via altering the heat released from photoexcitation of metal nanoparticles. In this work, remote actuation of metal, in particular gold and silver, nanoparticles is aimed to be investigated. The local temperature change due to photothermal heating of gold nanoparticles in poly (ethylene oxide) was followed with using fluorescence probes as thermal sensors. On the other hand, a method is proposed to study Raman crystallinity as a function of temperature using the conformational changes in poly (ethylene oxide). Gold nanoparticles are heated by photothermal effect to actuate magnetite doped poly (DL-lactide-co-glycolide); which is a shape memory polymer, and multi stages of shape memory schemes were successfully achieved. At the same time, the influence of gold and silver nanoparticles (at diameter of 10 and 30 nm) on thermal and mechanical properties of polymers was studied. The mechanical properties of poly (ethylene oxide) were found to be enhanced with addition of nanoparticles regardless of the nanoparticle type and size. However, the increase in stiffness and strength of poly (ethylene oxide) reached a plateau above a certain concentration, which is attributed to nanoparticle agglomerations. Finally, the effect of silver nanoparticles on the thermal conductivity of water, ethylene glycol and hexane was investigated. The thermal conductivity of different base fluids such as hexane and ethylene glycol was found to increase upon addition of silver nanoparticles whereas, the results for water measurements was contradictory. Although, this result can be correlated with interfacial thermal resistance and viscosity of the nanofluid, the deterioration in thermal conductivity of water cannot be fully explained.

ÖZET

ŞEKİL HAFIZALI POLİMERLERİN GELİŞTİRİLMESİ İÇİN METAL NANOPARÇACIK/POLİMER SİSTEMLERİNİN FOTOTERMAL ETKİ İLE AKTİFLEŞTİRİLMESİ

Nanoparçacıklar üstün özellikleri ile bilindiği için, fotonik, optoelektronik, biyolojik ve manyetik uygulamalarda değerlendirilmek üzere tavsiye edilir. Metal nanoparçacıklardaki yüzey plazmon rezonansına bağlı oluşan fototermal etki, bir çok disiplinde çeşitli uygulamalarda kullanılmak üzere ilgi çekmiştir. Bu etkinin sulu ortamlarda kullanımını biyolojik çalışmalarla bulmak mümkündür. Ancak, bu çalışmaların katı ortamlarda yerel sıcaklık profilinin takibi ve kontrolüyle ilgilenen miktarı azdır. Oysa ki, metal nanoparçacıkların fotoeksitasyonundan oluşan ısının değiştirilmesiyle polimer morfolojisi ve kristalliliği, yerinde kontrol edilebilir. Bu çalışmada metal, özellikle altın ve gümüş, nanoparçacıkların uzaktan harekete geçirilmesinin incelenmesi amaçlanmıştır. Poli (etilen oksit) içerisindeki altın nanoparçacıklarının fototermal ısınmasından dolayı oluşan yerel sıcaklık değişimi, termal sensör olarak floresan probu kullanımıyla takip edilmiştir. Öte yandan, Raman kristalliliğinin sıcaklığa bağlı bir fonksiyonu olarak çalışılması için poli (etilen oksit)'in içerisindeki biçimsel değişikliklerin kullanıldığı bir metod önerilmiştir. Altın nanoparçacıklar, bir şekil hafızalı polimer olan magnetit doldurulmuş poli (DL-laktit-ko-glikolit)'in harekete geçirilmesi için fototermal etki ile ısıtılmış ve çok aşamalı şekil hafıza şemalarına başarıyla ulaşılmıştır. Aynı zamanda, (10 ve 30 nm çapındaki) altın ve gümüş nanoparçacıkların polimerlerin termal ve mekanik özelliklerine olan etkileri çalışılmıştır. Nanoparçacıkların, poli (etilen oksit)'in mekanik özelliklerini, eklenen nanoparçacığın tipine ve boyutuna bakılmaksızın, iyileştirdiği bulunmuştur. Ancak polimerin sertliği ve dayanıklılığındaki artışın belli bir konsantrasyondan sonra platoya ulaştığı gözlemlenmiş, bu da nanoparçacık kümeleşmelerine bağlanmıştır. Son olarak, gümüş nanoparçacıklarının su, etilen glikol ve hekzanın termal iletkenliğine olan etkisi araştırılmıştır. Gümüş nanoparçacıkların eklenmesiyle beraber hekzan ve etilen glikolün termal iletkenliğinde artış bulunmuştur, ancak sonuçlar su ölçümlerinde karşıttır. Bu sonuç arayüzey termal rezistansı ve nanoakışkan vizkozitesi ile bağdaştırılabilir, ancak suyun termal iletkenliğindeki bozulma tamamen açıklanamaz.

TABLE OF CONTENTS

ACKNOWLEDGEMENTS.....	iii
ABSTRACT.....	v
ÖZET.....	vi
TABLE OF CONTENTS.....	vii
LIST OF FIGURES.....	xi
LIST OF TABLES.....	xvi
LIST OF SYMBOLS AND ABBREVIATIONS.....	xvii
1. VISION.....	1
2. GOLD AND SILVER NANOPARTICLES.....	2
2.1. INTRODUCTION.....	2
2.2. SYNTHESIS OF NANOPARTICLES.....	3
2.3. EXPERIMENTAL.....	9
2.3.1. Hydrophilic Nanoparticle Synthesis and Characterization.....	10
2.3.2. Hydrophobic Nanoparticle Synthesis and Characterization.....	10
2.4. RESULTS AND DISCUSSION.....	13
2.4.1. Hydrophilic Nanoparticles.....	13
2.4.2. Hydrophobic Nanoparticles.....	14
2.4.2.1. Size Distribution of Au10/o and Ag10/o Nanoparticles.....	14
2.4.2.2. Thermogravimetric Analysis of Au10/o and Ag10/o Nanoparticles.....	15
2.4.2.3. Fourier Transform Infrared Spectroscopic Analysis of Au10/o and Ag10/o Nanoparticles.....	16
2.4.2.4. Size Distribution of Au30/o and Ag30/o Nanoparticles.....	19
2.5. CONCLUSION.....	21
3. NANOCOMPOSITES PREPARED WITH GOLD AND SILVER NANOPARTICLES.....	23
3.1. INTRODUCTION.....	23
3.2. APPLICATIONS OF NANOCOMPOSITES.....	24
3.3. PREPARATION ROUTES FOR POLYMER NANOCOMPOSITES.....	27
3.3.1. Physical Methods.....	27

3.3.2. Chemical Methods	29
3.4. EXPERIMENTAL	30
3.5. RESULTS AND DISCUSSION	31
3.6. CONCLUSION	37
4. MECHANICAL AND THERMAL PROPERTIES OF PEO/AU AND PEO/AG NANOCOMPOSITES	38
4.1. INTRODUCTION	38
4.2. THERMOMECHANICAL PROPERTIES OF POLYMERS	39
4.2.1. Tensile Properties	40
4.2.2. Viscoelastic Properties	42
4.2.3. Melting and Glass Transition Temperature	45
4.2.4. Crystallinity of Polymers	46
4.3. EXPERIMENTAL	49
4.4. RESULTS AND DISCUSSION	50
4.4.1. Stress vs. Strain Curves for PAu10-30 and PAg10-30 Nanocomposites .	50
4.4.2. Glass Transition Temperature Measurements for PAu10 and PAg10 Nanocomposites	57
4.4.3. Crystallinity Measurements for PAu10 and PAg10 Nanocomposites	60
4.5. CONCLUSION	62
5. THE EFFECT OF FUNCTIONALIZED SILVER NANOPARTICLES OVER THE THERMAL CONDUCTIVITY OF BASE FLUIDS	64
5.1. INTRODUCTION	63
5.2. NANOFLUIDS	65
5.2.1. Preparation of Nanofluids	65
5.2.1.1. Two-Step Method	66
5.2.1.2. One-Step Method	68
5.2.2. Heat Transfer in Nanofluids	68
5.2.3. Theoretical Thermal Conductivity Models for Nanofluids	71
5.3. EXPERIMENTAL	72
5.4. RESULTS AND DISCUSSION	73
5.4.1. Enhanced Effective Thermal Conductivity for Hex/Ag and EG/Ag Nanofluids	74
5.4.2. Deterioration in Effective Thermal Conductivity of DW/Ag Nanofluids ..	77

5.4.3. Temperature Dependency Comparison for Hex/Ag, EG/Ag and DW/Ag Nanofluids	81
5.5. CONCLUSION	83
6. MEASUREMENT OF TEMPERATURE AND CRYSTALLINITY THROUGH CONFORMATIONAL AND STRUCTURAL CHANGES IN PEO VIA RAMAN SPECTROSCOPY	85
6.1. INTRODUCTION	85
6.2. RAMAN SPECTROSCOPY BASICS AND APPLICATIONS	86
6.2.1. Raman Scattering	86
6.2.2. Applications of Raman Spectroscopy to the Study of Polymers	87
6.3. EXPERIMENTAL	90
6.4. RESULTS AND DISCUSSION	91
6.5. CONCLUSION	98
7. ACTIVATION OF GOLD NANOPARTICLE/POLYMER SYSTEMS VIA PHOTOTHERMAL EFFECT TO DEVELOP SHAPE MEMORY POLYMERS.....	100
7.1. INTRODUCTION	100
7.2. PHOTOTHERMAL EFFECT.....	101
7.3. SHAPE MEMORY POLYMERS (SMP)	103
7.3.1. Shape Memory Effect (SME)	103
7.3.2. Magnetic Nanocomposites with SME.....	104
7.4. EXPERIMENTAL	105
7.4.1. Preparation of Polymer Nanofilms with Perylene	105
7.4.2. Investigation of Local Temperature Profiles Induced by Photothermal Effect in Metal Nanoparticle/Polymer Nanocomposites via Fluorescence Spectrophotometry.....	106
7.4.3. Preparation of Shape-Memory Polymers (SMP) and Activation with Heat	107
7.4.4. Activation of Shape-Memory Polymers (SMP) with Gold Nanoparticles	109
7.5. RESULTS AND DISCUSSION	110
7.5.1. Fluorescence Experiments	110
7.5.1.1. Fluorescence Experiments with Neat PEO	112
7.5.1.2. Fluorescence Experiments with PAu10-0.1 and PAu10-1	113

7.5.2. Shape Memory Experiments..... 117

 7.5.2.1. Activation of PDLLA/Magnetite Nanofilms with Heat..... 117

 7.5.2.2. Activation of PDLLA/Magnetite/Au Nanofilms with Laser
 Irradiation..... 119

7.6. CONCLUSION 121

8. CONCLUDING REMARKS 123

REFERENCES 124



LIST OF FIGURES

Figure 2.1. Formation mechanism of Au NPs with various particle sizes and shapes by chemical reduction method	4
Figure 2.2. TEM images of larger nanoparticles prepared from seed: (a) 5.5 ± 0.6 ; (b) 8 ± 0.8 ; (c) 17 ± 2.5 ; (d) 37 ± 5 nm after separation of nanorods.....	6
Figure 2.3. The formation of BH^4 capped Ag NP illustrated by Salomon et al.	8
Figure 2.4. (a) Gold particles formation process using oleylamine; (b) TEM images of Au NPs after 180 min; (c) The hydrogen bonding network formed between oleylamine ligands as a protecting layer on the gold nanoparticles	9
Figure 2.5. (a) TEM images and (b) Size distribution of Ag ₁₀ /w NPs synthesized in water (Green route synthesis)	13
Figure 2.6. (a) Particle size distribution; (b) Extinction measurement of NPs; representative TEM images of (c) Au ₁₀ /o (red bars) and (d) Ag ₁₀ /o (black bars) nanoparticles.....	14
Figure 2.7. TGA plots of Au ₁₀ /o, Ag ₁₀ /o NP samples and oleylamine/oleic acid (1:1 v/v) mixture	14
Figure 2.8. FTIR spectra of oleylamine, oleic acid, Au and Ag NPs	16
Figure 2.9. (a) Chemical formulations of oleylamine, oleic acid; (b) Representative image of oleylamine and oleic acid capped nanoparticle	18
Figure 2.10. (a) Particle size distribution; representative TEM images of (b) Au ₃₀ /o (black bars) and (c) Ag ₃₀ /o (red bars)	19

Figure 2.11. UV Extinction Spectra for (a) Au10/o and Au30/o; (b) Ag10/o and Ag30/o NPs	20
Figure 3.1. (a) Schematic of agglomerated nanoparticles dispersed in polymer matrix; (b) TEM micrographs of Aerosil® R8200 agglomerations in methylmethacrylate (MMA)	26
Figure 3.2. Preparation methods for nanocomposites; (a) Melt processing; (b) Film casting.....	28
Figure 3.3. Images of prepared nanofilms; (a) PAu10-0.01, (b) PAu10-0.1, (c) PAu10-1, (d) PAg10-0.01, (e) PAg10-0.1, (f) PAg10-1.....	33
Figure 3.4. TEM images for (a) PAu10-0.01 and (b) PAg10-0.01 nanofilms	34
Figure 3.5. ESEM images for (a) PAu10-1 and (b) PAg10-1 nanofilms	34
Figure 3.6. FTIR spectra of PAu10-0.1, PAg10-0.1 and neat PEO	36
Figure 4.1. Illustration of typical tensile sample	41
Figure 4.2. (a) The stress-strain behavior for brittle (curve A), plastic (curve B) and highly elastic (elastomeric) (curve C) polymers; (b) Schematic stress-strain curve for a plastic polymer	42
Figure 4.3. Representation of an arbitrary strain function and resulting stress response of a viscoelastic material	44
Figure 4.4. Specific volume vs. temperature plots upon cooling from the liquid melt for totally amorphous (A), semicrystalline (B) and crystalline (C) polymers	46
Figure 4.5. The schematic representation of (a) The chain folded structure; (b) Spherulite.....	48

Figure 4.6. Schematic illustration of DSC experimental procedure	50
Figure 4.7. (a) Stress vs. strain curve for neat PEO; (b) Elastic part of the stress vs. strain curve of neat PEO	51
Figure 4.8. Representative plots showing stress strain behavior for (a) PAu10 and (b) PAg10 nanocomposites at different concentrations	53
Figure 4.9. Representative plots showing stress strain behavior for (a) PAu30 and (b) PAg30 nanocomposites at different concentrations	54
Figure 4.10. Compliance as a function of nanoparticle concentration for PAu and PAg nanofilms	56
Figure 4.11. Temperature scan experiment for neat PEO	58
Figure 4.12. Per cent crystallinity of nanocomposites as a function of NP concentration	62
Figure 5.1. TEM images of (a) Citrate stabilized Au NPs (two-step method); (b) PVP stabilized Ag NPs (one-step method)	67
Figure 5.2. Modes of energy transfer in nanofluid systems	70
Figure 5.3. Thermal conductivity of (a) Hex/Ag10 and (b) EG/Ag10 nanofluids at different concentrations as a function of temperature.....	75
Figure 5.4. Relative thermal conductivities of Ag10/o NPs in hexane and Ag10/w NPs in ethylene glycol at 20 °C	76
Figure 5.5. Thermal conductivity of Ag10/w NPs dispersed in water at different concentrations as a function of temperature.	78

Figure 5.6. Relative thermal conductivity of Ag10/w NPs in water	79
Figure 5.7. Temperature dependency of effective thermal conductivity of nanofluids ..	82
Figure 6.1. Schematic representation of an induced dipole and resultant scattered light	86
Figure 6.2. Raman spectra of PEO at various temperatures	89
Figure 6.3. Raman spectrum was collected during second and third heating steps	90
Figure 6.4. Molecular model of PEO with helical symmetry.....	91
Figure 6.5. Raman spectra of PEO collected from 30 °C to 70 °C	92
Figure 6.6. (a) Parameters defined in Lorentzian peak function; (b) Lorentzian curve fit to Raman spectra of PEO at 30 °C and 70 °C	95
Figure 6.7 Normalized peak intensities recorded from 30 °C to 70 °C	96
Figure 6.8. Intensity of (a) Trans and (b) Gauche peaks as a function of temperature ...	97
Figure 6.9. Raman crystallinity index of neat PEO as a function of temperature	98
Figure 7.1. Schematic of surface plasmon resonance manifested by metal nanoparticles	102
Figure 7.2 Shape memory effect	103
Figure 7.3. Neat PEO, PAu10-0.1 and PAu10-1 nanofilms are exposed to green light from a distance of 2 cm. (a) PEO chains (red) dispersed with Au NPs (blue); (b) After irradiation, NPs will provide effective heating and cause the movement of polymer chains and melting eventually.....	107

Figure 7.4. Fluorescence spectrums and peak locations for (a) Perylene solution; (b) Neat PEO; (c) PAu10-0.1 and (d) PAu10-1 at room temperature	110
Figure 7.5. Fluorescence amplitude ratios of trough to peak for static and photothermal heating of neat PEO	113
Figure 7.6. The conventional and photothermal heating of PAu10-0.1 and PAu10-1 nanofilms	114
Figure 7.7. Fluorescence ratios for static and photothermal heating of neat PEO, PAu10-0.1 and PAu10-1	116
Figure 7.8. Shape memory behavior of PMag nanofilms	117
Figure 7.9. The process of shape memory recovery of PMag2.5; (a) Permanent shape of PMag2.5 at room temperature; (b) Folded shape of PMag2.5 at $T < 70\text{ }^{\circ}\text{C}$; (c) PMag2.5 recovers its shape at $T > 70\text{ }^{\circ}\text{C}$	118
Figure 7.10. The process of shape memory recovery of PMag5; (a) Permanent shape of PMag5 at room temperature; (b) Folded shape of PMag5 at $T < 70\text{ }^{\circ}\text{C}$; (c) PMag2.5 recovers its shape at $T > 70\text{ }^{\circ}\text{C}$	119
Figure 7.11. Shape memory behavior of PMag5-Au5% irradiated with green laser	120
Figure 7.12. The process of shape memory recovery of PMag5-Au5%; (a) Folded shape of PMag5-Au5% at $T < 70\text{ }^{\circ}\text{C}$; (b) PMag5-Au5% could not recover its shape at $65\text{ }^{\circ}\text{C}$; (c) Shape recovery completed after 30 min of irradiation at $65\text{ }^{\circ}\text{C}$	121

LIST OF TABLES

Table 2.1.	Vibrational mode assignments for oleylamine (Oamine), oleic acid (Oacid), Au and Ag NPs	17
Table 2.2.	The summary of abbreviations and results used for Au and Ag nanoparticles synthesized in this study.....	21
Table 3.1.	List of prepared PEO nanocomposites at different concentrations	31
Table 4.1.	Isothermal DMA results.....	55
Table 4.2.	Glass transition temperature and loss factor data for nanocomposites	59
Table 4.3.	Melting temperature, enthalpy and per cent crystallinity data for nanocomposites.....	61
Table 5.1.	Theoretical thermal conductivity values for some metals & metal oxides and common heat transfer fluids at 25 °C	65
Table 5.2.	Prepared nanofluids for thermal conductivity experiments.....	73
Table 5.3.	Viscosity measurements for gum arabic / water solutions	83
Table 6.1.	Raman bands for crystalline and melt states of PEO	93
Table 7.1.	List of peaks evaluated for fluorescence experiments	112

LIST OF SYMBOLS / ABBREVIATIONS

A	Area
A_0	Original cross-sectional area of the gage region
C_p	Centipoise
\bar{C}	Mean speed
\hat{C}_V	Heat capacity per unit volume
$\hat{C}_{V, NP}$	Heat capacity of nanoparticle per unit volume
d	Diameter
D	Diffusion constant
E	Young's modulus
E'	Storage modulus
E''	Loss modulus
f	Frequency
f	Volume fraction
F	Static force
h	Equivalent thickness
h	Heat transfer coefficient
I	Intensity
I_a	Raman intensity of amorphous portions
I_c	Raman intensity of crystalline portions
J	Tensile compliance
J_u	Net energy flux
k	Thermal conductivity
k_B	Boltzmann constant
k_{BF}	Thermal conductivity of base fluid
k_{eff}	Effective thermal conductivity
k_{NP}	Thermal conductivity of nanoparticle
l	Path length

L	Length
L_0	Narrow region of the tensile specimen
M	Total mass
M_a	Mass of amorphous chains
M_c	Mass of crystalline chains
r	Rocking
r_p	Radius of the particle
R	Interfacial thermal resistance
t	Time
T	Temperature
T_{BF}	Temperature of base fluid
T_f	Final temperature
T_g	Glass transition temperature
T_m	Melting temperature
T_{NP}	Temperature of nanoparticle
T_{trans}	Transition temperature
\bar{v}	Mean speed
w	Wagging
w	Width of Raman peak
x_c	Intensity of Raman peak
X_c	Per cent crystallinity
$(X_c)_R$	Raman crystallinity index
y_c	Wavelength of Raman peak
γ	Ratio of nanoparticle radius to equivalent thickness
δ	Bending
δ	Phase angle
δ_T	Thickness of thermal boundary layer
ΔH_m	Heat of melting
ΔL	Change in sample gage length

ε	Engineering strain
ε^0	Amplitude of applied strain
λ	Wavelength
η	Viscosity
ρ	Density
ρ_a	Density of totally amorphous sample
ρ_c	Density of totally crystalline sample
σ	Engineering stress
σ^0	Amplitude of stress response
σ_y	Yield strength
τ	Torsion
ν	Stretching
ν_0	Frequency of incident light
ψ	Sphericity
ω	Angular frequency of oscillations
Φ	Fractional crystallinity
CNT	Carbon nanotube
DLS	Dynamic light scattering
DMA	Dynamic mechanical analysis
DSC	Differential scanning calorimetry
EG	Ethylene glycol
EM	Electromagnetic wave
EMT	Effective medium theory
ESEM	Environmental scanning electron microscopy
FTIR	Fourier transform infrared spectroscopy
$^1\text{H-NMR}$	Proton nuclear magnetic resonance
CTAB	Cetyltrimethylammonium bromide
LCE	Liquid crystal elastomer
NP	Nanoparticle

PDLLA	poly (DL-lactide-co-glycolide)
PEO	poly (ethylene oxide)
PMMA	poly (methylmethacrylate)
P-NIPAAM	poly (N-isopropylacrylamide)
ppm	Pound per minute
PS	polystyrene
PU	polyurethane
PVA	poly (vinyl alcohol)
PVP	poly(vinyl pyrrolidone)
rpm	Rounds per minute
SEM	Scanning electron microscopy
SMCP	Shape memory creation procedure
SMP	Shape memory polymer
SME	Shape memory effect
SPR	Surface plasmon resonance
TC	Thermal conductivity
TEM	Transmission electron microscopy
TGA	Thermogravimetric analysis
THW	Transient hot wire
TS	Tensile strength
UV-Vis	Ultraviolet visible

1. VISION

The ultimate goal of the study is derived from the idea on using external stimuli to activate nanocomposites either by magnetic or electromagnetic field. Eventual remote control of nanoactuators is aimed to be used for activating hosting material; shape memory polymers which have a wide range of applications in biomedical field.

Initially, gold and silver nanoparticles were dispersed in polymer matrix for further applications. The preparation techniques of nanoparticles and nanocomposites are presented in chapter 2 & 3 respectively. Several characterization methods such as transmission and scanning electron microscopy, dynamic light scattering were demonstrated to confirm particle uniformity and homogeneity. On the other hand, differential scanning calorimetry and dynamical mechanical analysis tests were applied in order to check if these nanofillers improve the thermal and mechanical properties of resulted nanocomposites. The details of the experiments, experimental results and comparative plots are given in chapter 4.

Before moving on with photothermal experiments, the effect of functionalized silver nanoparticles over the thermal conductivity of base fluids was investigated via hot wire technique. Chapter 5 is comprised of experiments on enhancement or deterioration in effective thermal conductivity of water, ethylene glycol and hexane based silver nanofluids.

A novel method on estimating local temperature and crystallinity through conformational and structural changes in poly (ethylene oxide) was proposed via Raman spectroscopy in chapter 6. And finally, the actuation of gold nanoparticles dispersed in polymer matrix was demonstrated in chapter 7. A shape memory polymer which can respond to dual actuation; by magnetic and/or electromagnetic field was created. The temperature change in polymer due to photothermal heating was followed via fluorescence spectroscopy and shape memory schemes were presented at the end of the study.

2. GOLD AND SILVER NANOPARTICLES

2.1. INTRODUCTION

It is known that gold and silver have been widely used in ancient times for mostly aesthetic and curing purposes. The most distinctive use of gold for decorative construction reported in history was for the marvelous statue of King Tutankhamen around 1200-1300 BC in ancient Egypt [1]. The colloidal gold and silver, on the other hand, have been employed since Roman times for dyeing and coloring the glass and ceramics to yellow, red or mauve with using both two metals at the same time. The reputation of colloidal gold was also known as cure for various diseases such as cardiac problems, dysentery, epilepsy and syphilis [2].

The first 'scientific' use of gold was reported by Michael Faraday in 1857 [3]. He suggested a synthesis route for gold nanoparticles (Au NPs) through reduction of gold salts (chloroaurate, AuCl_4^-) using phosphorus stabilized carbon disulfide (CS_2) and studied their optical properties by drop casting the Au NP solution on thin films. Metal nanoparticles, especially gold and silver nanoparticles (Ag NPs), have attracted great interest due to their unique properties since then. Their dimensions are in the nanometer range; i.e. generally larger than small molecules, but much smaller than bulk material. In this size regime, electronic, physical and chemical properties of metallic nanoparticles show different variations. The fundamental properties of nanoparticles not only depend on their structural properties but also their shape, crystallinity and phase of the nanomaterial [4].

Nanoparticles have relatively large surface area to volume ratio because of their small sizes. This property affects both NP's own properties and also their neighboring interactions by making them different from their bulk materials. Their exclusive properties are suggested to be used in different applications in the fields of catalysis, photonics, optoelectronics, biological labeling and imaging, sensing, magnetic devices, information storage and so on [4].

Chapter 2 gives literature survey on the methods used to synthesize Au and Ag NPs in various size ranges. In this work, hydrophilic and hydrophobic synthesis techniques were used for preparing both Au & Ag NP colloidal solutions. Details of these synthesis methods and corresponding characterization techniques are also given.

2.2. SYNTHESIS OF NANOPARTICLES

Metal NPs have been prepared by both ‘top - down’ and ‘bottom - up’ techniques. The first ‘top - down’ approach involves division of bulk metals with large portions into smaller pieces by breaking down the strong forces in metals; either by milling, attrition or chemical methods. Several researchers developed the ‘top - down’ method via chemical methods such as ion irradiation in air [5], arc discharge in water [6] and laser ablation in solution [7] etc. However, the use of ‘top - down’ method is limited since it is difficult to control size and uniformity of the resulted particles. On the other hand, ‘bottom - up’ approach enables the control of size, shape and uniformity of the particles with using wet chemical process including chemical reduction of metal salts, electrochemical pathways and decomposition of organometallic compounds [8].

Many NP syntheses usually start with reduction of metals’ salts at elevated temperatures leading to nucleation and growth of nanoparticles. The growth and stabilization of the NPs are terminated by addition of surfactants. The control over nanoparticle size and shape requires the isotropic growth on nanoparticle seed surface. The specific conditions should be kept during the process; pH, temperature, surfactant and chemical concentration, etc. Otherwise, anisotropic growth would lead to the formation of nanoparticles in particular shapes. The formation of the Au nanoparticles via chemical reduction method, presented as in Figure 2.1, is taken from the work of Nguyen et al [8].

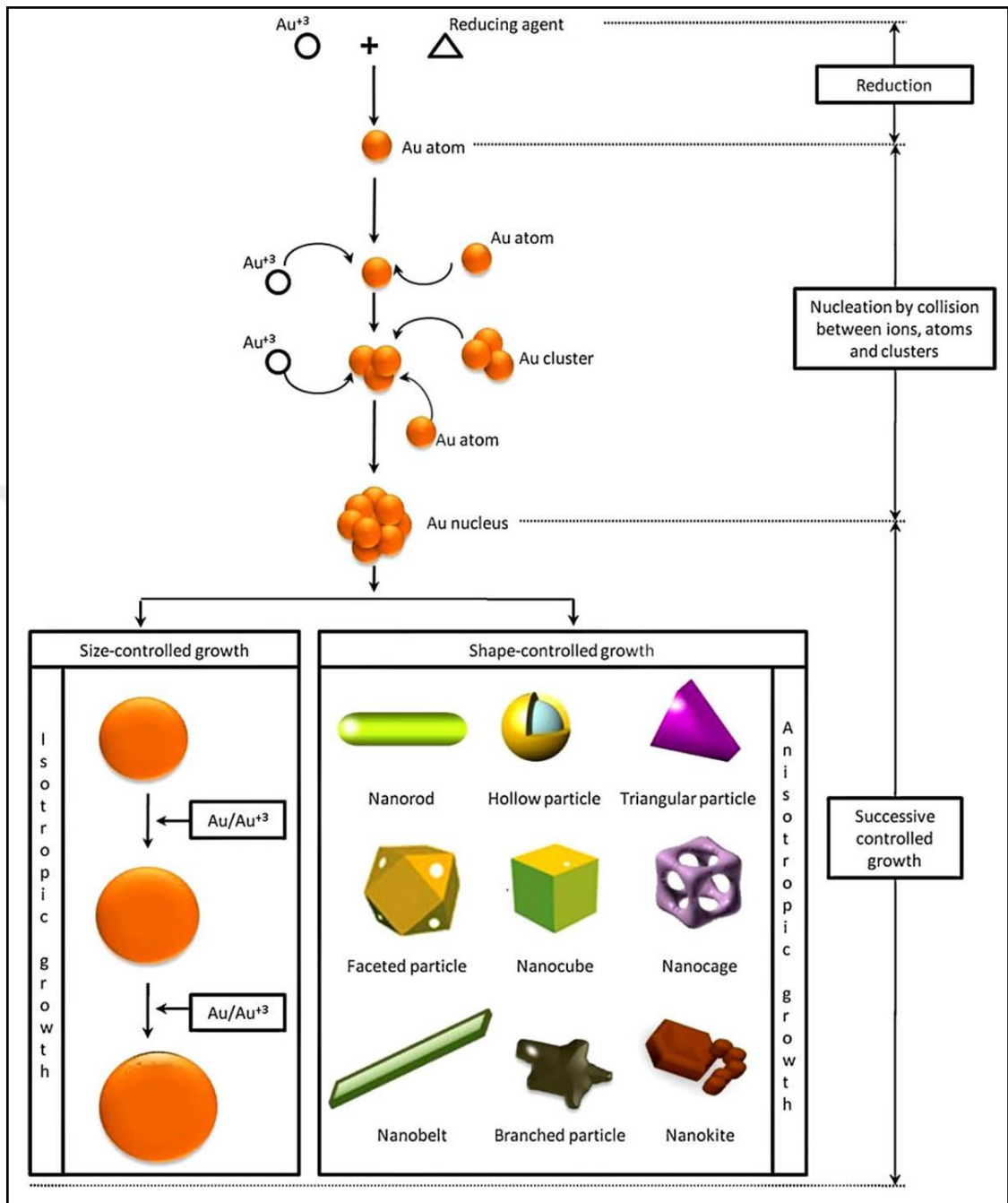


Figure 2.1. Formation mechanism of Au NPs with various particle sizes and shapes by chemical reduction method [8]

Among all conventional methods those proposed to obtain Au NPs via reduction of Au (III) derivatives, citrate reduction is still predominantly used due to the ease, reproducibility and economical availability of the method. The citrate reduction method was introduced by Turkevitch in 1951 [9] and then developed for controlled size formation by Frens in 1973 [10].

In Frens method, an aqueous solution of gold (III) chloride is heated to boil and sodium citrate is added. At elevated temperature, citrate ion reduces Au (III) to Au⁰ and then stabilizes the atom by forming a covalent bond at the particle surface. In other words, the electrostatic double layer occurs between negatively charged citrate and positively charged sodium ions. Although the particles stay suspended in an ionic solvent due to the electrostatic layer, the force can be broken with addition salt of Na⁺ or another cation; which is known as 'salting out'. The size of the particles can be altered by varying the amount of citrate added. However, it is almost impossible to re-disperse synthesized nanoparticles once they are dried, which limits the application of the NPs.

The precise particle size control was introduced by Brust et al. [11] by taking advantage of strong alkanethiolate / Au chemistry and then developed by Jana et al. in 2001 [12]. In the case of Brust's 'two phases' method, AuCl₄⁻ was transferred from aqueous solution to toluene using tetraoctylammonium bromide as the phase-transfer reagent and reduced with aqueous sodium borohydride (NaBH₄) in the presence of dodecanethiol (C₁₂H₂₅SH). The size of the resulted Au NPs with a surface coating of thiols can be tuned in the 1-30 nm range.

Another common approach for controlling the size is 'seed mediated growth'; in which small particles are prepared first and subsequently used as 'seeds' for making larger particles. Basically, preformed seeds are used as nucleation centers and suitable growth conditions inhibit secondary nucleation. The complexity of the technique can limit the application of NPs due to the possible additional nucleation mitigated by poor growth conditions. To avoid additional nucleation and obtain successive growth, step by step enlargement method is suggested by Jana et al. [12]. TEM images of these particles are shown in Figure 2.2. At room temperature, citrate coated Au particles are synthesized through NaBH₄ reduction to be used as 'seeds' with a particle size of 3.5 nm.

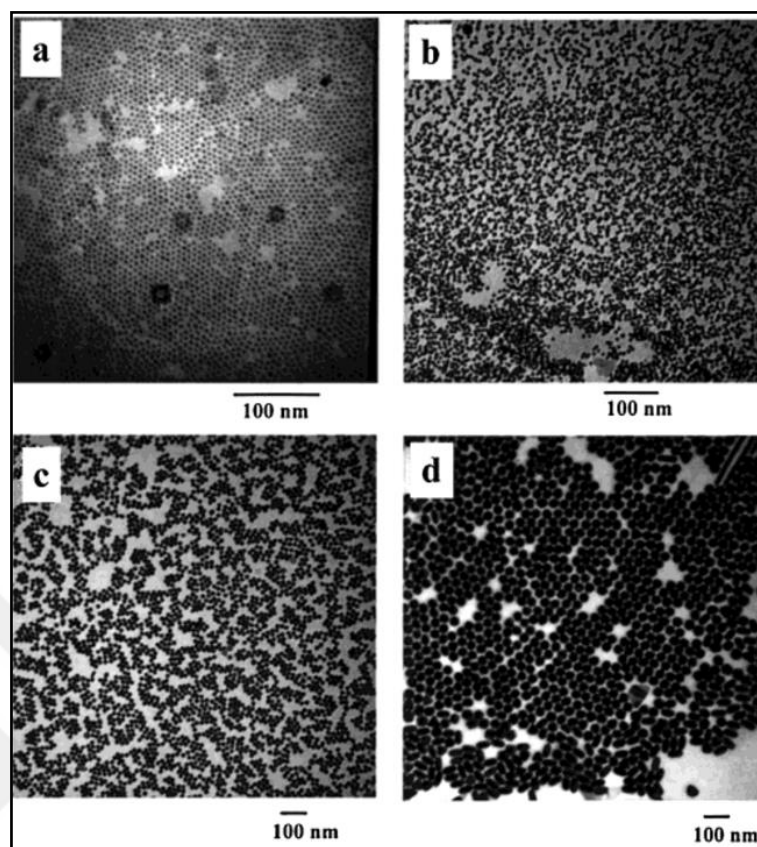


Figure 2.2. TEM images of larger nanoparticles prepared from seed: (a) 5.5 ± 0.6 ; (b) 8 ± 0.8 ; (c) 17 ± 2.5 ; (d) 37 ± 5 nm after separation of nanorods [12]

An aqueous solution of HAuCl_4 , and cetyltrimethylammonium bromide (CTAB) are heated to boiling, then cooled to room temperature and used as stock ‘growth’ solution. Finally, seed and growth solutions are mixed in presence of ascorbic acid. By varying the portions of seed, growth and ascorbic acid solutions, Au NPs with size in 5 - 40 nm range are obtained. It was observed that synthesized particles capped with CTAB are stable more than a month and can also be converted to thiol-capped clusters by ligand exchange [12].

During the last decade, minimizing hazard and waste of the nanoparticles became essential considering the wide application area and distribution of these materials. Thus ‘green synthesis’ methods were developed by scientists regarding the ‘green chemistry’ concept which is defined as the utilization of a set of principles that reduces or eliminates the use or generation of hazardous substances in the design, manufacture, and application of chemical products [13]. The 12 principles of ‘green chemistry’ were first described by Anastas in

1998 [14] and translated for application in the practice of green nanoscience by Dahl et al. in 2007 [13].

Practicing greener nanomaterials and nanomaterial production methods involve determining the biological impacts of NP size, surface area and surface functionality; studying nanomaterial degradation and fate in the environment; eliminating solvent-intensive purifications by utilizing selective nanosyntheses; utilizing more benign feed stocks, derived from renewable sources; pursuing efficient synthetic pathways that can be carried out at ambient temperatures rather than elevated temperatures [13].

Other than the methods proposed containing citrate reduction and use of alkanethiolate as surfactant, Medina-Ramirez et al. reported a convenient study indicating that the formation of stable Ag NPs can be achieved using green chemistry methods [15]. The materials used in the method were all prepared in the form of aqueous dispersions and the synthesis was carried out at lower temperatures (<100 °C). In a typical synthesis of hydrophilic Ag NPs, silver powder is obtained through the reaction of silver nitrate (AgNO_3) with NaBH_4 , where gum arabic serves as a dispersing agent [15, 16]. Resulted particle sizes were controlled in the range from 10 to 50 nm.

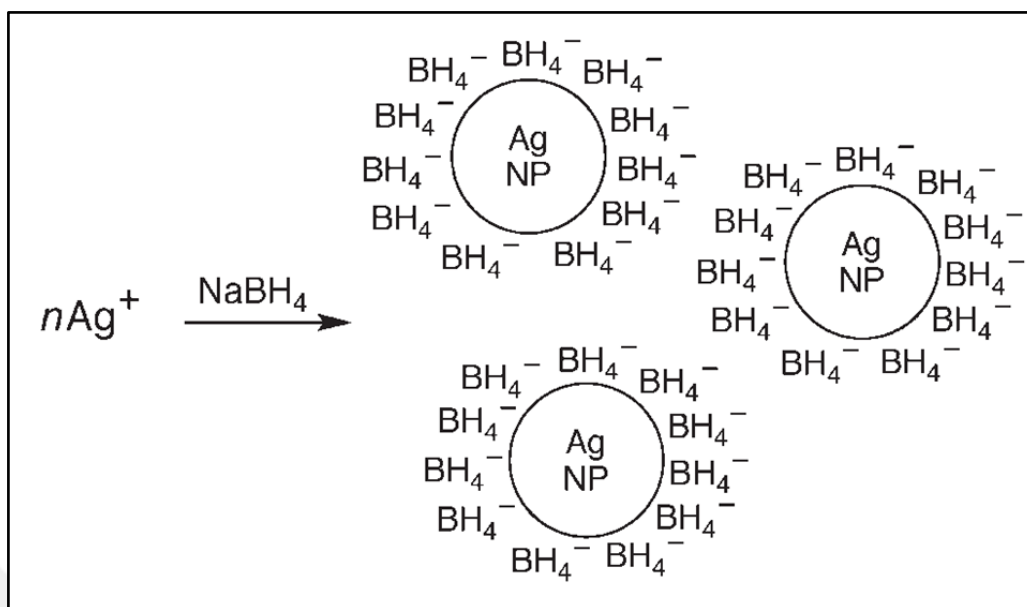


Figure 2.3. The formation of BH_4^- capped Ag NP illustrated by Salomon et al. [16]

Osterloh et al. proposed an inexpensive, versatile and very reproducible method for the large-scale synthesis of organoamine-protected nanoparticles in the 6-21 and 8-32 nm size ranges for Au and Ag respectively [17]. Resulted particles can be suspended in organic fluids for a long time. A significant difference between thiol and organoamine chemistry synthesis is that amine ligands can serve both as reducing agent and capping ligands for nanoparticle synthesis. Therefore only few reagents are required to establish the procedure. Oleylamine and oleic acid are commonly used reducing reagents since they are commercially available and inexpensive.

The use of oleylamine to reduce tetrachloroauric acid or silver acetate in a refluxing organic solvent -toluene, dichlorobenzene, hexane or dichlorobenzene- is presented in the work of Osterloh et al. Reflux in hexane, toluene, and 1,2-dichlorobenzene yield 8.5 nm, 12.7 nm and 32.3 nm Ag NPs, respectively. At the same study, organoamine-protected Au NPs of variable sizes form by refluxing a solution of tetrachloroauric acid and oleylamine in toluene over the course of 120 min. The sizes of the particles are reported to be regulated from 15.3 to 21.3 nm by alternating the concentrations of oleylamine and gold precursor [17].

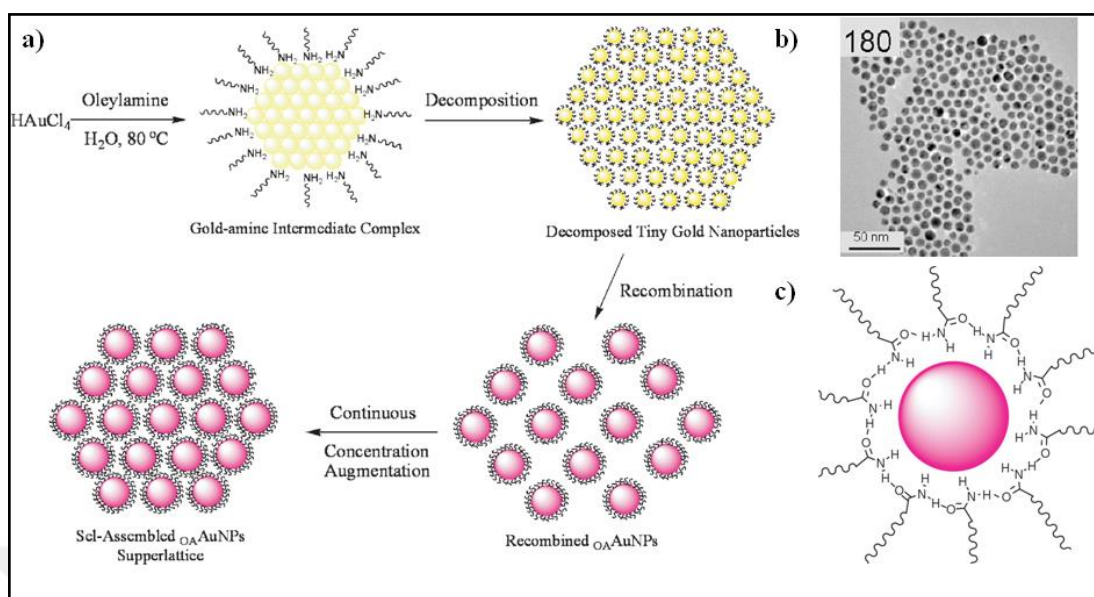


Figure 2.4. (a) Gold particles formation process using oleylamine; (b) TEM images of Au NPs after 180 min; (c) The hydrogen bonding network formed between oleylamine ligands as a protecting layer on the gold nanoparticles [18]

According to another study on organoamine-protected nanoparticle synthesis, few conclusions came out with respect to the $^1\text{H-NMR}$ and FTIR results [18]. The most important finding of the research is the formation of amides while gold (III) is reduced (Figure 2.4.c). The oxidation of amine ligands results a hydrogen bonding network as a protecting layer around nanoparticle surface. In any case, organoamine surfactants can be exchanged with thiol based reagents to be used in further applications.

2.3. EXPERIMENTAL

Both hydrophobic and hydrophilic nanoparticles were synthesized in this study. The characterization of nanoparticles was performed via UV-Vis spectrophotometry, dynamic light scattering (DLS), transmission electron microscopy (TEM), fourier transform infrared spectroscopy (FTIR) and thermogravimetric analysis (TGA).

2.3.1. Hydrophilic Nanoparticle Synthesis and Characterization

There exist several methods for preparing Au/Ag NPs in aqueous phase. All other methods proposed for synthesizing NPs; like seed mediated growth, citrate reduction and alkanethiolate capping were tried in this work but green chemistry route was selected since it is easier to scale-up the procedure. The method aims to produce water soluble nanoparticles using AgNO_3 as metal source, NaBH_4 and gum arabic as reducing and dispersing agents respectively [15]. The chemical reaction for borohydride reduction of AgNO_3 is given below;



In a typical synthesis, aqueous gum arabic solution (3 per cent, m/w) is prepared with dissolving 1.5 g of Gum Arabic ($\text{C}_6\text{H}_{10}\text{O}_5$, Merck, Pure) in 50 mL distilled water. The solution was then stirred in a round bottom flask at 60 °C. After 30 minutes of mixing, 3.5 mL & 0.1 M aqueous solution of AgNO_3 (Fluka, 99.5 per cent) was added to the flask under continuous stirring. The conditions were kept constant for 15 minutes until the diffusion of metal ions into the pores of dispersing agent is completed. 3.5 mL of 0.1 M NaBH_4 solution (Merck, 98 per cent) was then injected into the flask and the reaction temperature was elevated to 85 °C. The solution was left for 3 hours under continuous agitation at 85 °C. It should be noted that all the solutions were freshly prepared prior to experiment.

The colloidal solution was centrifuged and washed with ethanol (Sigma Aldrich, absolute, ≥ 99.8 per cent) for three times in order to remove excess reagents. After three times of centrifugation (10 minutes at 6000 rpm), NPs were left to dry in oven at 32 °C overnight. The reaction yields 0.036 g of Ag10/w NP powder.

2.3.2. Hydrophobic Nanoparticle Synthesis and Characterization

The hydrophobic Ag NP synthesis method proposed by Osterloh et al. was performed in which silver acetate is used as metal precursor. The method is known with reproducibility

and low polydispersity (6.9 per cent) [17] and also it can be scaled-up easily for further applications. The same procedure offered for producing Ag NPs was also adapted to Au NP synthesis with shifting the silver acetate to gold (III) acetate.

Basically, the method comprises the reduction of silver/gold salt via addition of organic surfactants with hydrocarbon chains such as oleylamine and oleic acid. 150 mg of silver acetate (ChemPur GmbH, 99 per cent) was dispersed in refluxing solvent of 150 mL toluene (AnalaR, NORMAPUR®, min. 99.5 per cent) for 30 minutes. 3.5 mL of oleylamine (Fluka, technical, ≥ 70 per cent, GC) and 3.5 mL of oleic acid (Aldrich, 65.0-88.0 per cent, GC) were then transferred to boiling solution of silver acetate and toluene. The reaction was carried out in a round bottom flask containing glass beads and attached to a reflux condenser for 24 hours. The temperature of the reaction medium was around 110 °C, at which is where the boiling of toluene occurs.

Identical procedure was applied for producing Au NPs with using gold (III) acetate instead of silver acetate. This time, 336 mg of gold (III) acetate (Alfa Aesar, 99.9 per cent, metal basis) was added to 150 mL of toluene. Oleic acid and oleylamine again served as surfactants and all other reaction conditions were set to be the same as in Ag NP synthesis. Colloidal solutions of Au and Ag NPs were centrifuged three times with methanol (Sigma Aldrich, CHROMASOLV®, ≥ 99.9 per cent) at 6000 rpm for 10 minutes. Resulted precipitates were collected and left to dry in an oven at 32 °C. The reactions yield 0.176 g of Au and 0.096 g of Ag NP powders. Nanoparticle samples were named as Au(Ag)10/o.

Procedures containing solvent with relatively low boiling temperature (i.e. Toluene, b.p. 110 °C) are proposed to synthesize Au and Ag nanoparticles in smaller size. In order to increase the size of the particles formed, 1,2-dichlorobenzene (Fluka, 98 per cent, b.p.: 180 °C) was used as a solvent. This is what happens during the nanoparticle formation in 1,2-dichlorobenzene medium; at 30 minutes, the reaction solution shows a bimodal size distribution of ~3 nm and 8.9 nm Ag NP. Within the following 7 hours, the large particles become larger and the number of small particles decreases. After 8 hours, the reaction is nearly complete, and the large particles are 27.0 (13.8 per cent) nm in diameter. These particles can be obtained in pure form by precipitation with methanol. The latter is likely due to the high temperature of the reaction in 1,2-dichlorobenzene [17].

150 (336) mg of silver acetate (gold (III) acetate) were quickly injected to a refluxing solvent of 150 mL 1,2-dichlorobenzene. 7.5 mL, freshly prepared oleylamine and oleic acid solution with a 1:1 volumetric ratio were then transferred to solution. After 8 hours of reaction, the solution was cooled down and left at room temperature. The solution was centrifuged with methanol three times (6000 rpm, 10 minutes) in order to remove excess reagents and the precipitate was collected. After drying the precipitate in an oven at 32 °C, the resulting dry NPs were dispersed in chloroform. This time, resulted particles were named as Au (Ag) 30/o.

UV-Vis absorption spectra to determine the typical absorption bands for Au and Ag NPs were obtained using Lambda 25 UV-Vis Spectrophotometer (Perkin Elmer). Both Au and Ag NPs dissolved in chloroform were placed in optical glass cuvettes with 10 mm path width and scanned between the wavelengths of 300 nm and 600 nm. Size distribution of Ag and Au NPs and their complexes in chloroform suspensions were measured by a Zetasizer NanoZS instrument (Malvern Instruments). The measurements were performed at 25 °C using three subruns for each scanning.

Sample images for Au10/o, Ag10/o and Ag10/w were collected with JEOL JEM-ARM200CFEG UHR-Transmission Electron Microscope with an accelerating voltage of 200 kV. Nanoparticle suspensions were dropped onto carbon coated 200 mesh copper grids and dried at ambient conditions. Au30/o and Ag30/o NPs were drop-casted on Cu grids from the chloroform solutions and TEM images of these particles were taken using FEI Technai, G2 F30 type of electron microscope. Images obtained from microscope were processed by ImageJ [19].

FTIR (Perkin Elmer, Spectrum One) measurements were conducted with oleylamine, oleic acid and nanoparticle solutions at room temperature in the transmission mode to study the interaction between surfactants and nanoparticles. Dry KBr powder was placed in an evacuable die and pressed in a manual hydraulic press. Resulted KBr pellets were in 13 mm diameter and 1.5-2 mm thickness. 10 µl of oleylamine, oleic acid and NP solutions were dropped and dried on these pellets. Each sample was scanned from 500 cm⁻¹ to 4000 cm⁻¹.

Surface coverage of nanoparticles with oleylamine and oleic acid ligands was studied via TGA. Experiments were performed with using Perkin-Elmer (Pyris 1-TGA). Solid Au and Ag NPs were heated at constant rate of 10 °C/min under nitrogen atmosphere up to 600 °C.

2.4. RESULTS AND DISCUSSION

2.4.1. Hydrophilic Nanoparticles

Size analysis by counting 330 particles and measuring sizes on TEM micrographs showed that the green route synthesis gave spherical particles in the range of 3 nm to 17 nm having an average size of 7.27 nm. Size distribution was found to be 7.3 ± 2.5 nm and the size histogram is given in Figure 2.5.b.

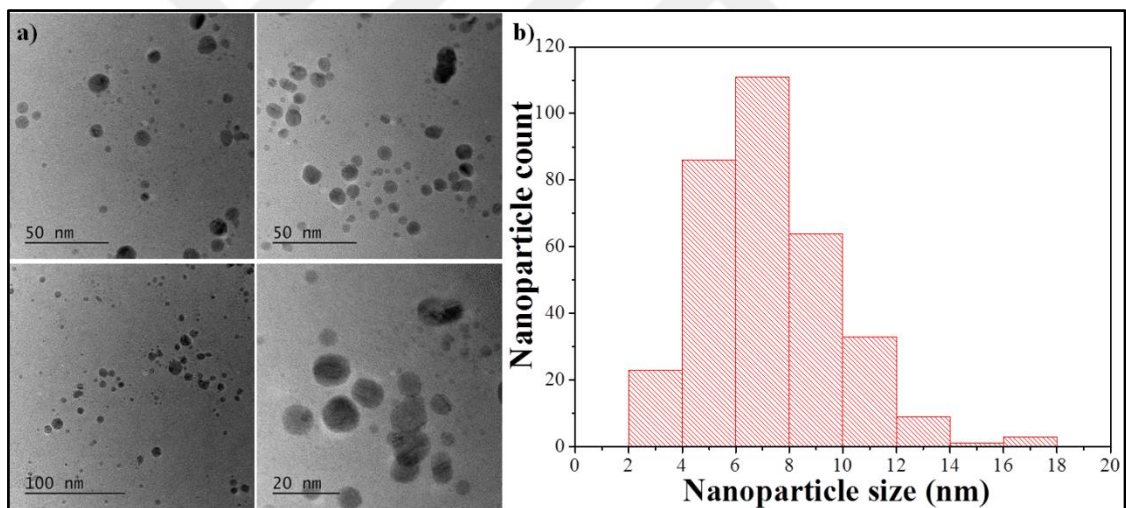


Figure 2.5. (a) TEM images and (b) Size distribution of Ag10/w NPs synthesized in water (Green route synthesis).

2.4.2. Hydrophobic Nanoparticles

2.4.2.1. Size Distribution of Au10/o and Ag10/o Nanoparticles

The size of the Au10/o and Ag10/o nanoparticles were determined by image analysis of TEM. While Figure 2.6.a shows the size distribution of Au and Ag NPs, representative TEM images of them are given in Figure 2.6.c and 2.6.d respectively. The average diameter of Au10/o (Ag10/o) nanoparticles was measured as 8.92 ± 2.71 nm (8.38 ± 2.00 nm) based on 196 (200) nanoparticles.

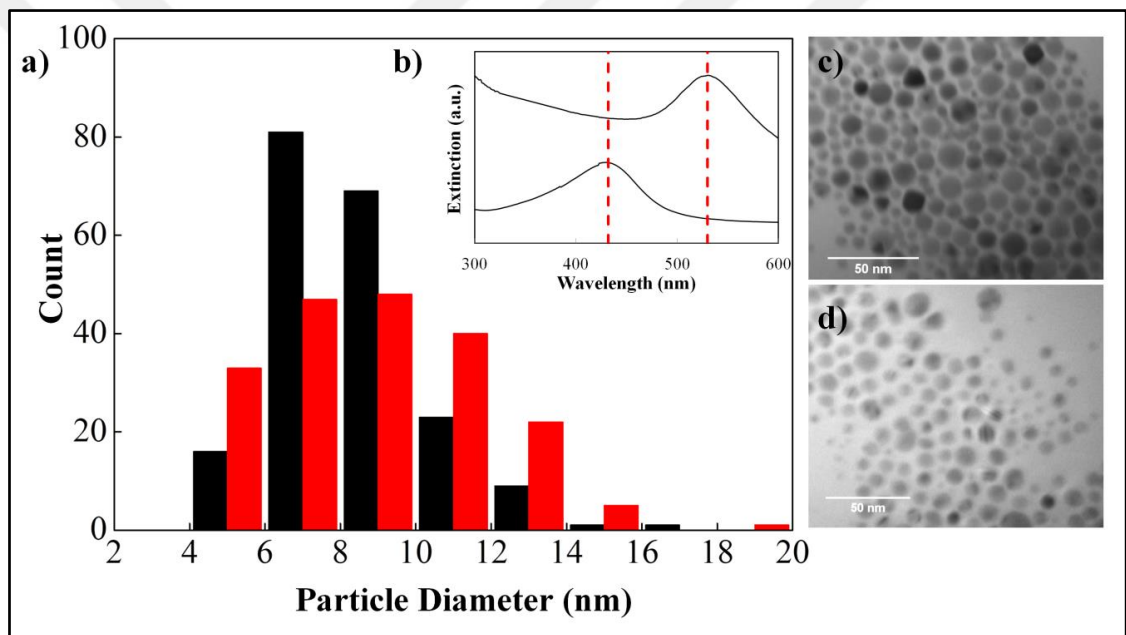


Figure 2.6. (a) Particle size distribution; (b) Extinction measurement of NPs; representative TEM images of (c) Au10/o (red bars) and (d) Ag 10/o (black bars) nanoparticles

Based on DLS analysis, both Au and Ag NPs displayed good colloidal properties in chloroform. The mean hydrodynamic diameter (Z-average) of oleylamine and oleic acid modified Au (Ag) NPs were found to be 12.36 ± 0.26 nm (12.53 ± 4.06 nm). Light scattering profile of the Au (Ag) NPs in chloroform has a single peak denoting that they dispersed well in the chloroform (Data not shown). According to the UV absorption

spectra, Au and Ag NPs displayed peaks at 530 and 432 nm respectively and both indicated by vertical red dashed lines in Figure 2.6.b.

2.4.2.2. Thermogravimetric Analysis of Au10/o and Ag10/o Nanoparticles

TGA is widely used for determining the inorganic and organic contents of materials. Since the Au and Ag NPs are capped with surfactants with hydrocarbon chains (oleic acid and oleylamine), the weight loss due to surfactant evaporation (or decomposition) is expected to occur around at 300 °C - 500 °C. TGA analysis of oleylamine-oleic acid (1:1 by vol) mixture was previously studied by several researchers [20, 21] and obtained data is presented in Figure 2.7.

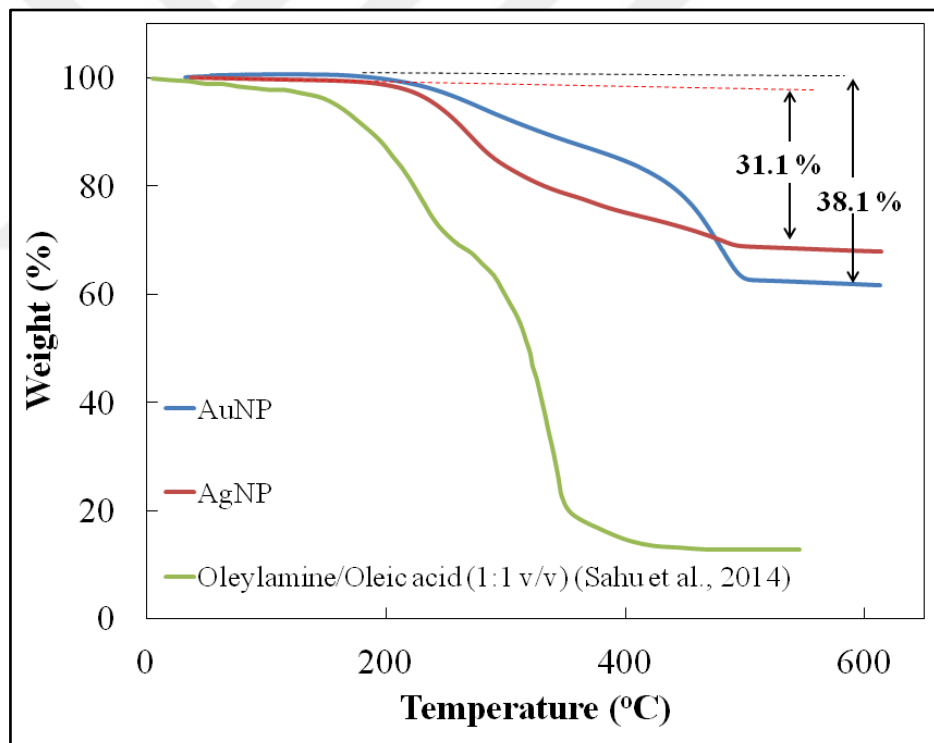


Figure 2.7. TGA plots of Au10/o, Ag10/o NP samples and oleylamine/oleic acid (1:1 v/v) mixture

For the oleylamine/oleic acid mixture plot, the major weight loss was observed at 350 °C which is almost around 80 per cent, also a weak shoulder is apparent at 250 °C. These are both attributed to evaporation (or decomposition) of surfactants as CO₂ and H₂O [21]. For

oleylamine and oleic acid capped Au10/o (Ag10/o) NPs, the major weight loss (38.1 per cent for Au NPs and 31.1 per cent for Ag NPs) was observed around 500 °C, confirming that the surface of the gold and silver nanoparticles are successfully capped with oleylamine and oleic acid. It is also possible to determine the ratio of oleic acid and oleylamine attached to surface; however is not investigated in this study.

2.4.2.3. Fourier Transform Infrared Spectroscopic Analysis of Au10/o and Ag10/o Nanoparticles

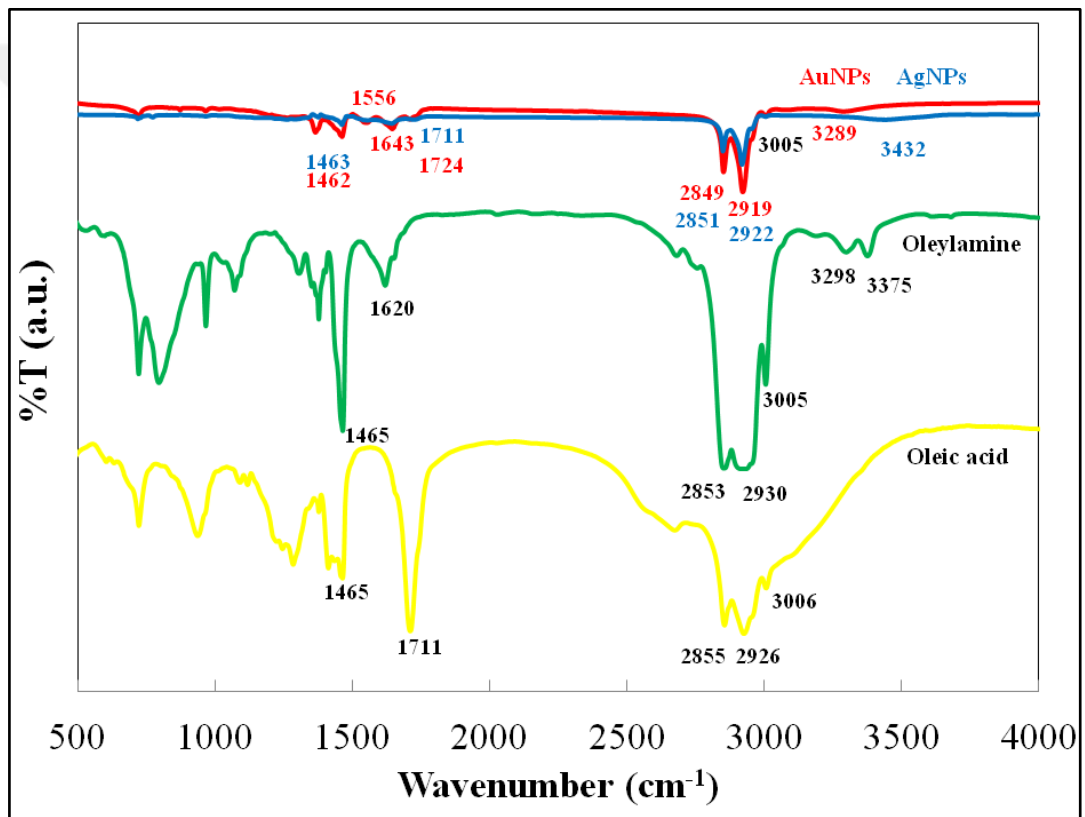


Figure 2.8. FTIR spectra of oleylamine, oleic acid, Au and Ag NPs

The FTIR spectrums were recorded to get a better understanding about the surface interactions of Au (Ag) NPs and were compared with pure oleylamine and oleic acid. There have been some studies reported oleylamine/NP [22] and oleic acid/NP [23, 24]) interactions, but only few of them [20] listed the FTIR peaks of both oleylamine and oleic acid modified NPs. In this work, FTIR plots for oleylamine, oleic acid and NPs are also presented in Figure 2.8 and vibrational assignments of possible interactions between them in Table 2.1.

Table 2.1. Vibrational mode assignments for oleylamine (Oamine), oleic acid (Oacid), Au and Ag NPs

Wavenumber (cm ⁻¹)				Assignments
Au NP	Ag NP	Oamine	Oacid	
3289	3432			OH interactions between OAmine and OAcid
			3000-3600	OH stretch of carboxylic acid [21]
		3375		Free NH ₂ stretch [18]
		3298		Free NH ₂ stretch [18]
3005	3005	3005	3006	CH stretch in C=C-H [18, 21, 25]
2919	2922	2930	2926	Asym. CH ₂ stretch [21, 23, 25]
2849	2851	2853	2855	Sym. CH ₂ stretch [21, 23, 25]
1724	1711		1711	C=O stretch [21, 23, 25]
1643				Amide vibrations [18]
		1620		Free NH bend [18]
1556				Amide vibrations [18]
1462	1463	1465	1465	O-H in plane for oleic acid [21] , CH ₂ bending [25]

Major differences between surfactants and Au (Ag) NPs are observed after 3000 cm⁻¹ and on specific bands of 1711 cm⁻¹ and 1620 cm⁻¹. Characteristic bands between 2500 cm⁻¹ and 3000 cm⁻¹ are responsible for asymmetric and symmetric CH₂ stretching and almost same for all samples containing hydrocarbon chains. The broad feature around 3000 cm⁻¹

in oleic acid spectra represents OH stretch of a carboxyl group. Two small peaks in 3298 cm^{-1} and 3375 cm^{-1} are due to free 1° Amine stretching in oleylamine. Single peaks at 3289 cm^{-1} in Au NP (3432 cm^{-1} in Ag NP) spectra, on the other hand, might be responsible for both OH stretch in oleic acid and possible oxygen hydrogen interactions between heads of oleic acid and oleylamine.

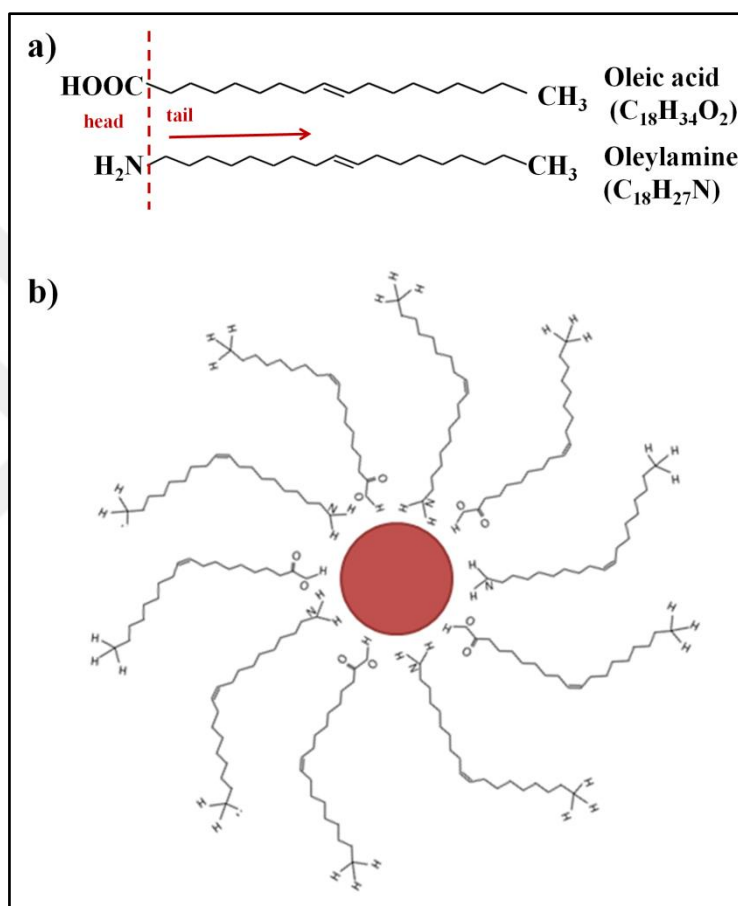


Figure 2.9. (a) Chemical formulations of oleylamine, oleic acid; (b) Representative image of oleylamine and oleic acid capped nanoparticle

Oleylamine and oleic acid tethering to nanoparticle surface favors from ‘heads’ of the molecules; $-\text{COOH}$ or $-\text{NH}_2$ sides [18] (See Figure 2.9.b). FTIR experiments revealed that the amine ligands at oleylamine are oxidized into amides, while gold (III) was reduced [18]. The single peak observed at 1620 cm^{-1} in oleylamine spectra is assigned for free NH bending. Referring to Figure 2.8, the bands at 1620 cm^{-1} disappeared and two additional

bands appeared at 1643 cm^{-1} and 1556 cm^{-1} indicating the presence of amide bonds in Au NPs because N-H groups are involved in hydrogen bonds.

The carbonyl stretching peak at 1711 cm^{-1} for oleic acid is located at 1724 cm^{-1} in Au NP spectra. However despite the presence of carbonyl peak in Au NP spectra, the intensities are not as strong as in neat oleic acid, implying that there is small amount of physically adsorbed free oleic acid molecules left around Au NPs. The reason that carbonyl peak is no longer dominant for Au NP solution can be explained by chemisorption of oleic acid molecules to the surface of the nanoparticle via their oxygen atoms.

2.4.2.4. Size Distribution of Au30/o and Ag30/o Nanoparticles

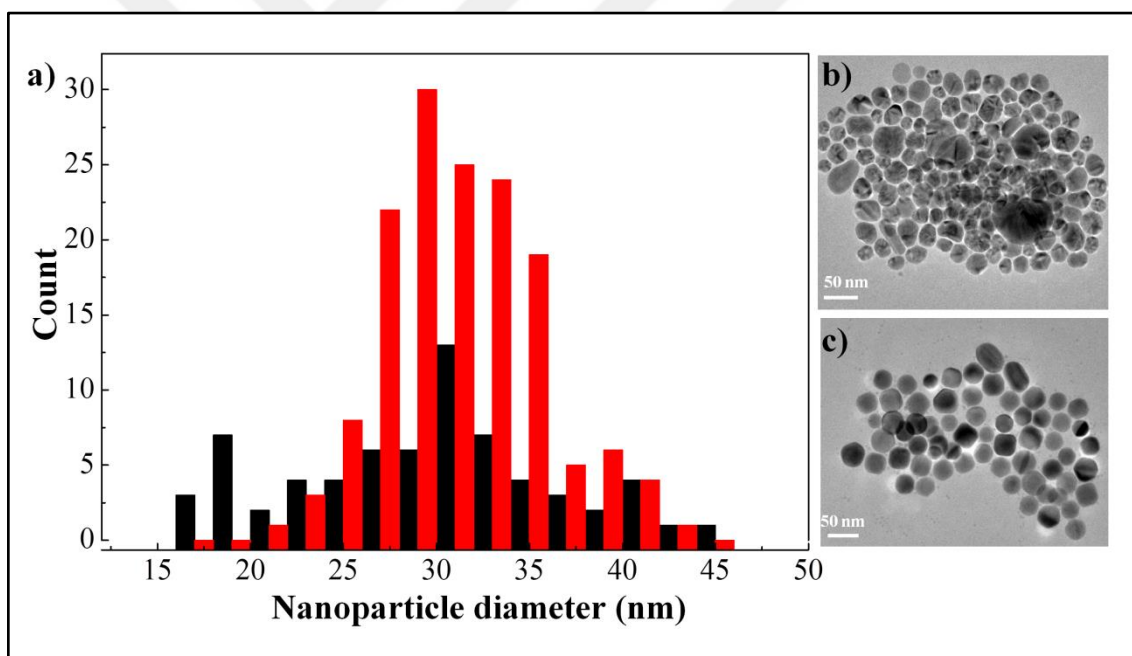


Figure 2.10. (a) Particle size distribution; representative TEM images of (b) Au30/o (black bars) and (c) Ag30/o (red bars)

Figure 2.10. b and 2.10.c give the TEM images collected from the Au and Ag NP suspensions drop coated on Cu TEM grids and their size distribution. The average diameter of Ag NPs was found to be $31.12 \pm 4.24\text{ nm}$ based on 151 particles. The mean of the Au NPs was calculated as 29.48 nm with a standard deviation of 6.89 nm based on 67 nanoparticles.

The peak for the SPR of Au10/o NPs was recorded at 530 nm, whereas it is found at 535 nm for Au30/o particles. The trend fits with the model proposed by Haiss et al. [26]. For Ag NPs, a slight decrement in the SPR peak location was observed with the increase of NP size ($\lambda_{\text{Ag10/o}} = 432 \text{ nm}$, $\lambda_{\text{Ag30/o}} = 412 \text{ nm}$). Also the DLS results for Au/Ag30 NPs gave narrow size distribution, indicating that solutions of NPs show good colloidal properties. The mean hydrodynamic diameter (Z-average) of Au30/o and Ag30/o NPs were found to be 24.36 ± 2.72 and $25.93 \pm 2.68 \text{ nm}$ respectively.

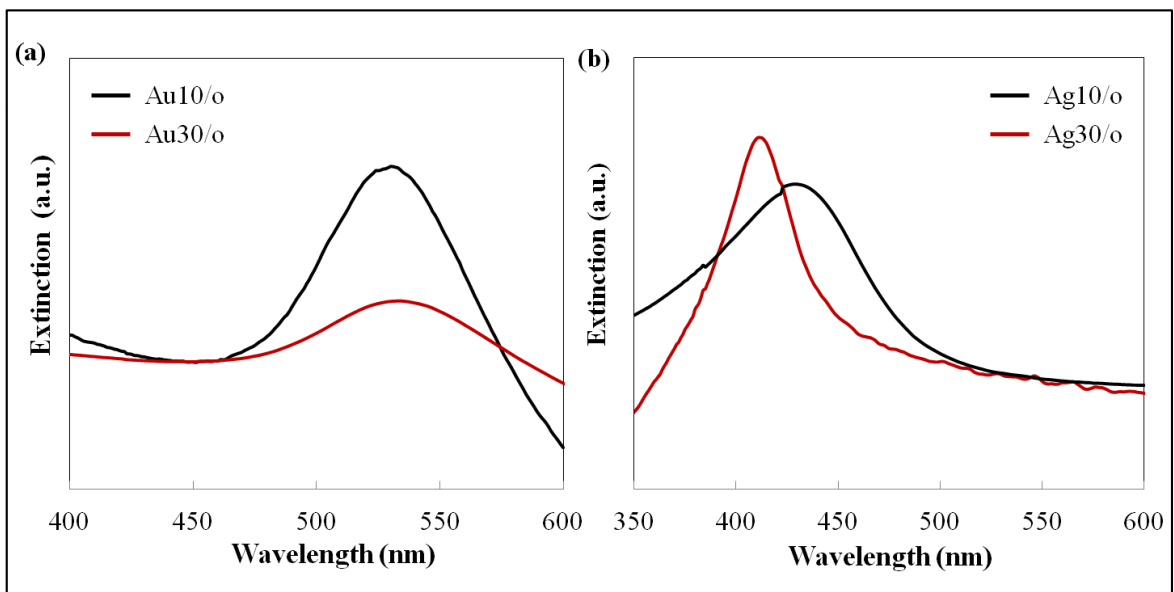


Figure 2.11. UV Extinction Spectra for (a) Au10/o and Au30/o; (b) Ag10/o and Ag30/o NPs

Table 2.2. The summary of abbreviations and results used for Au and Ag nanoparticles synthesized in this study

NP Name	NP type	Solubility of nanoparticle	Reaction medium	Surfactant	Diameter (nm)
Au10/o	Au	Hydrophobic /oil soluble	Toluene	Oleic acid- oleylamine	8.92 ± 2.71
Au30/o	Au	Hydrophobic /oil soluble	1,2 Dichlorobenzene	Oleic acid- oleylamine	29.48 ± 6.89
Ag10/o	Ag	Hydrophobic /oil soluble	Toluene	Oleic acid- oleylamine	8.38 ± 2.00
Ag30/o	Ag	Hydrophobic /oil soluble	1,2 Dichlorobenzene	Oleic acid- oleylamine	31.12 ± 4.24
Ag10/w	Ag	Hydrophilic /water soluble	Water	Gum arabic/ BH_4^-	7.30 ± 2.50

2.5. CONCLUSION

Nanoparticles have superior properties than the bulk materials due to their aspect ratio. The improved properties enable them to be used in wide range of applications. Gold (Au) and silver (Ag) nanoparticles were intensely studied in this work. There are several proposed Au and Ag NP preparation methods in literature. Most commonly used technique is the Frens method [10], involves citrate reduction of gold (III) chloride. Au NPs with a size of 16-42 nm were synthesized using Frens method. However, results have not been published in this work due to the lack of stability of NPs and the insufficient yield did not allow us to use them in applications. Therefore hydrophobic and hydrophilic NPs were synthesized through following Osterloh method [17] and green route synthesis [13] respectively.

Gum arabic & sodium borohydride mixture were used to stabilize NPs in water and oleic acid & oleylamine mixtures were used for oil-based solvents. According to TEM studies, hydrophilic Ag NPs were found to have a size of 7.3 ± 2.5 nm and named as Ag10/w. The size of the hydrophobic Au and Ag NPs, on the other hand, could have been altered with changing the reaction medium. In the first set of experiments; Au NPs with a diameter of

8.92 ± 2.71 nm and Ag NPs with 8.38 ± 2.00 nm were synthesized with using toluene as solvent. The change of solvent from toluene to 1-2 dichlorobenzene increased the size of Au and Ag NPs to 29.48 ± 6.89 nm and 31.12 ± 4.24 nm respectively. The hydrophobic NPs were named as Au10-30/o and Ag10-30/o for this case.

Additionally TGA and FTIR experiments were performed on Au10/o and Ag10/o NPs. According to TGA results, it was found that 38.1 per cent (by wt) of Au NPs are oleylamine & oleic acid and NPs are successfully covered with surfactants. Similarly the ratio was found to be 31.1 per cent (by wt) for Ag NPs. Also FTIR experiments revealed that there were almost no free oleylamine and free oleic acid left around particles; majority of the surfactants were adsorbed to NP surface. According to TEM, DLS, UV-VIS Spectroscopy, TGA and FTIR analysis results, the synthesized NPs are perfect candidates for applications for nanocomposites, nanofluids and nano-actuators due to their narrow size distribution and good colloidal properties.

3. NANOCOMPOSITES PREPARED WITH GOLD AND SILVER NANOPARTICLES

3.1. INTRODUCTION

For various reasons and potential applications, the combination of organic and inorganic particles has been widely used. Crustacean carapaces, mollusc shells, bone and tissues are examples of organic-inorganic natural materials used since the earlier times [27, 28]. The significant changes observed on the physical and mechanical properties of polymers with the addition of inorganic nanoparticles are explained by the large surface area, which increases the interaction between the nanoparticle and the polymer. Uniformly dispersed nanosized particles allow the development of new materials with tailored properties; materials belong to a new class of composites designated by Theng in 1970s as nanocomposites [29]. It has been decades since nanoparticles have been added to synthetic materials to improve properties as variant as mechanical [30, 31], electrical [31-33], optical properties [34] and gas permeability [35, 36].

Poly (ethylene oxide) (PEO) is a semicrystalline polymer which has a helical conformation with repeating units of $[-CH_2-CH_2-O-]$. PEOs are commercially available in wide range of molecular weight (M_w) from 200 to 7×10^6 g/mol. Low molecular weight PEOs, ($M_w < 20,000$ g/mol) are also named as poly (ethylene glycol) (PEG), have been widely used since the 1960s in a variety of scientific and biomedical fields [37]. PEO is also known with its solubility in water as well as in organic solvents like toluene and chloroform. The amphiphilicity of PEO comes from the molecular structure itself. The backbone of PEO consists of both ethylene

$[-CH_2-CH_2-]$ and ethylene oxide $[-CH_2-O-CH_2-]$ groups; representing hydrophobic and hydrophilic parts respectively. PEOs having high molecular weight, i.e. at M_w greater than about 1,000 g/mol, become insoluble in water [38].

In this chapter, PEO-based nanofilms were prepared with using film casting method. PEO powders and previously synthesized Au & Ag NPs (See Chapter 2) were mixed in a

solvent and then left for evaporation in an oven. Transmission Electron Microscope (TEM) and Environmental Scanning Electron Microscopy (ESEM) were used for imaging the homogeneous dispersion of NPs in films. This chapter aims to present the PEO/Au and PEO/Ag nanocomposite preparation and characterization techniques. PEO nanofilms were used in further mechanical, thermal and conformational studies as presented in chapters 4, 6 and 7.

3.2. APPLICATIONS OF NANOCOMPOSITES

Recently, polymer nanocomposites are used in many industrial areas such as electronic devices [39, 40], food packaging [41] and automotive or aircraft components [42] because of their unique properties such as high mechanical strength, thermal and chemical stability, good optical clarity and heat resistance. Also, the use of polymer nanocomposites as biomaterials became very popular due to their favorable properties such as good biocompatibility, easy design and preparation, a variety of structures and interesting biomimetic character during recent decades. Drug delivery techniques that use polymeric composites cover cancer targeting [43], protein and gene delivery [44, 45], micro and nano fabricated self-regulated devices [46], bio-recognizable systems, etc.

The major application areas of PEO-based nanocomposites are electrical and biomedical. Arzhakov et al. studied metal/PEO like plasma polymers and mainly focused on basic characterizations of Au/PEO nanocomposites [47]. The method developed by them allows obtaining nanocomposites with more than 80 per cent retention of the PEO character and with different filling by gold. PEO nanocomposites are closely related to the design of advanced devices for electronic and optoelectronic applications. Xu et al. reported poly (ethylene glycol) (PEG) and poly (ethylene oxide) (PEO)/lithium intercalated tungsten disulfide nanocomposites and found that the resultant nanocomposites displayed pretty good conductivity [48]. PEO electrolytes have also gained much interest due to their potential applications such as lithium rechargeable batteries and fuel cell. Another example for the lithium ion conductor studies with PEO matrix was demonstrated by Ibrahim et al. They pointed out a decrease in T_m , T_g and X_c values, which leads to increased conductivity for composite PEO electrolytes at 298K [39].

In addition, PEGs have a number of properties which are of interest in the biopharmaceutical sciences. They may be attached to the surface of liposomes in order to prevent recognition by the immune system, thus prolonging the circulation time of the liposomes [49]. Direct PEGylation of drugs to enhance their stability and bioavailability has been demonstrated for several drugs [50-53]. They are also known to cause fusion between cells [54] and may bind to proteins [55].

Some copolymers of PEO, i.e. poly (ethylene oxide-co-propylene oxide), [56, 57] show thermoresponsive properties and form two phase systems from relatively hydrophilic polymers such as dextran or modified starch and have been successfully used for protein purification. Block copolymers that have a thermosensitive 'smart' part that consists of poly (N-isopropylacrylamide) (P-NIPAAm) form reversible gels on an increase in temperature, whereas random copolymers separate from aqueous solutions by forming a concentrated polymer phase [58]. Reversible gel-formation of thermosensitive block copolymers in response to temperature could be utilized in different applications. Poly (NIPAAm) block copolymers with poly (ethylene oxide), which undergo a temperature-induced reversible gel-sol transition, were patented as the basis for cosmetics such as depilatories and bleaching agents [59]. The copolymer solution is liquid at room temperature and easily applied to the skin where it forms a gel within one minute.

Usually inorganic nano-fillers including metals and metal alloys (e.g. Au, Ag, Cu, Ge, Pt, Fe, CoPt), semiconductors (e.g. PbS, CdS, CdSe, CdTe, ZnO), clay minerals (e.g. montmorillonite, vermiculite, hectorite, CaCO_3), other oxides (e.g. TiO_2 , SiO_2 , ferric oxide), and carbon-based materials (i.e. carbon nanotube (CNT), graphite, carbon nanofiber) are added to polymer matrices to be used in several applications. Kim et al. have fabricated polystyrene and naphthalenethiol-capped Au nanoparticle composite nanofibers using an electrospinning technique [60]. In the same manner, 5-6 nm Ag nanoparticles were synthesized by Pandis et al. [61] and blended with poly (methylmethacrylate) (PMMA) at different weight percents (0 to 0.5 per cent, by wt). They both found improvements in mechanical and thermal properties of bulk polymers. Montazami et al. used Au nanoparticles to develop liquid crystal elastomer (LCE) actuators [62]. They came up with a conclusion that the AuNP-doped LCE actuators

exhibited more than a 100 per cent increase in the rate of change of strain with respect to time; resulting an improved material response.

The scientists who work on polymer nanocomposites all agree on the necessity of homogeneous dispersion of particles in polymer matrix to achieve tremendous mechanical, thermal and optical properties. However, a homogeneous dispersion of nanoparticles in a polymeric matrix is a very difficult task due to the strong tendency of nanoparticles to agglomerate [63]. Consequently, phase separation between components of nanocomposites

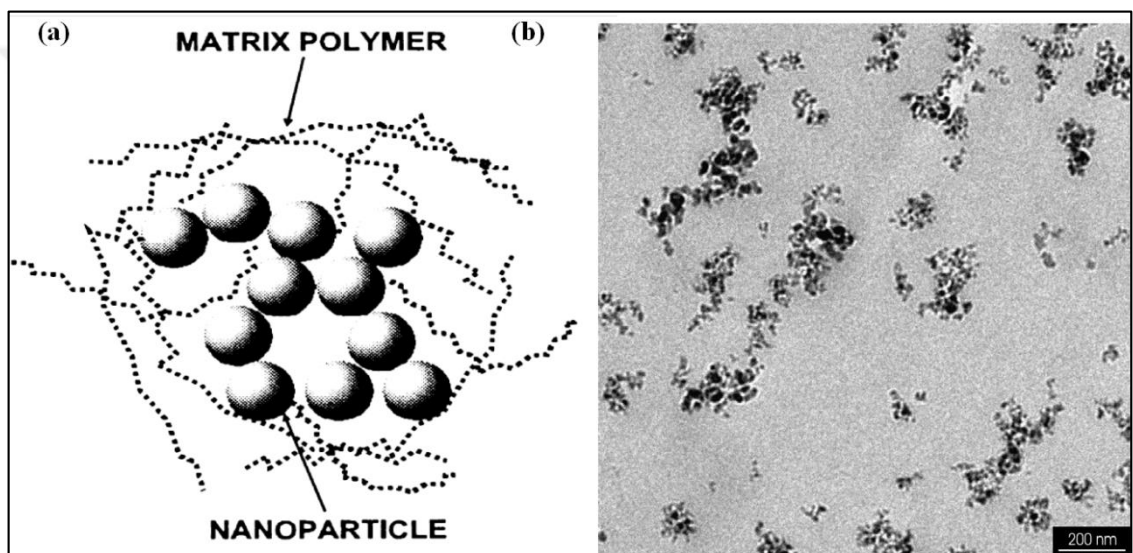


Figure 3.1. (a) Schematic of agglomerated nanoparticles dispersed in polymer matrix [63]; (b) TEM micrographs of Aerosil® R8200 agglomerations in methylmethacrylate (MMA) [64]

induces number of clustered particles in polymer matrix (See Figure 3.1.a). To avoid that kind of accumulations, some researchers focused on altering the nanocomposite synthesis route. The approaches on in-situ polymerization of monomers in the presence of nanoparticles, such as the sol-gel process [65] and the intercalation polymerization technique [66]. Nevertheless, adding surfactants to better disperse nanoparticles is still the simplest and most convenient method.

3.3. PREPARATION ROUTES FOR POLYMER NANOCOMPOSITES

Properties of nanocomposites are directly dependent on several concepts; the properties of the components, shape and volume fraction of the filler, the morphology of the system and the nature of the interphase that is likely to be formed between the two components [67]. Beside the formed interface, as it was mentioned before, the nanoscale particles typically aggregate, which cancels out any benefits associated with the dimension [68] and exhibit properties even worse than conventional particle/ polymer systems [63]. To overcome these handicaps, several methods were developed for preparing polymer nanocomposites, mainly can be classified under two major categories: physical and chemical methods. Physical methods include solvent processing; melt-processing, film casting, polymer intercalation whereas chemical methods cover in-situ processes.

3.3.1. Physical Methods

Melt processing is the most promising and practical method to be used in industry. In melt processing, particles are dispersed into a polymer melt and then polymer nanocomposites are obtained by extrusion. Basically the method consists of annealing of a mixture of the polymer and the inorganic material above the softening point of the polymer, either by static heating or under shear. (See Figure 3.2.a) Diffusion of polymer chains from the bulk polymer and melting into the galleries between the host layers occur during annealing [69, 70]. The process is usually applicable for a wide range of materials such as clays, oxides, and carbon nanotubes [71]. An important strength of this route is; being environmentally benign [72], easy to scale-up and economical advantage that is compatible with industrial usage [71]. However the method is not suitable for olefins [69].

Film casting method, on the other hand, starts with a solution of polymer and host material. Polymer and fillers are mixed, dissolved in a polymer solution and followed by evaporation of the solvent [73]. The solvent evaporation takes place during the coating process; called spin-coating or by subsequent treatment in oven or at ambient temperature.

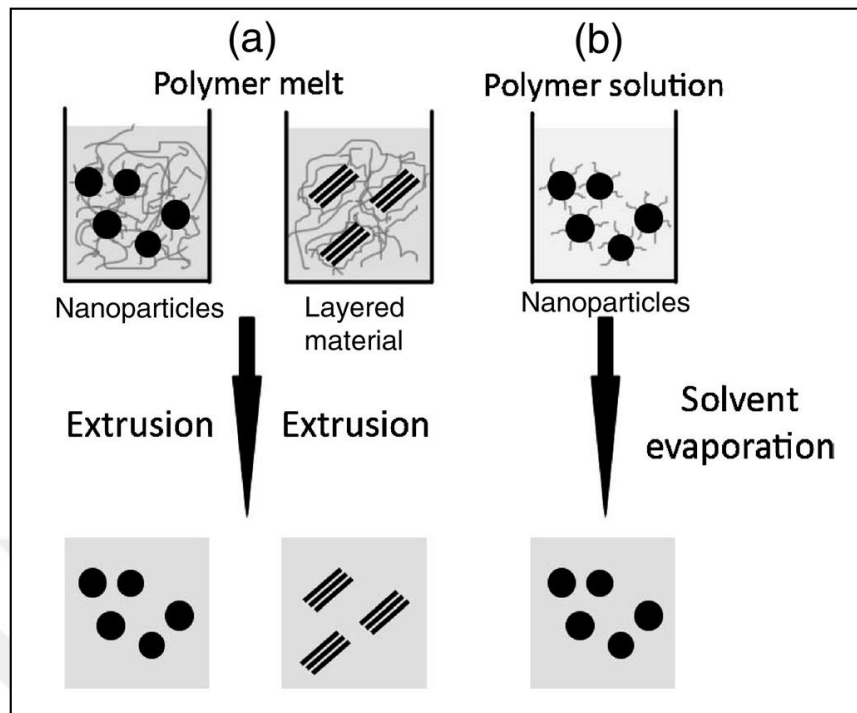


Figure 3.2. Preparation methods for nanocomposites; (a) Melt processing; (b) Film casting [71]

Another method for preparing nanocomposites from polymer solution is intercalation; which is employed for layered reinforcing material in which the polymer may intercalate. Intercalation of the polymer or pre-polymer from solution is mostly used for layered silicates [74, 75]. Resulted nanocomposites can be considered almost homogeneous and have low or even no polarity. Despite the ease of solvent evaporation methods, they cannot be adapted for industrial use due to the need of large amounts of solvents.

3.3.2. Chemical Methods

Direct mixing and melt processing of particles with polymers usually result in a lack of incorporation of fillers and polymers. That phenomenon ends up with agglomeration of particles and makes films look turbid or translucent [71]. To overcome these problems, scientists developed and focused on in-situ polymerization and in-situ nanoparticle formation.

The in-situ polymerization basically involves dispersion of the inorganic nanoparticles directly in the monomer solution prior to a polymerization process [71]. The main handicap for in-situ polymerization would be to obtain stable dispersions by adequate modification of particle surfaces, since the viscosity of the monomer dispersions is comparatively low and sedimentation processes can proceed quickly [76]. The modification of particle surfaces can be achieved by adding amphiphilic molecules, such as stearic acid, oleic acid, oleic amine or long chain alcohols [77, 78] as surfactants and using ‘grafting to’ or ‘grafting from’ methods.

Grafting techniques take advantage of monomers being directly adsorbed to the particle surface. In ‘grafting to’ techniques, polymer chains modified with anchoring groups are used to bind to the particle surface. By reaction of these anchoring groups with functional sites at the particle surface, the polymer can be grafted to the inorganic particle [79]. Organic/inorganic nanocomposite materials can also be produced by “grafting from” techniques by functionalization of inorganic surfaces with initiating groups, starting the polymerization reaction from the inorganic surface [78].

In this work, we employed solvent casting method to prepare nanofilms due to the simplicity of this method. To better disperse the nanoparticles in the polymer matrix during evaporation nanoparticles are coated with a surfactant.

3.4. EXPERIMENTAL

Solvent evaporation method was used to prepare nanofilms. For the neat PEO films, 0.57 g of PEO (PEO, POLYOX™, WSR 205, $M_w=600,000$ g/mol) was dissolved in 15 ml chloroform (Sigma Aldrich, anhydrous, ≥ 99 per cent) and for the NP/PEO films, previously prepared solutions of Au/o or Ag/o NPs (see Chapter 2) were added to these PEO-chloroform solutions at calculated (theoretical) amounts. The solutions were mechanically stirred overnight. The resulting PEO (or NP/PEO) solutions were left for one hour at room temperature to remove any air bubbles that might have occurred. The solutions were then transferred to glass petri dishes ($d = 5$ cm), dried in an oven at 32 °C overnight. The thickness of the resulting films was measured with electronic digital caliper as 0.17 ± 0.03 mm based on 20 samples. The samples were labeled with their corresponding weight percent and are listed in Table 3.1. Volume conversions were done taking densities of the Au NPs (ρ_{Au}), Ag NPs (ρ_{Ag}) and PEO (ρ_{PEO}) to be 19.6 g/cm³, 10.5 g/cm³ and 1.13 g/cm³, respectively.

The distribution of nanoparticles in the polymer matrix was analyzed by TEM and ESEM. In order to prepare samples for TEM (FEI Tecnai Sphera, Voltage: 200kV), carbon coated 200 mesh copper grids were dipped in dilute NP/PEO solutions and left overnight at room temperature. No coating was applied to the samples prior to the ESEM study. Prepared nanofilms were fractured in liquid nitrogen and images were collected from the cross-section of these films with using ESEM (FE-ESEM, Philips XL30 ESEM FEG, Voltage: 4.00 kV, Magnification: 8000x) equipped with an energy-dispersive X-ray spectrometry EDS (EDAX).

FTIR (Perkin Elmer, Spectrum One) measurements were conducted with PEO/Au10 and PEO/Ag10 NP solutions at room temperature in the transmission mode to study the interaction between NPs and PEO chains. Dry KBr powder was placed in an evacuable die and pressed in a manual hydraulic press. Resulted KBr pellets were in 13 mm diameter and 1.5-2 mm thickness. 10 μ l of PEO/NP solutions with different concentrations were dropped and dried on these pellets. Each sample was scanned from 500 cm⁻¹ to 4000 cm⁻¹.

Table 3.1. List of prepared PEO nanocomposites at different concentrations

Sample Label	NP Type	NP Conc. wt (per cent)	Au NP Conc. vol (per cent)	Ag NP Conc. vol (per cent)
Neat PEO	-	0	0	0
PAu/Ag 10-0.01	Au/Ag 10/o	0.01	0.0006	0.0011
PAu/Ag 10-0.03	Au/Ag 10/o	0.03	0.0017	0.0032
PAu/Ag 10-0.1	Au/Ag 10/o	0.1	0.0058	0.0108
PAu/Ag 10-0.3	Au/Ag 10/o	0.3	0.0175	0.0323
PAu/Ag 10-0.5	Au/Ag 10/o	0.5	0.0291	0.0538
PAu/Ag 10-1	Au/Ag 10/o	1	0.0582	0.1076
PAu/Ag 10-2	Au/Ag 10/o	2	0.1164	0.2152
PAu/Ag 30-0.01	Au/Ag 30/o	0.01	0.0006	0.0011
PAu/Ag 30-0.03	Au/Ag 30/o	0.03	0.0017	0.0032
PAu/Ag 30-0.1	Au/Ag 30/o	0.1	0.0058	0.0108
PAu/Ag 30-0.3	Au/Ag 30/o	0.3	0.0175	0.0323
PAu/Ag 10-0.5	Au/Ag 30/o	0.5	0.0291	0.0538
PAu/Ag 10-1	Au/Ag 30/o	1	0.0582	0.1076
PAu/Ag 10-2	Au/Ag 30/o	2	0.1164	0.2152

3.5. RESULTS AND DISCUSSION

The intense color of colloidal gold is due to the surface plasmon band, a broad absorption band in the visible region around 530 nm. The surface plasmon band originates from the excitation of oscillations of the metallic electrons at the surface of the nanoparticles and is therefore evidence of metallic character (See Chapter 7 for further information). As the core size decreases, the absorption band broadens [80] and its intensity decreases sharply due to loss of metallic character. Metal nanoparticles interaction with light is strongly dictated by their environment, size and physical dimensions [81].

For small (~10nm) monodisperse Au nanoparticles the surface plasmon resonance phenomena causes an absorption of light in the blue-green portion of the spectrum (~500

nm) while red light (~700 nm) is reflected, yielding a rich red color. As particle size increases, the wavelength of surface plasmon resonance related absorption shifts to longer, redder wavelengths. Red light is then absorbed, and blue light is reflected, yielding solutions with a pale blue or purple color [80]. Silver nanoparticles, on the other hand, display a color range from yellow to brown color as the size gets larger. As the size of each silver particle gets larger, the color of the suspension ranges from yellow to amber and brown. That is a result of reflection of yellow-brown light (~600 nm) by Ag nanoparticles, similar with Au nanoparticles.

Nanocomposites were prepared through solvent casting method, with simply adding Au and Ag NP colloidal solutions to PEO solution, since it is economical, convenient and easy to scale-up. Different colors of the NP solutions yield red and yellow nanofilms. As the the concentration of the nanoparticles dispersed in nanofilms gets higher, the color of the film becomes darker. Representative pictures of nanofilms are presented in Figure 3.3; low (0.01 per cent, by wt), medium (0.1 per cent, by wt) and high (1 per cent, by wt) concentrations. Since the thickness of the films vary in the wide range, i.e. between 0.14 and 0.20 mm, it is impossible to obtain homogeneous nanoparticle dispersion and same color for each film prepared. To minimize the errors and assure accuracy, appropriate films were selected with visual detection first and the experiments were repeated for several times.

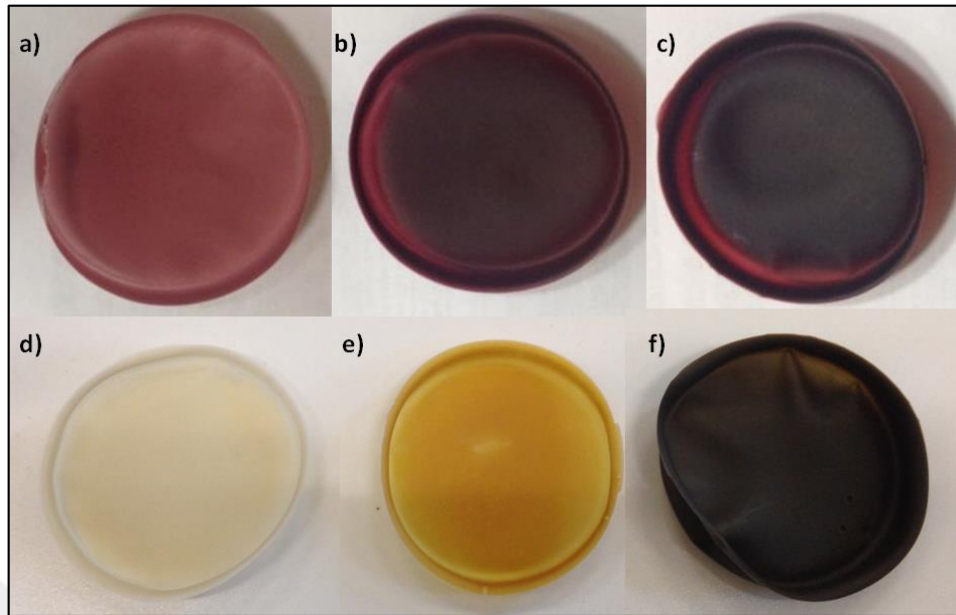


Figure 3.3. Images of prepared nanofilms; (a) PAu10-0.01; (b) PAu10-0.1; (c) PAu10-1; (d) PAg10-0.01; (e) PAg10-0.1; (f) PAg10-1

As the nanoparticles are very small, TEM was used to show dispersed particles in the polymer matrix. For TEM sample preparation, solvent evaporation of polymer solutions was demonstrated on carbon coated 200 mesh copper grids. Grids were dipped into polymer solutions and left to dry. For low concentration of nanoparticles (i.e. 0.01 wt per cent), particles are predominantly dispersed as shown in Figure 3.4. However some aggregated sections can be encountered as circled on the images. As the imaging is done by drying on the TEM grid, aggregation can also be results of an inevitable artifact.

When the concentration of particles is increased, aggregation is expected and ESEM is used to show the aggregates formed. ESEM is a better imaging technique to show larger structures. Images were taken from cross-section of the polymer matrix, which were obtained via fracturing the nanofilms in liquid nitrogen. For higher concentration of nanoparticles (i.e. 1 wt per cent), large nanoparticle clusters in the matrix can be seen in Figure 3.5.

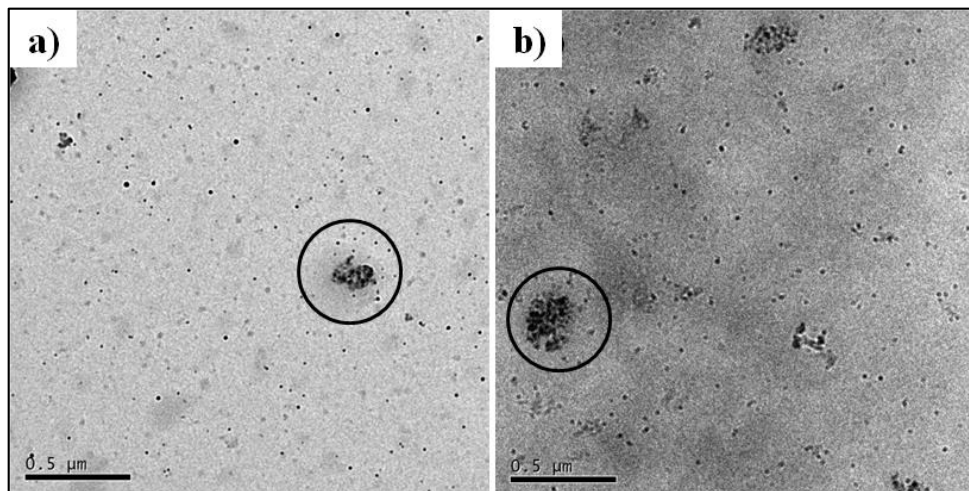


Figure 3.4. TEM images for (a) P Au10-0.01 and (b) P Ag10-0.01 nanofilms

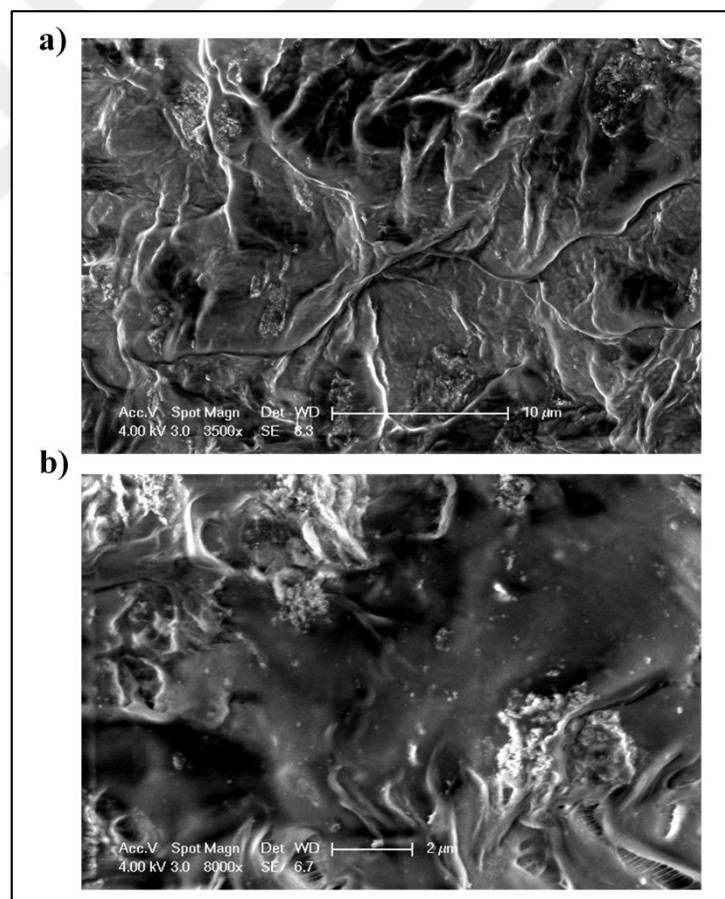


Figure 3.5. ESEM images for (a) P Au10-1 and (b) P Ag10-1 nanofilms

Nanoparticle agglomeration is the most common problem for nanocomposite experimental research. In a typical two phase system, as in nanofillers dispersed in polymer matrix, surface tension at the interface results in a greater attraction of nanoparticles to each other. The tendency of nanoparticles to decrease their interface area within polymer molecules will cause particle agglomeration yielding a phase separation [82]. The most common method for reducing surface energy is use of surfactants. Organic surfactants such as oleylamine and oleic acid are generally utilized and put in a reaction with metal salts; since they both act as reducing and stabilizing agents [17, 18]. Oleylamine and oleic acid are amphiphilic molecules having both hydrophilic heads & hydrophobic tails (Figure 2.9.a) and tie to NP surface via heads as mentioned before. It can be thought as in reverse micelle configuration. Intermolecular forces between 'head' of the surfactants, $-\text{NH}_2$ and $-\text{COOH}$, forms a hydrodynamic layer around the nanoparticle molecules, enabling them to stay dispersed in polymer matrices.

However, uniform distribution of nanoparticles cannot be achieved even with the addition of surfactants above a threshold nanoparticle concentration. The agglomerations can be explained with some possible reasons; (1) PEO is soluble in water as well as in organic solvents like toluene and chloroform. The amphiphilicity of PEO comes from the molecular structure. The backbone of PEO consists of both ethylene ($-\text{CH}_2-\text{CH}_2-$) and ethylene oxide ($-\text{CC}-\text{O}-\text{CC}-\text{O}-$) groups representing hydrophobic and hydrophilic sides respectively [38]. The repulsion between hydrophobic surfactant chains and hydrophilic groups of PEO causes phase separation. (2) The second reason is again related with the first one. With the increase of nanoparticle concentration, the attractions between the nanospheres get dominated and they lose their ability to be exfoliated.

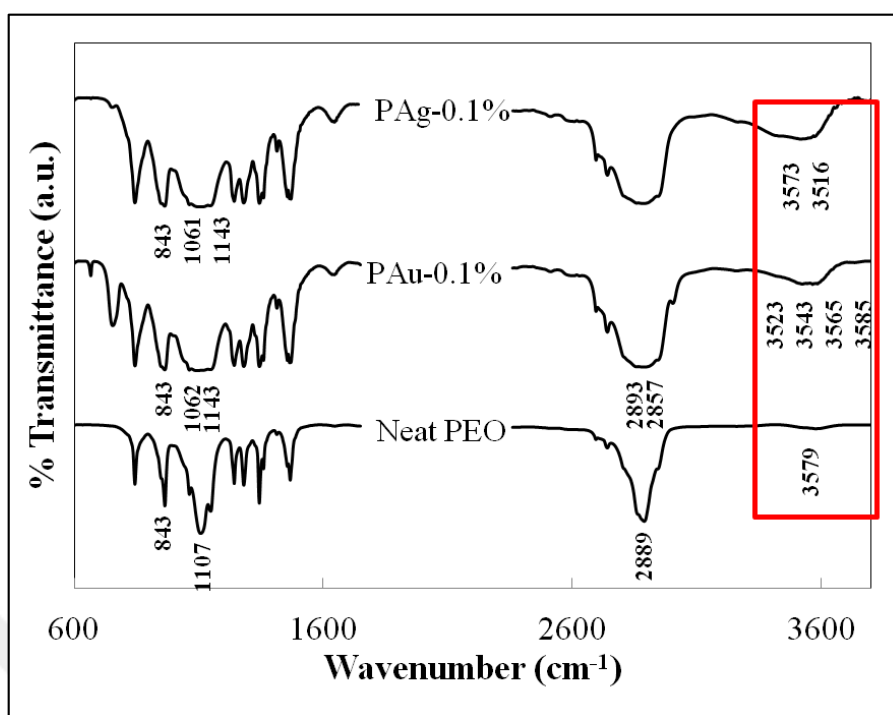


Figure 3.6. FTIR spectra of PAu10-0.1, PAg10-0.1 and neat PEO

In order to understand the interactions between polymer chains and nanoparticles, FTIR experiments were performed. FTIR spectra of PAu10 and PAg10 nanocomposites having a NP concentration of 0.1 per cent (by wt) and their comparison with neat PEO is shown in Figure 3.6. The strongest bands emerge between 1050 cm^{-1} and 1150 cm^{-1} , 2650 cm^{-1} and 3000 cm^{-1} represents the C-O-C stretching and asymmetric CH₂ stretching respectively. The sharp bands around these two locations broaden with addition of nanoparticles for both PAu10 and PAg10 nanocomposites. The peak at 843 cm^{-1} is another characteristic peak responsible for CH₂ rocking. Except these specific regions, the broad band at 3579 cm^{-1} which is assigned for hydroxyl groups [83] is a specific interest for this study. The increase in the transmittance of this band with addition NPs might be due to strong intramolecular forces between H atoms in surfactants and O atom of PEO.

3.6. CONCLUSION

Addition of nanofillers to polymers has been increasing interest for several years due to the enhanced mechanical, thermal and optical properties of resulting nanocomposites. In this chapter, PEO-based nanocomposites were prepared and characterized for further applications. Solvent casting method was employed among the other nanocomposite synthesis routes because of the simplicity. Previously synthesized Au and Ag nanoparticle solutions were directly added to PEO/chloroform solutions at different concentrations varying from 0.01 to 2 per cent (by wt). The nanoparticles were already capped with oleic acid and oleylamine surfactants; therefore possible agglomerations were avoided.

For the nanofilms which have lower nanoparticle concentrations, TEM imaging was used to monitor the dispersion of Au and Ag NPs in polymer matrix. Although some agglomerations due to drying on TEM grid were detected in images, it was found that almost homogeneous dispersion was achieved for the nanofilms with NP concentration of 0.01 per cent (by wt). However, ESEM experiments performed on PAu10-1 and PAg10-1 nanofilms revealed that, the formation of nanoparticle clusters between PEO layers are predominant for nanofilms with higher NP concentration. Therefore the use of surfactants could not exfoliate the neighboring fillers after certain concentration and result accumulation of Au and Ag NPs in polymer matrix. FTIR characterization was also conducted on prepared nanofilms. The most significant difference between the spectra neat PEO and PEO-based nanocomposite was observed around 3600 cm^{-1} that is more likely to be caused from interaction between oxygen atom of PEO and hydrogen atom of surfactant molecules.

Hence, the nanocomposites were successfully prepared and found to have good NP dispersion up to certain concentration. Solvent casting method can be easily applied for preparing PEO/Au and PEO/Ag nanofilms and resulted films can be used for further applications.

4. MECHANICAL AND THERMAL PROPERTIES OF PEO/AU AND PEO/AG NANOCOMPOSITES

4.1. INTRODUCTION

Fillers play important roles in modifying the structural, mechanical and thermal properties of nanocomposites, as a matter of fact; with lower cost. Such properties can indeed be enhanced and tailored by changing the volume fraction, shape, and size of the filler particles [84-86]. A further improvement of the mechanical properties can be achieved by using nanofiller materials with a larger aspect ratio. The interaction between fillers and polymer matrix will be stronger if the filler has dimensions in nano scale, because the interfacial area of the particles is larger. Therefore stiffness in a polymer matrix could lead to higher mechanical performances [87].

Several researchers study influence of Au and Ag NPs on thermal and mechanical properties of polymers. El-Shamy et al. prepared nanocomposite films by using poly (vinyl alcohol) (PVA) and Ag NPs at different concentrations (0-1.5 per cent, by wt). A maximum of increase in young's modulus (almost 20 times) in presence of nanofillers was recorded for films having concentration of 1.5 per cent, by wt of Ag [88]. Similarly, Montazami et al. prepared liquid crystal elastomers (LCE) doped with different Au NPs with various concentrations (0, 0.024, 0.048 and 0.096 per cent, by mol) and performed DMA experiments by using tensile clamp. They found an enhancement in young's modulus of LCE at around 100 per cent [62]. On the other hand, Pandis et al. synthesized 5.6 nm sized Ag nanoparticles and dispersed them into the poly (methylmethacrylate) (PMMA) matrix by changing concentration of Ag from 0 to 0.5 per cent (by wt). However, after applying mechanical tests, they pointed out that young's modulus of the sample slightly decreases with addition of Ag NPs [61].

Glass transition temperature (T_g), on the other hand, gives information on dynamics and thermal behavior of polymers. Researchers configured experiments on polymers in presence of nanofillers and presented a relation between polymer mobility and T_g [60, 61]. To illustrate this relation, Kim et al., synthesized Au/polystyrene nanocomposites with

increasing nanoparticle concentration and concluded that, T_g of the nanocomposites decreases gradually compared to pure polystyrene as the nanofiller amount increases [60]. In the work of Pandis et al., glass transition of the Ag/PMMA nanocomposites was also investigated. They presented that, T_g of polymer nanocomposites decreases by 10 °C as the nanoparticle amount increases [61]. Yet again, Sun et al., prepared Ag nanopowders with an average diameter of 65 nm. Obtained Ag nanopowders were blended with epoxy resin at different weight percentages as; 68, 72, and 75 per cent [89]. They showed that, as the nanofiller concentration increases, T_g approximately decreases by 7° C. On the contrary, Feyzi et al. found an increase of 5 °C in T_g of polyimide matrix with addition of Ag NPs [90].

In this chapter, dynamic mechanical analysis and differential calorimetric scan tests were performed on previously prepared PAu and PAg nanofilms. The details of mechanical and thermal testing of polymers are presented. Dynamic tests enabled us to compare the effect of type, size and concentration of the nanoparticles on mechanical properties, glass transition temperature and crystallinity of neat PEO.

4.2. THERMOMECHANICAL PROPERTIES OF POLYMERS

There are some parameters discussed in material science those influence mechanical properties of polymers and polymer nanocomposites. These parameters can be listed as; temperature, strain rate, chain entanglement, strong intermolecular bonding, heat treatment, molecular weight of the polymer, degree of crystallinity, molecular configurations such as geometrical and stereoisomerism [91]. A variety of methods are used to determine mechanical performance of polymer films under a variety of loading conditions. These may be classified as static (i.e., tensile and shear), transient (i.e., creep and stress relaxation), impact (i.e., Izod and Charpy) and cyclic (i.e., fatigue) tests [92]. Static tests are used to measure the force response when a sample is strained, compressed, or sheared at constant rate. The one who wants to study and test the mechanical properties of polymers via static tests should define various topics such as; modulus of elasticity, tensile strength, yield, compliance and elongation to failure. Three important parameters related to thermal properties of polymers are melting, glass transition temperature and crystallization.

4.2.1. Tensile Properties

Static tests refer to those for which the deformation rate is steady in time. While tensile, compressive, or shear modes may be employed, tensile testing is the most common. In a typical tensile test, a polymer sample, is clamped at one end and pulled at a constant rate of elongation at the other clamped end. A static force (F) is applied to the specimen, and the response of the film is recorded in terms of stress and strain functions [93].

Usually tensile response is plotted as engineering (nominal) stress (σ) vs. engineering strain (ϵ), where;

$$\sigma = \frac{F}{A} \quad (4.1)$$

and

$$\epsilon = \frac{\Delta L}{L_0} \quad (4.2)$$

where; A_0 is the original (undeformed) cross-sectional area of the gage region and ΔL is the change in sample gage length ($L-L_0$) due to the deformation. L_0 stands for the narrow region of the tensile specimen, also called initial gage length (See Figure 4.1)

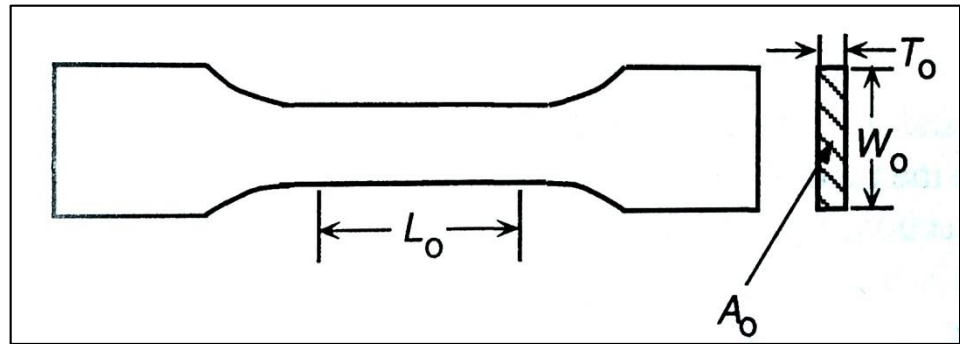


Figure 4.1. Illustration of typical tensile sample [93]

Basic stress-strain behavior found for polymeric materials can be seen in Figure 4.2.a. Red curve (A) illustrates the stress-strain character for a brittle polymer, as it fractures while deforming elastically. The behavior for a plastic material, the blue curve (B), the initial deformation is elastic, which is followed by yielding and a region of plastic deformation. Finally, the deformation displayed by green curve (C) is totally elastic; this rubber-like elasticity (large recoverable strains produced at low stress levels) is displayed by a class of polymers termed the elastomers [91]. Hooke's law for ideal elastic films provides a relationship between stress and strain for tensile deformation as;

$$\sigma = E\varepsilon \quad (4.3)$$

where the proportionality factor, E , is defined as tensile (or Young's) modulus which is a measure of stiffness of the material. Conversely, the strain and stress are related by the tensile compliance, J , defined by;

$$\varepsilon = J\sigma \quad (4.4)$$

Therefore, for tensile deformation, the compliance is reciprocal of the modulus [94].

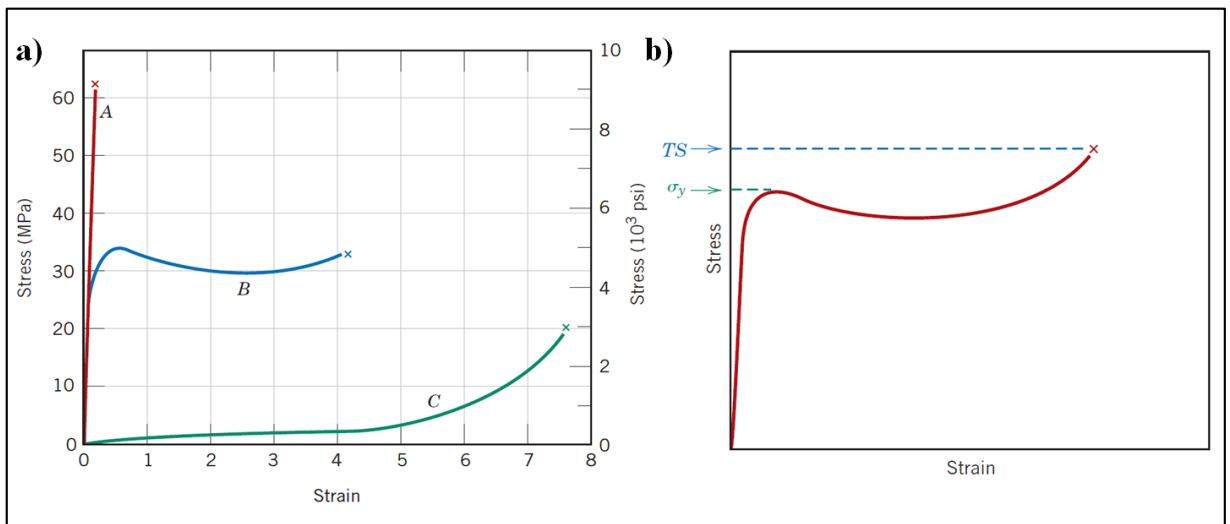


Figure 4.2. (a) The stress-strain behavior for brittle (curve A), plastic (curve B) and highly elastic (elastomeric) (curve C) polymers; (b) Schematic stress-strain curve for a plastic polymer [91]

For plastic polymers (curve B, Figure 4.2.a), the yield point is taken as a maximum on the curve, which occurs just beyond the termination of the linear-elastic region (Figure 4.2.b). The stress at this maximum is the yield strength (σ_y). Furthermore, tensile strength (TS) corresponds to the stress at which fracture occurs (Figure 4.2.b); TS may be greater than or less than yield strength. Strength, for these plastic polymers, is normally taken as tensile strength [95].

4.2.2. Viscoelastic Properties

Polymeric materials can also be experimented via tensile tests under varying temperature or altered frequency of stress. Using these techniques, viscoelastic behavior of the specimen can be determined. It is established via recording the time-dependent response of a polymeric solid, melt, or solution to a periodic perturbation such as the application of a sinusoidal strain or an electrical voltage. The most commonly used method to measure viscoelastic properties as a function of temperature and time (frequency) is dynamic-mechanical analysis, which records the stress response to an application of a sinusoidal strain [96].

For a tensile strain that is a sinusoidal function of time, t , the strain function may be expressed as;

$$\varepsilon = \varepsilon^{\circ} \sin(\omega t) \quad (4.5)$$

In this expression, ε° is the amplitude of applied strain and ω is the angular frequency of oscillations (rad/s). The angular frequency is related to frequency, f , measured in cycles per second, or Hz, as $\omega = 2\pi f$ [96].

The stress resulting from the applied sinusoidal strain will also be a sinusoidal function, which may be written as;

$$\sigma = \sigma^{\circ} \sin(\omega t + \delta) \quad (4.6)$$

Where σ° is the amplitude of stress response and δ is the phase angle between the stress and the strain illustrated by Figure 4.3.

If the material being evaluated is purely elastic, the phase difference between the stress and strain sine waves is 0° (i.e., they are in phase). If the material is purely viscous, the phase difference is 90° . However, most real-world materials including polymers are viscoelastic and exhibit a phase difference between those extremes. This phase difference, together with the amplitudes of the stress and strain waves, is used to determine a variety of fundamental material parameters, including storage and loss modulus and $\tan \delta$, etc. [97] While storage modulus (E') is ability to store energy of a polymer representing the elastic response and found as;

$$E' = \left(\frac{\sigma^{\circ}}{\varepsilon^{\circ}} \right) \cos(\delta) \quad (4.7)$$

and loss modulus (E'') characterizes the viscous behavior of a material and given as;

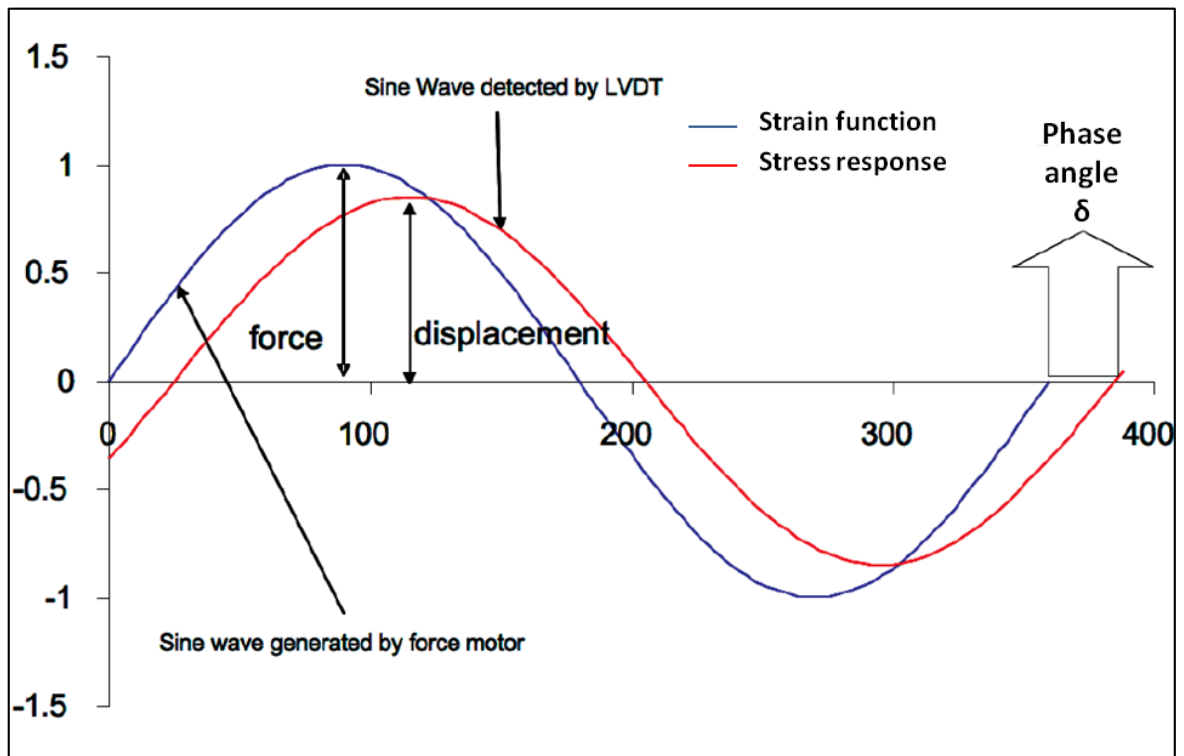


Figure 4.3. Representation of an arbitrary strain function and resulting stress response of a viscoelastic material [97]

$$E'' = \left(\frac{\sigma^{\circ}}{\varepsilon^{\circ}} \right) \sin (\delta) \quad (4.8)$$

The ratio of loss and storage modulus defines another parameter, $\tan \delta$, where;

$$\tan \delta = \left(\frac{\sin \delta}{\cos \delta} \right) = \frac{E''}{E'} \quad (4.9)$$

4.2.3. Melting and Glass Transition Temperature

Melting (T_m) and glass transition (T_g) temperatures are important parameters relative to applications of polymers. They define, respectively, the upper and lower temperature limits for numerous applications, especially for semi-crystalline polymers, and most of the synthetic and natural polymers are semi-crystalline. T_g may also define the upper use temperature for glassy amorphous materials [91]. Furthermore, and also influence the fabrication and processing procedures for polymers and polymer-matrix composites.

During melting of a polymer there will be a rearrangement of the molecules in the transformation from ordered to disordered molecular states. On the other hand, upon heating through the glass transition temperature, the amorphous solid polymer transforms from a rigid to a rubbery state. Correspondingly, the molecules that are virtually frozen in position below begin to experience rotational and translational motions. Thus, the values of T_g and T_m will depend on molecular characteristics that affect chain stiffness [95].

Referring to Figure 4.4; for the crystalline material (blue, C), there is a discontinuous change in specific volume at the T_m . The curve for the totally amorphous material (red, A) is continuous but experiences a slight decrease in slope at the glass transition temperature, The behavior is intermediate between these extremes for a semicrystalline polymer (green, B) in that both T_m and T_g phenomena are observed. T_m and T_g are properties of the respective crystalline and amorphous phases in this semicrystalline material. But it should be noted that no engineering polymer is 100 per cent crystalline; curve C is included in Figure 4.4 to illustrate the extreme behavior that would be displayed by a totally crystalline material [91].

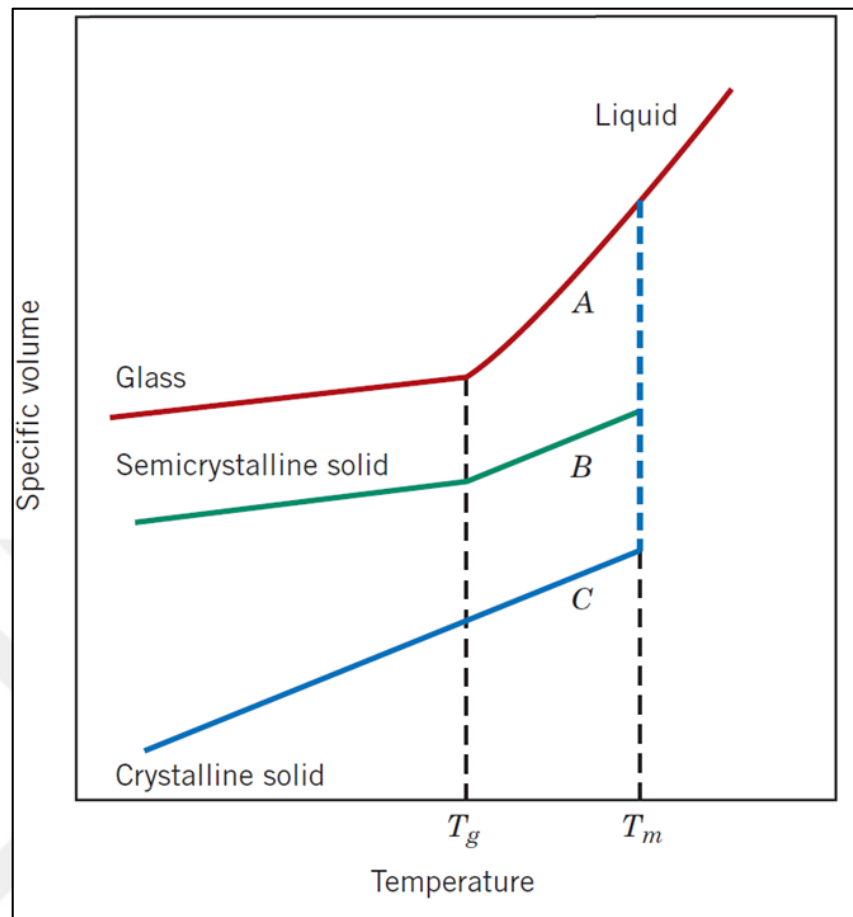


Figure 4.4. Specific volume vs. temperature plots upon cooling from the liquid melt for totally amorphous (A), semicrystalline (B) and crystalline (C) polymers [91]

4.2.4. Crystallinity of Polymers

The third important phenomena related to thermal properties of polymers beside T_m and T_g is crystallization. An understanding of the mechanism and kinetics of polymer crystallization is important because the degree of crystallinity directly influences the mechanical and thermal properties of these materials.

The crystallization of a molten polymer occurs by nucleation and growth processes. For polymers, upon cooling through the T_m , nuclei form wherein small regions of the tangled and random molecules become ordered and aligned in the manner of chain-folded layers. At temperatures in excess of the melting temperature, these nuclei are unstable due to the thermal atomic vibrations that tend to disrupt the ordered molecular arrangements.

Subsequent to nucleation and during the crystallization growth stage, nuclei grow by the continued ordering and alignment of additional molecular chain segments; that is, the chain-folded layers remain the same thickness, but increase in lateral dimensions (Figure 4.5.a), or for spherulitic structures (Figure 4.5.b) there is an increase in spherulite radius [95].

The crystallinity, also defined as the ratio of crystalline regions dispersed in amorphous chains, can be obtained via several methods. If the density of totally amorphous (ρ_a) and totally crystalline (ρ_c) sample are known or can be estimated, then fractional crystallinity (ϕ) can be determined as follows;

$$\phi = \frac{\rho - \rho_a}{\rho_c - \rho_a} \quad (4.10)$$

X-Ray diffraction is a widely used technique of polymer characterization that can provide information concerning both the crystalline and amorphous states. Also, differential scanning calorimeter (DSC) gives information on per cent crystallinity via measuring the change in enthalpy, i.e. amount of heat that is absorbed or released by a substance undergoing physical or a chemical change. Per cent crystallinity (X_c) can be estimated using formula above;

$$X_c = \frac{\Delta H_m}{\Delta H_m^o} \times 100 \quad (4.11)$$

where ΔH_m^o is the theoretical heat of melting of 100 per cent crystalline PEO, and recorded as 197 J/g by Wunderlich et al. [98]. However previous studies showed that, crystallinity of polymers measured based on the assumption of two-phase structure indeed not be the case. The existence of intermediate non-crystalline phase is also considered at crystallinity from Raman spectroscopy measurements [99] and will be discussed at Chapter 6.

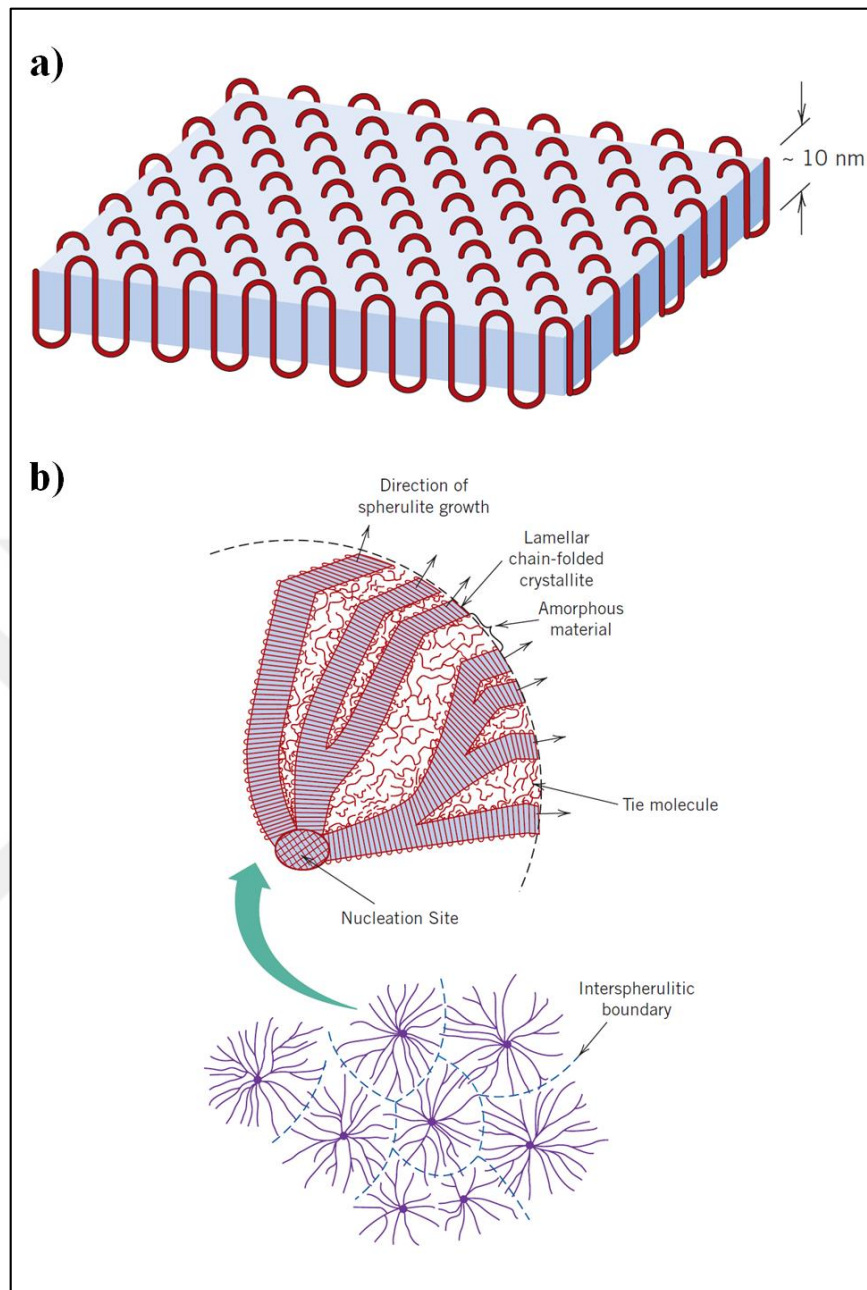


Figure 4.5. The schematic representation of (a) The chain folded structure; (b) Spherulite

[91]

4.3. EXPERIMENTAL

Previously prepared PEO/Au and PEO/Ag nanofilms (see Chapter 2) were subjected to mechanical tests those were performed on a TA Instruments Dynamic Mechanical Analyzer (DMA) equipped with liquid nitrogen cooling tank. Two types of experiments were performed; isothermal and temperature scan tests. Tensile clamp which has a movable lower clamp positioned under the fixed clamp was used for both of the measurements. Each experiment was repeated four to six times in order to assure the accuracy. Isothermal tests were performed at 32 °C applying a static force starting from 0.010 N to 18 N with 0.5 N/min ramp. Compliance (J) was presented with taking the reciprocal of Young's Modulus (E), which is obtained from slope of elastic part of stress vs. strain curve. Temperature scan tests were performed with varying the temperature from -100 °C to 100 °C with 5 °C/min increments at constant frequency, 1 Hz. Storage modulus (E') and loss modulus (E'') values were recorded and glass transition temperature (T_g) was read from E'' vs. time charts.

Differential scanning calorimetry (DSC) measurements were performed using a Setaram DSC 131 apparatus. 30 μ l crucibles were used for sample holding and the weight of the samples were varied between 5-8 mg. Nitrogen gas was purged through the DSC crucible during the experiments and samples were pre-heated from 25 °C to 100 °C, then pre-cooled from 100 °C to 25 °C with 10 °C /min rate in order to neglect the thermal history. Thermally equivalent samples were heated from 25 °C to 100 °C with 10 °C /min rate and this time melting enthalpies (ΔH_m) were calculated from the area under the second heating curve (See Figure 4.6) and each value was averaged from three to five samples.

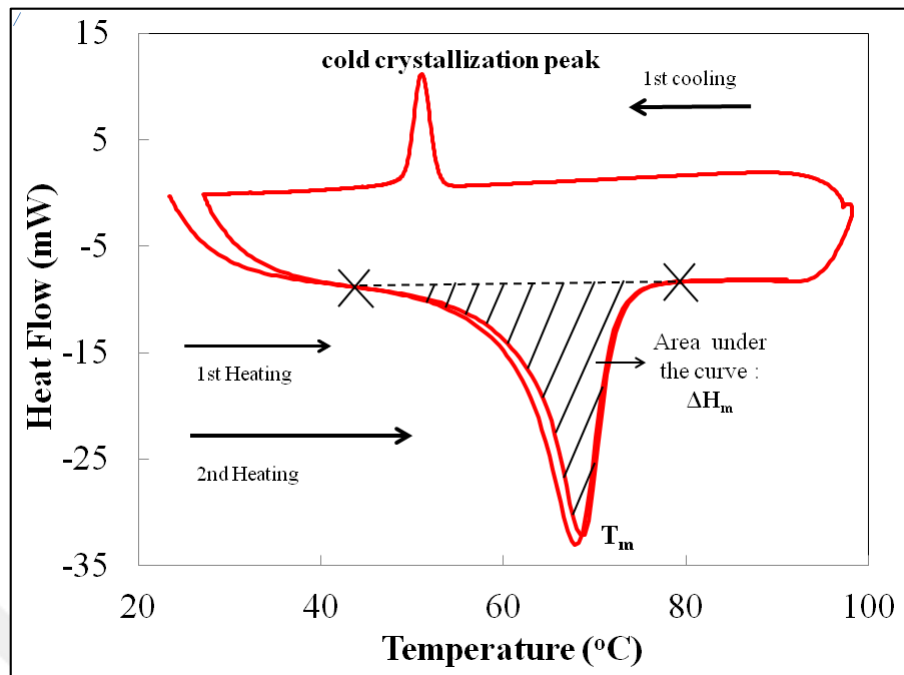


Figure 4.6. Schematic illustration of DSC experimental procedure

4.4. RESULTS AND DISCUSSION

4.4.1. Stress vs. Strain Curves for PAu10-30 and PAg10-30 Nanocomposites

The tensile tests (isothermal experiments) were carried out at 32 °C at which polymer is in solid state. The strain of PEO nanofilms containing different concentrations of Au and Ag NPs with size of 10 nm and 30 nm was measured as a function of stress applied parallel to the long axis of the films. Therefore, we could discuss and compare the effect of size of the NPs on mechanical properties.

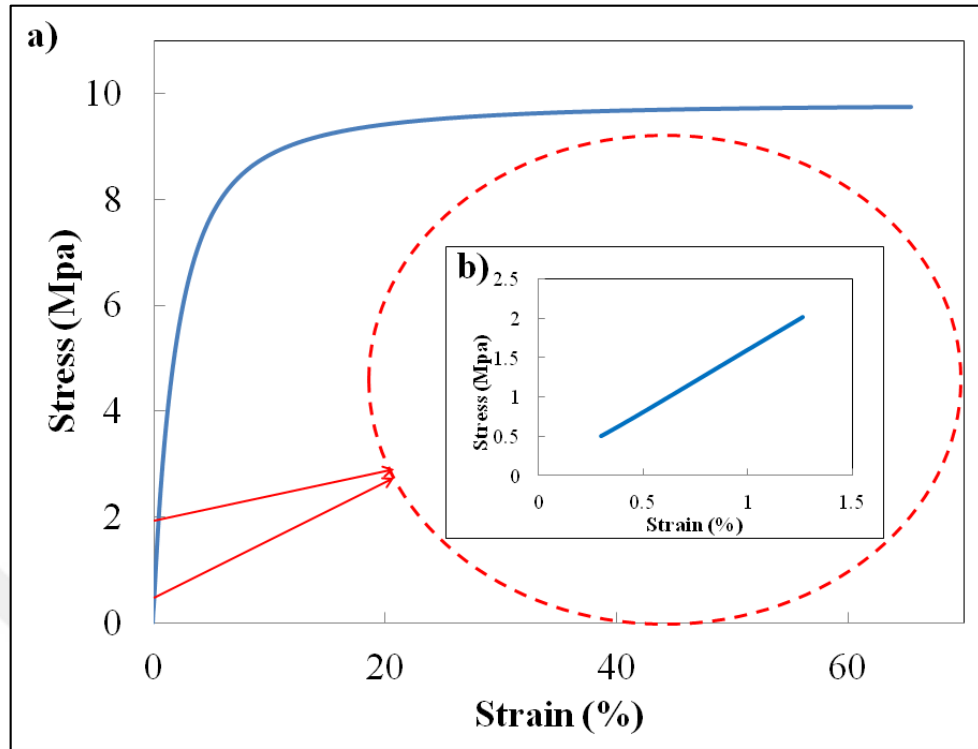


Figure 4.7. (a) Stress vs. strain curve for neat PEO; (b) Elastic part of the stress vs. strain curve of neat PEO

Figure 4.7.a displays the stress vs. strain curve for neat PEO at 32 °C. By looking at the chart, plastic behavior of PEO can obviously be seen; deformation is initially elastic (almost up to 2 MPa of stress applied) and followed by plastic region. The length of the film was found to extend to 165 per cent of its initial value and then fractures. The deformation during the elastic part is reversible, but it is not possible to recover the shape after the sample starts being deformed plastically. The figure above shows the representative stress strain behavior of PEO film, but the average value for more than three measurements are presented in Table 4.1.

It is known that, the slope of the elastic part of the curve gives young's modulus and reciprocal of the modulus of elasticity is named as compliance. In order to standardize all the measurements, the points those are between 0.5 MPa to 2 MPa of stress were encountered in elastic region. The linear part of the elastic region can be seen in Figure 4.7.b. When the stress, strain data were plotted for PAu and PAg nanocomposites, it was found that the slope of the curve changes, however plastic behavior remains same with

neat PEO. Figure 4.8 and 4.9 shows the charts of tensile experiments performed on PAu10, PAg10, PAu30 and PAg30 nanofilms. Note that; plots only show the elastic part of data collected; stress range between 0.5 -2 MPa and strain values were shifted in x-axis for better visualization.

The increase in the Au10 content from 0 to 0.3 per cent (by wt) resulted 59 per cent of decrease in compliance; implying an increase in stiffness of PEO. Similar trend was also observed for tensile strength values. For the PAu10-0.1 films, presence of gold nanoparticles made an improvement in tensile strength of PEO from 8.81 MPa to 10.21 MPa, which is about 15.9 per cent. On the other hand, addition of Ag10 to PEO, led to an enhancement of 50.8 per cent (for PAg10-0.1) in young's modulus and 13.2 per cent (for PAg10-0.03) in tensile strength of PEO. However, the increase in stiffness and strength of the nanofilms reached plateau after certain concentration (0.3 and 0.1 %, by wt, for PAu10 and PAg10; 0.5 and 0.1 %, by wt, for PAu30 and PAg30). In any case, the parameters for nanofilms with high Au10 and Ag10 NP concentration are found better than of neat PEO's.

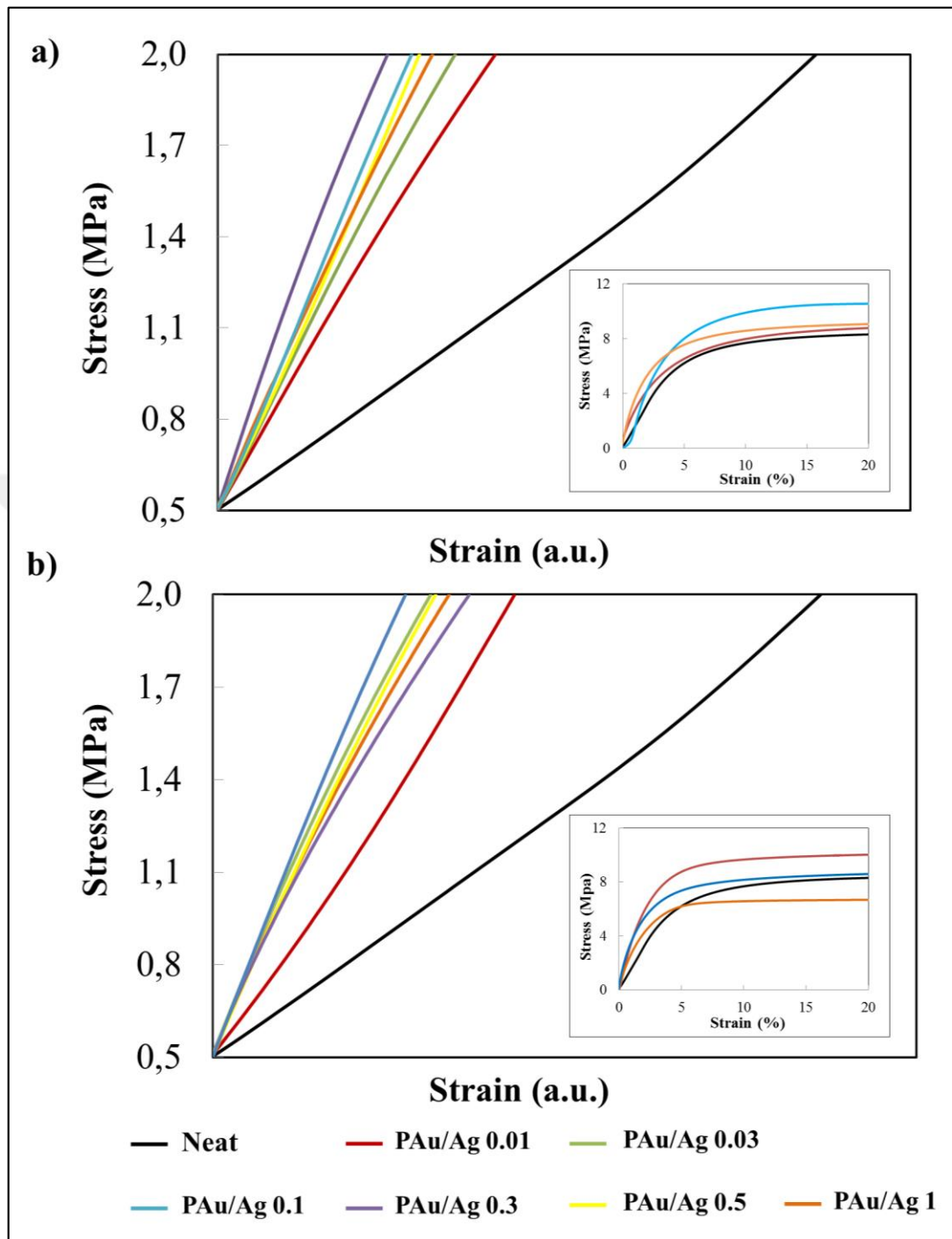


Figure 4.8. Representative plots showing stress strain behavior for (a) PAu10 and (b) PAg10 nanocomposites at different concentrations

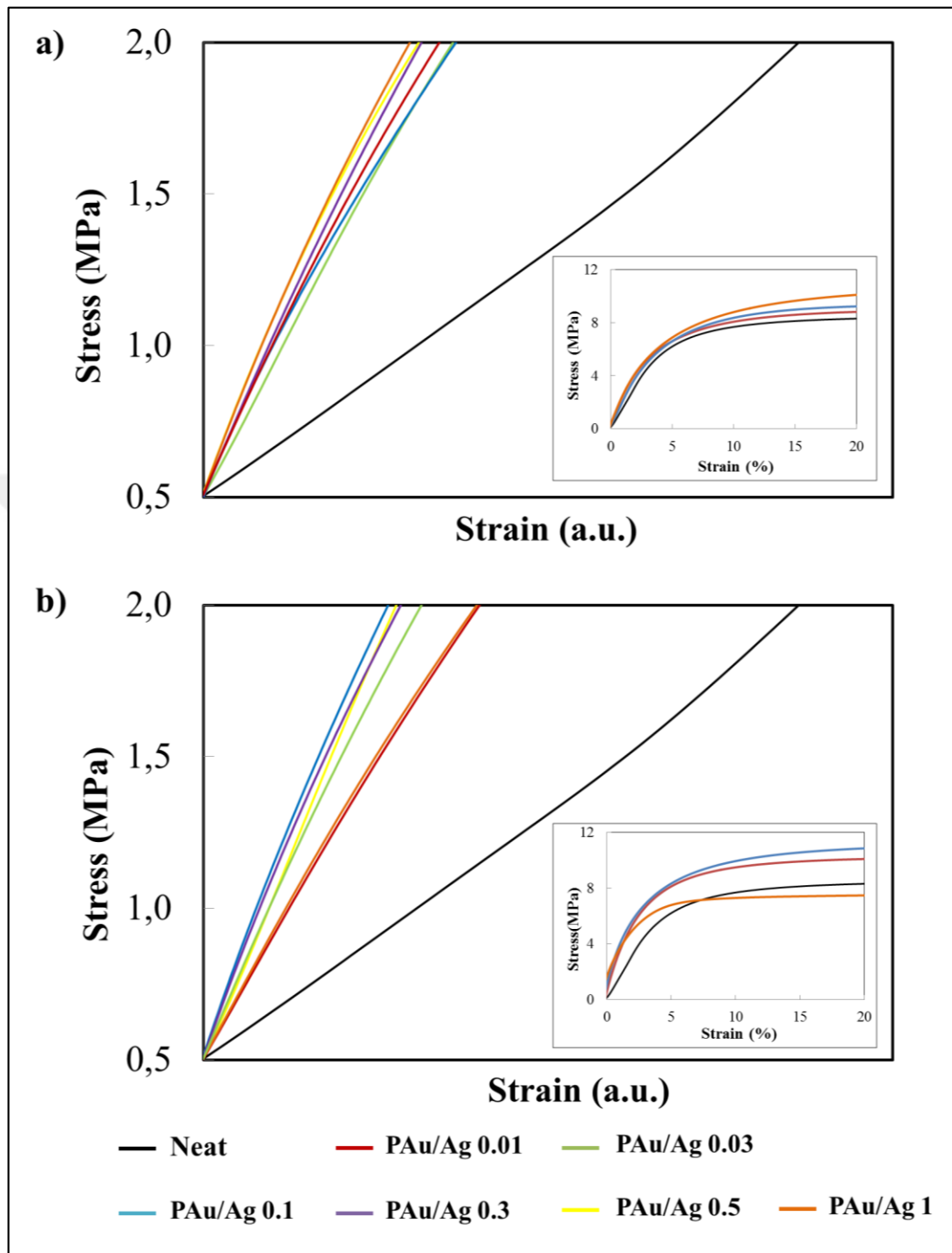


Figure 4.9. Representative plots showing stress strain behavior for (a) PAu30 and (b) PAg30 nanocomposites at different concentrations

Table 4.1. Isothermal DMA results

Sample Name	J (MPa ⁻¹)	TS (MPa)	Sample Name	J (MPa ⁻¹)	TS (MPa)
Neat PEO	0.61 ± 0.03	8.81 ± 0.43	Neat PEO	0.61 ± 0.04	8.81 ± 0.43
PAu10-0.01	0.51 ± 0.15	9.42 ± 0.46	PAu30-0.01	0.38 ± 0.02	8.18 ± 0.59
PAu10-0.03	0.42 ± 0.03	8.90 ± 0.04	PAu30-0.03	0.44 ± 0.14	9.38 ± 0.94
PAu10-0.1	0.26 ± 0.01	<u>10.21 ± 0.31</u>	PAu30-0.1	0.39 ± 0.01	9.40 ± 0.44
PAu10-0.3	<u>0.25 ± 0.02</u>	10.19 ± 0.26	PAu30-0.3	0.39 ± 0.15	9.59 ± 0.74
PAu10-0.5	0.27 ± 0.01	9.70 ± 0.19	PAu30-0.5	<u>0.34 ± 0.03</u>	9.93 ± 0.89
PAu10-1	0.29 ± 0.02	9.45 ± 0.25	PAu30-1	0.34 ± 0.08	<u>10.33 ± 0.97</u>
PAg10-0.01	0.44 ± 0.11	9.04 ± 0.17	PAg30-0.01	0.54 ± 0.31	10.23 ± 1.62
PAg10-0.03	0.33 ± 0.07	<u>9.97 ± 1.77</u>	PAg30-0.03	0.32 ± 0.08	10.18 ± 1.06
PAg10-0.1	<u>0.30 ± 0.03</u>	9.54 ± 0.42	PAg30-0.1	<u>0.28 ± 0.03</u>	<u>10.40 ± 1.07</u>
PAg10-0.3	0.42 ± 0.01	7.59 ± 0.02	PAg30-0.3	0.30 ± 0.04	8.92 ± 0.65
PAg10-0.5	0.33 ± 0.03	7.81 ± 0.15	PAg30-0.5	0.30 ± 0.05	8.55 ± 1.02
PAg10-1	0.36 ± 0.01	5.98 ± 0.73	PAg30-1	0.42 ± 0.01	7.55 ± 0.52

The increase in diameter of the particles from 10 to 30 nm made mechanical properties improved, but no significant change was observed between PAu/Ag10 and PAu/Ag30 nanocomposites. While addition of Au10 NPs to PEO result an increase in young's modulus by 59 per cent, maximum 44.3 per cent of enhancement was found for PAu30 nanofilms. Accordingly, the increase of Ag NP size from 10 to 30 nm changed the enhancement in mechanical properties from 50.8 to 54.1 per cent.

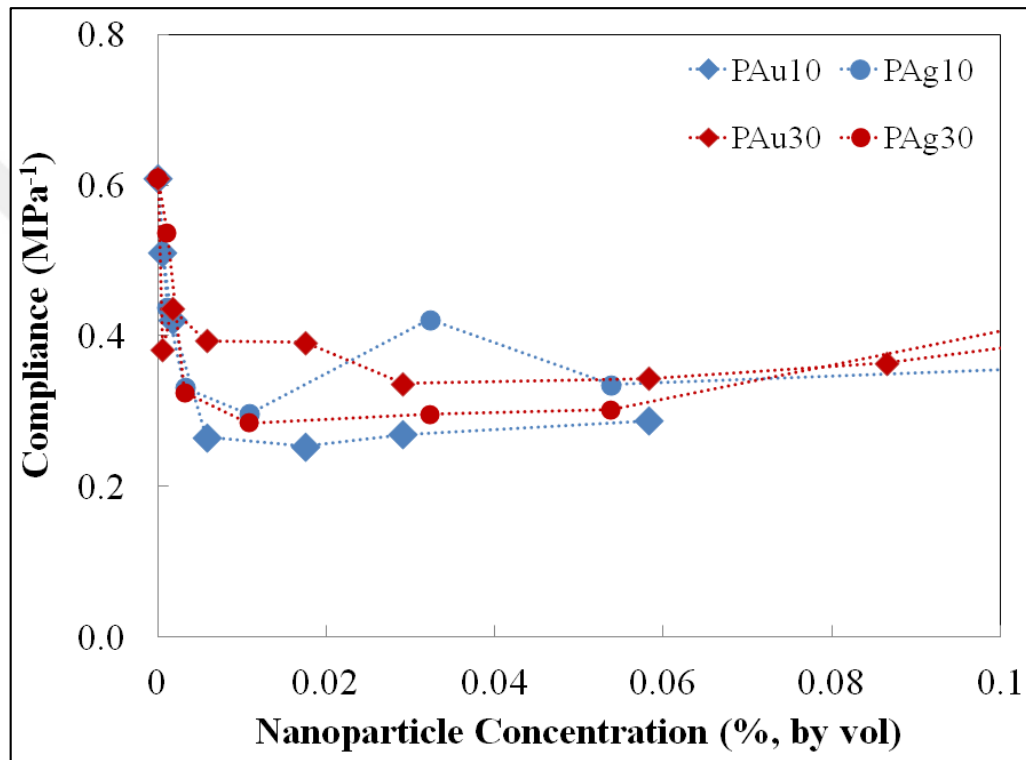


Figure 4.10. Compliance as a function of nanoparticle concentration for PAu and PAg nanofilms

The increase in stiffness and strength of PEO was found to increase with addition of NPs, regardless of nanoparticle type or size. By looking at the data plotted in Figure 4.10, it can be said that addition of both Au and Ag NPs to PEO at some concentration (≈ 0.006 per cent, by vol) made an enhancement in young's modulus of PEO. But, after certain concentration, the increase reaches plateau. The reason behind it originates from the possible agglomerations; those are attributed to phase separation between nanoparticles and polymer matrix after addition of certain amounts of nanofillers. The most severe outcome of the agglomeration is deterioration in mechanical and thermal properties of PAu

and PAg nanocomposites. Since the particles stay in clusters; they cannot show enormous nanosize properties such as large surface area to volume ratio anymore (See Chapter 3). Another important point concluded from isothermal DMA experiments is; there is no significant difference found in mechanical properties of PAu/Ag10 and PAu/Ag30 samples although higher improvement is expected for smaller NPs since they have larger surface area. Apparently, this much of increase in surface area is not sufficient to make remarkable increase in young's modulus or tensile strength.

4.4.2. Glass Transition Temperature Measurements for PAu10 and PAg10 Nanocomposites

Nanocomposites were initially subjected to preheating/precooling process in order to neglect thermal history and then heated from -100 °C to 100 °C to see the transition from glassy to rubbery state. Since recorded glass transition temperature of PEO is -52 °C [100], liquid nitrogen was used to set the initial temperature of samples under 0 °C. While storage modulus is ability to store energy of a polymer representing the elastic response, loss modulus characterizes the viscous behavior of a material. When the polymer is heated above its T_g , the value of storage modulus will suddenly drop and loss modulus will reach its peak value since the polymer chains become rubbery (See Figure 4.11). Glass transition temperatures for various nanocomposites were read from the peak of the loss modulus vs. temperature curves. In Figure 4.11, data for temperature scan experiment of neat PEO is given. The average of glass transition data collected for several trials is found as -44.9 ± 2.6 °C for neat PEO, where the theoretical T_g was recorded to vary between -53 °C to -45 °C [37, 100].

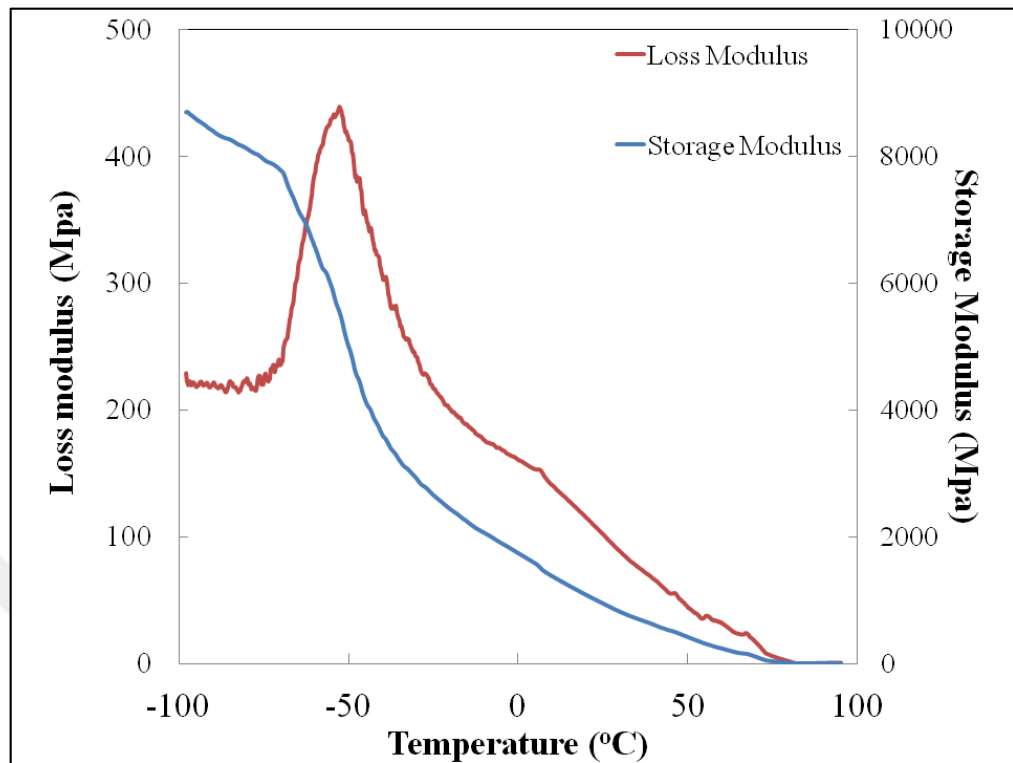


Figure 4.11. Temperature scan experiment for neat PEO

The data obtained from the peak of loss factor plots revealed that, addition of Au10 NPs with 0.3 per cent (by wt) concentration made a decrease of 4.5 °C in T_g compared to neat PEO, whereas Ag10 NPs contributed to an increase in T_g of almost 10 °C with 1 per cent (by wt) of Ag10 NP addition. This value reaches its maximum (-35.1 ± 2.3 °C) with the addition of Ag10 NPs at 1 per cent (by wt), however decreased to -47.6 ± 2.0 °C for Au10 NPs of the same concentration.

It has been pointed out that changes in glass transition temperature due to nanofiller addition can be explained with two possible reasons [101]. The increase in T_g may be attributed to strong interactions or hydrogen bonding between the nanofillers and polymer matrices. These attractions between molecules limit the mobility of polymer chains and make dynamics slower, resulting in higher T_g . Contrarily, in the case of weak interactions between molecules, free volume around relaxing chains of polymers increase, leading flexible movements due to loose packing also known as plasticizing effect. Besides the fact that the different amount of surfactant molecules surrounded around Au and Ag NPs as shown with TGA, it is always possible for surfactants to stay in different configurations

while they are dispersed in the polymer matrix. To sum up, T_g values were found to change between an temperature interval of -35 and -49 °C for various NP concentrations (See Table 4.2.) and it is hard to express a consistent relationship between them. Some T_g values were found to decrease with addition of NPs and exactly the opposite was observed for others. Published results can be attributed to different dislocations and consequent movements of polymer chains in each sample.

Table 4.2. Glass transition temperature and loss factor data for nanocomposites

Sample Name	T_g (°C)	Loss factor (tan δ)
Neat PEO	-44.9 ± 2.6	0.082 ± 0.012
PAu10-0.01	-44.8 ± 2.1	0.065 ± 0.005
PAu10-0.03	-46.1 ± 2.4	0.061 ± 0.004
PAu10-0.1	-47.5 ± 2.0	0.063 ± 0.003
PAu10-0.3	-49.4 ± 0.1	0.059 ± 0.003
PAu10-0.5	-48.5 ± 0.6	0.059 ± 0.002
PAu10-1	-47.6 ± 2.0	0.061 ± 0.001
PAg10-0.01	-42.0 ± 4.3	0.059 ± 0.002
PAg10-0.03	-44.4 ± 3.2	0.057 ± 0.003
PAg10-0.1	-42.2 ± 3.6	0.065 ± 0.006
PAg10-0.3	-40.3 ± 2.0	0.060 ± 0.002
PAg10-0.5	-40.4 ± 4.3	0.073 ± 0.010
PAg10-1	-35.1 ± 2.3	0.074 ± 0.012

The loss factor (tan δ) calculated as the ratio of loss modulus to storage modulus is an indicator of energy lost. The increase in loss factor is an indicator for low elasticity. Temperature scan experiments for neat PEO gave the highest loss factor with 0.082 ± 0.012 among the others, revealing that it has the poorest elasticity. The addition of Au10 and Ag10 NPs led to an increase in tan δ and makes films gain high elasticity.

4.4.3. Crystallinity Measurements for PAu10 and PAg10 Nanocomposites

It is well known that a semi-crystalline polymer crystallizes when it is cooled from melt and structural properties of the polymer strongly depend on its crystallinity. Thus, DSC crystallization experiments are of great interest. The crystallinity of polymers is effected by sample preparation as well as the chain configuration, stereoisomerism and branching of the polymer. Different cooling rates would result in different crystallinities while preparing the sample. Our goal, specifically, is to observe the effect of nanoparticles on crystallinity, if any, with keeping the cooling and heating rates constant. That is why we conducted thermal pretreating procedure before any further DSC experiments.

Each DSC experiment was carried out by heating the sample from 25 °C to 100 °C with keeping the heating rate constant at 10 °C /min. Temperature and enthalpy of melting were found from the sharp endothermic peak appeared after heating and their averages are presented. T_m was obtained at 67.9 ± 0.4 °C for neat PEO and while area under the heating curve was calculated as 142.1 ± 15.7 J/g. Per cent crystallinity (X_c) was calculated using eqn. 3.11;

$$X_c = \frac{142.1 \text{ J/g}}{197 \text{ J/g}} \times 100 = 72.1 \% \quad (4.12)$$

Therefore; X_c for neat PEO is found as 72.1 per cent, where ΔH_m^0 , theoretical heat of melting of 100 per cent crystalline PEO, was recorded as 197 J/g by Wunderlich et al. as it was mentioned before [98]. The films doped with Au10 and Ag10 at 0.5 and 2 per cent (by wt) concentrations, representing low and high nanoparticle contents respectively, were tested with applying the exactly same procedure and the results are tabulated.

Table 4.3. Melting temperature, enthalpy and per cent crystallinity data for nanocomposites

Sample Name	T_m (°C)	ΔH_m (J/g)	X_c (per cent)
Neat PEO	67.9 ± 0.4	142.1 ± 15.7	72.1
PAu10-0.5	68.3 ± 0.5	137.3 ± 15.1	69.7
PAu10-2	67.8 ± 0.5	140.4 ± 16.1	71.2
PAg10-0.5	67.2 ± 0.3	150.1 ± 23.3	76.2
PAg10-2	66.2 ± 1.1	142.4 ± 15.6	72.3

The abovementioned results show some fluctuations in their crystallinity values; however, these are more likely to be within experimental error than a significant effect. Although it was shown that the interaction between nanoparticles and polymer changes with the addition of nanoparticles, this does not appear to be sufficient to change the conformations of long chains of polymer molecules and the number of ordered segments, resulting in a change in the crystallinity of the polymer.

In literature survey, T_g and T_m of polymeric materials are defined as lower and upper limits for possible applications. Referring to our results it can be said that; the final products of PEO would be more durable and strong between temperature ranges of -44.9 °C (T_g) to 67.9 °C (T_m); which makes a temperature interval of 112.8 °C. Addition of Au10 NPs to PEO at almost 0.5 per cent (by wt) concentration increased this range to 116.8 °C. However, the difference between T_g and T_m is found to elevate to 107.6 °C for PAg10-0.5 nanocomposites. To be more specific, the addition of Au10 and Ag10 NPs do not seem to change T_m , T_g or crystallinity of PEO directly, but the difference between glass transition and melting; the lower and upper limits for applications; expands for PAu10 nanocomposites.

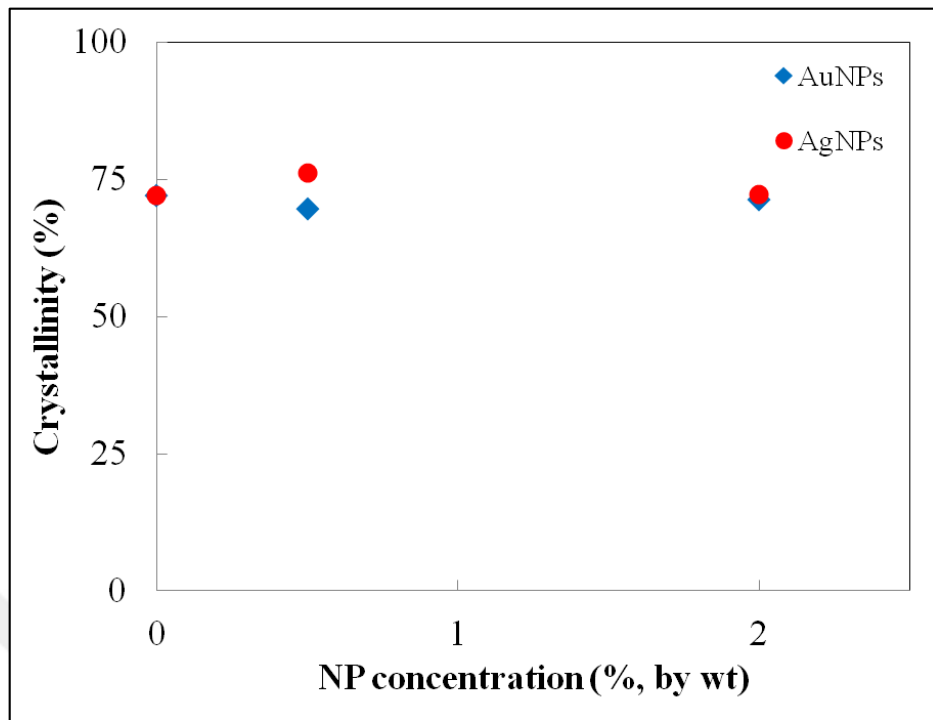


Figure 4.12. Per cent crystallinity of nanocomposites as a function of NP concentration

4.5. CONCLUSION

Thermal and mechanical properties of nanocomposites have become a great interest because improved properties of polymers with addition of nanofillers were found in most of the studies. In order to study thermomechanical properties of PEO doped with Au and Ag nanoparticles, dynamic mechanical analysis and differential scanning calorimetric techniques were conducted. The parameters related to thermomechanical properties of polymers were discussed such as young's, loss and storage modulus; loss factor; compliance; tensile strength; glass transition and melting temperature; crystallinity, etc.

According to stress vs. strain curves, the strength and stiffness of the nanocomposites were found to increase with addition of nanoparticles by regardless of NP type and size. The maximum increase in young's modulus was recorded as 59 per cent for PAu10-0.3 and 54 per cent for PAg30-0.1 respectively. In tensile strength data, similar to those in young's modulus, 15.9 per cent and 18 per cent of increase is recorded in TS with addition of Au and Ag NPs respectively. Also, results indicated that changing the NP size from 10 to 30 nm does not affect mechanical properties. However, the increase in mechanical properties

reached plateau after certain concentration for all nanocomposites. The threshold concentration is recorded at around 0.006 per cent (by vol.). Experimental results suggest that mechanical properties of PEO are strongly correlated to polymer phase separation (See Figure 3.5), which depends on the nature of the interface between the polymer and the nanoparticles for higher concentrations.

The elasticity of PEO was also found to increase for high concentrations of NPs and in order to express relationship between NP concentration and thermal properties, melting enthalpy and loss modulus data was evaluated. Although, inconsistency in T_g and T_m values was observed for PEO nanocomposites, the difference between upper and lower temperature limits was found to increase from 112.8 °C to 116.8 °C when Au10 NPs are dispersed in PEO matrix by 0.05 per cent (by vol) of concentration. This increase enables PEO to be used in further applications in wider temperature range. On the other hand, crystallinity of the samples remained almost same; recorded between 69 to 76 per cent. To sum up, PAu and PAg nanocomposites displayed better mechanical properties up to certain concentration, however significant changes could not be observed for thermal experiments.

5. THE EFFECT OF FUNCTIONALIZED SILVER NANOPARTICLES OVER THE THERMAL CONDUCTIVITY OF BASE FLUIDS

5. 1. INTRODUCTION

Convective heat transfer can be enhanced by altering flow type, boundary conditions and corresponding thermal conductivity of the heat transfer fluid used. Common heat transfer fluids have low thermal conductivities at room temperature [102] leading to inefficiency in heat transfer applications. Relative thermal conductivities of fluids containing solid particles have been investigated both experimentally and theoretically since the theory of Maxwell [103] had been reported. However, the particles used in these studies cover a size range in micrometers which cause clogging and consequent settling of the particles as a result of insufficient stability. Modern technology provides scientists to work with nano-sized particles that expected to have superior properties over micro-sized particles and traditional base fluids. The most important properties that differentiate nanoparticles (NPs) from micro-sized particles are their large surface area to volume ratio where the heat transfer will occur [104] and smaller size which will prevent clogging.

Previously, the use of nanofluids for heat transfer applications was demonstrated by suspending metallic NPs in heat transfer fluids by Choi et al. [102]. They did an experimental work by suspending carbon nanotubes in synthetic oil at 1 per cent (v/v) ratio based on the theoretical studies of Batchelor & O'Brien [105] and Hamilton & Crosser [106] and 150 per cent enhancement over the corresponding thermal conductivity of the base fluid was reported. Several studies cover the factors affecting heat transfer in nanofluids such as; NP type and size [107], base fluid, the role of surfactant [108] and ambient conditions like pH and temperature [109].

Table 5.1. Theoretical thermal conductivity values for some metals & metal oxides and common heat transfer fluids at 25 °C

	k (W/m.K)		k (W/m.K)
Al	237 [102]	Water	0.613 [102]
Al₂O₃	40 [104], 36 [110]	Ethylene glycol	0.253 [102]
Cu	401[102], 386 [104]	Hexane	0.117 [102]
CuO	20, 33 [110]	Engine oil	0.145 [102]
Ti	21	Ag	429 [102]
TiO₂	4.8-11.8 [111], 8.4 [110]	Au	315 [112]

Metal oxides such as aluminum oxide (Al₂O₃), titanium dioxide (TiO₂) and copper oxide (CuO) constitute the major research area on effective thermal conductivity. Bulk metals, on the other hand, have relatively higher thermal conductivity than their oxides and copper (Cu), iron (Fe), silver (Ag), and gold (Au) have been the most useful metallic NPs.

In this chapter, thermal conductivities of Ag nanoparticles in several solvents were investigated using transient hot wire technique (THW). Nanofluids were prepared via two step method; which includes addition of pre-synthesized nanoparticles in heat transfer solvents. The addition of nanoparticles yielded an increase in thermal conductivities of oil based solvent (hexane) and ethylene glycol, whereas deterioration in effective thermal conductivity was recorded for water.

5.2. NANOFUIDS

5.2.1. Preparation of Nanofluids

Synthesis of nanofluids is the essential step for the heat transfer applications. Nanofluids are not simply solid-liquid solutions; they require an even suspension, perfect stability, acceptable agglomeration and no chemical interaction between particles. To ensure that, two types of preparation methods were proposed; (1) Two-step and (2) One-step preparation methods.

5.2.1.1. Two-Step Method

The method basically consists of synthesizing nanomaterials in dry form, then mixing them with base fluids. Nanoparticles, nanofibers, nanotubes, or other nanomaterials used in this method are first produced as dry powders by several proposed chemical or physical methods. The second step is then performed with dispersing formed nanosized powder into a base fluid. Combination of two components can be accomplished either with the help of intensive magnetic force agitation, ultrasonic agitation, high-shear mixing, homogenizing, or ball milling [110].

In literature, thermal conductivity of nanofluids prepared with two-step method is frequently encountered. Sahu et al. found maximum 6 per cent of enhancement in thermal conductivity of DI water with addition of Cu NPs but suggested an improvement of 15 per cent if the nanoparticles are stabilized with PEG [113]. In another study, addition of CuO NPs led to an increase of only 3 per cent on the thermal conductivity of water [114]. Wang et al. tested fluids containing two types of NPs, Al_2O_3 and CuO, dispersed in water, vacuum pump fluid, engine oil, and ethylene glycol [115]. The addition of CuO to water (\approx 5 per cent volume fraction) and ethylene glycol (\approx 6 per cent volume fraction) resulted an increase of almost 19 and 24 per cent respectively. Similarly, relative thermal conductivity was calculated as 1.15 and 1.25 when Al_2O_3 NPs were added to water and ethylene glycol at almost 5 per cent vol. fractions. Contrary to the work of Sahu et al., they reported that the enhancement in thermal conductivity in presence of Al_2O_3 is lower when polymer coating is added as a stabilizing agent. Another work also supports the theory of Wang stating that an increase in Al_2O_3 NP concentration increases thermal conductivity, and an increase in dispersant concentration reduces thermal conductivity for all Al_2O_3 NP concentrations [116].

An intensive study on thermal conductivity of citrate coated Au NPs (10 - 20 nm) in water and thiolate coated Au NPs (3 - 4 nm) in toluene was established by Patel et al. [108]. The major conclusions for Au NP nanofluids can be listed as; (1) A higher increase from thermal conductivity of neat toluene was seen as 7 per cent in nanofluid with thiolate coated Au NPs (at per cent 0.011, by vol.) at 30 °C and 8.8 per cent at 60 °C; (2) Similarly, a higher increase from thermal conductivity of water and citrate (blank) solution was seen

as 4.6 per cent in nanofluid with citrate coated Au NPs (at 0.00026 per cent, by vol.) at 30 °C and 8.3 per cent at 60 °C. (3) At lower concentrations, relative thermal conductivities were reduced for both cases. In the same study, thermal conductivity of citrate coated Ag NPs (60 – 80 nm) in water (at 0.001 per cent, by vol.) was also measured. It was seen that the conductivity enhances from about 3.2 per cent at 30 °C to 4.5 per cent at 60 °C with respect to blank solution. Although Ag has higher conductivity and an order of magnitude higher concentration than Au, these particles showed less enhancement of the conductivity which is attributed to higher particles size and lower aspect ratio.

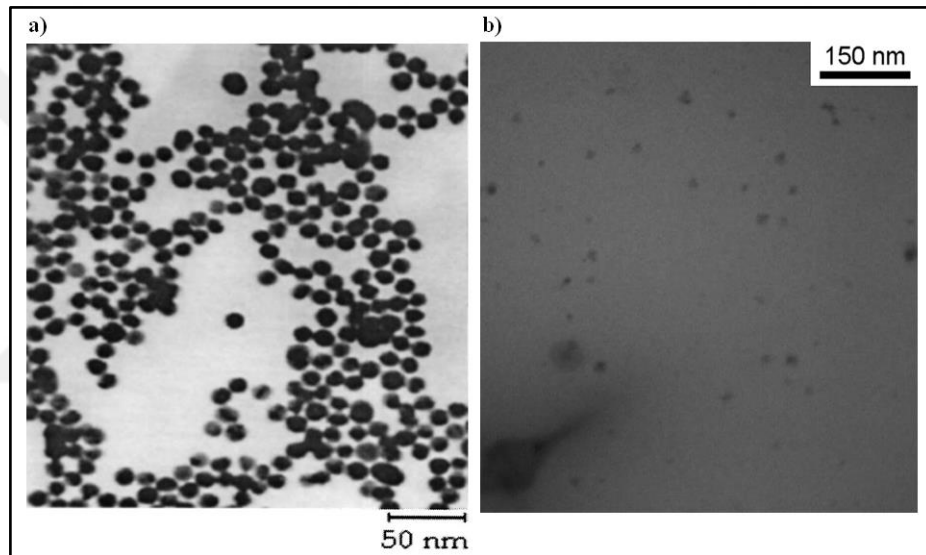


Figure 5.1. TEM images of (a) Citrate stabilized Au NPs (two-step method) [108];
(b) PVP stabilized Ag NPs (one-step method) [117]

Shalkevich et al. [112] conducted a series of experiments with Au NPs coated with citrate in water at concentrations of 0.00025 per cent and 0.00055 per cent (by vol.). Surprisingly, the maximum increase at thermal conductivity of nanofluids was recorded only as 1.5 per cent, in fact a decrease of 0.3 per cent was observed at AuNP in water (0.00025 per cent by vol) at 40 °C.

5.2.1.2. One-Step Method

Although two-step method is the most widely used and economic method to produce nanofluids in large scale [118], particles tend to agglomerate due to high surface area and surface activity. Since it is quite difficult to obtain stable nanofluids by two-step method, several advanced techniques are developed to produce nanofluids, including one-step method which involves simultaneous preparation and direct dispersion of nanoparticles in the base fluid [11]. Cho et al. used one-step method to prepare Ag nanofluid using silver nitrate as precursor, ethylene glycol as reducing agent and solvent, poly (acryl-amide-co-acrylic acid) as a dispersing agent [119]. They reported that thermal conductivity of ethylene glycol increases by 10, 16 and 18 per cent for nanofluids containing 1000, 5000 and 10000 ppm of Ag NPs.

An another attempt has been made to synthesize Ag nanofluid with one-step method using silver nitrate as metal source, sodium borohydride and hydrazine as reducing agents in work of Salehi et al. [117]. The medium base was water and poly (vinyl pyrrolidone) (PVP) was used as surfactant. They have found an increase in thermal conductivity of water up to 18 per cent for sample containing 1000 ppm of Ag NPs and 10 g of PVP as dispersing agent. However, effective thermal conductivity was reduced from 1.175 to 1.135 and 1.105 when added PVP was increased to 12.5 g and 15 g respectively.

5.2.2. Heat Transfer in Nanofluids

It has been stated that heat transfer in nanofluids are governed by four modes of energy transport [120] (See Figure 5.2). First mode is originated from the thermal conductivity of a carrier fluid, in other words; heat transfer due to collision of base fluid's (BF) molecules.

The net energy flux due to collision of molecules over the path length of l is given as J_u ;

$$J_u = -\frac{1}{3} I_{BF} \hat{C}_{V,BF} \bar{C}_{BF} (1-f) \frac{dT}{dz} = -k_{BF} \frac{dT}{dz} (1-f) \quad (5.1)$$

where \hat{C}_V , \bar{C} and T are the heat capacity per unit volume, mean speed and temperature of the base fluid respectively. k_{BF} is given for the thermal conductivity of base fluid and f is for the volume fraction of the particles dispersed.

Second and third modes denote thermal motions of the nanoparticles; can be investigated under two concepts; thermal diffusion and Brownian motion of the nanoparticles. Thermal diffusion in nanoparticles in fluids is given by;

$$J_u = -\frac{1}{3} l_{NP} \hat{C}_{V, NP} \bar{v} f \frac{dT}{dz} = -k_{NP} \frac{dT}{dz} (f) \quad (5.2)$$

where k_{NP} and \bar{v} are thermal conductivity of the nanoparticles and the mean speed of electrons or photons respectively, the other abbreviations stand for the same parameters as in first case [120].

Brownian motion enables the direct energy transfer between solid molecules, by which collision of the particles are expected to have higher role in enhancement in thermal conductivity than thermal diffusion. However, Keblinski et al. [121] have shown that thermal diffusion is faster than Brownian motion and is characterized through the particle diffusion constant, D , given by Stokes-Einstein formula;

$$D = \frac{k_B T}{3\pi\eta d} \quad (5.3)$$

where k_B is the Boltzmann constant, η is the fluid viscosity and d is the particle diameter [121].

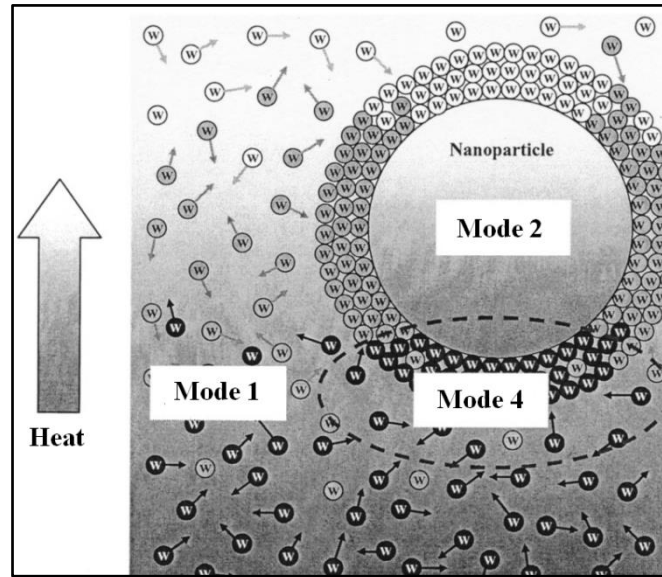


Figure 5.2. Modes of energy transfer in nanofluid systems [120]. (The first mode is collision between base fluid molecules; the second mode is the thermal diffusion of NPs suspended in fluids; the third mode is collision between NPs (not shown); and the fourth mode is thermal interactions of NPs with base fluid molecules.)

The last mode is proposed for the thermal interactions between nanoparticles and base fluid. Jang et al. [120] postulated that Brownian motions of the nanoparticles produces convection-like effects at nanoscale and defined the last mode as;

$$J_u = h (T_{NP} - T_{BF}) f = h \delta_T f \frac{T_{NP} - T_{BF}}{\delta_T} \approx -h \delta_T f \frac{dT}{dz} \quad (5.4)$$

where h and δ_T are the heat transfer coefficient between BF and NPs and the thickness of the thermal boundary layer, respectively.

5.2.3. Theoretical Thermal Conductivity Models for Nanofluids

Several mathematical models were developed to estimate the thermal conductivity of nanofluids. In these models enhancement in thermal conductivity is explained via effective medium theory (EMT). In earlier models, only three parameters were considered in EMT assuming the solid particles to be inert in fluids. These models included thermal conductivity of the bulk fluid, nanoparticles and volume fraction of NPs in base fluid [103,106]. The Maxwell model is able to predict effective thermal conductivity (k_{eff}) of nanofluids with spherical NPs at low fractions.

$$k_{eff} = \frac{k_{NP} + 2k_{BF} + 2\phi(k_{NP} - k_{BF})}{k_{NP} + 2k_{BF} - \phi(k_{NP} - k_{BF})} \quad (5.5)$$

where k_{eff} is the effective thermal conductivity of the nanofluid and ϕ is the volume fraction of the particles [103].

There is a slight difference between the Hamilton and Crosser (H-C) model and the Maxwell model which is that the H-C model takes the effect of the shape of the solid particles into consideration with defining η as an empirical shape factor.

$$\eta = \frac{3}{\Psi} \quad (5.6)$$

where Ψ is the sphericity which is the ratio of the surface area of a sphere with a volume equal to that of the particle to the surface area of the particle. Therefore, $n = 3$ for a sphere, and in that case the Hamilton and Crosser model (eqn. 5.7) becomes identical to the Maxwell model as expressed in eqn. 4.5 [106].

$$k_{eff} = \frac{k_{NP} + (n-1)k_{BF} + (n-1)\phi(k_{NP} - k_{BF})}{k_{NP} + (n-1)k_{BF} - \phi(k_{NP} - k_{BF})} \quad (5.7)$$

In addition, some valuable models were presented recently. These models were originated from the theory of Maxwell and most of them (Yu-Choi model [122], Leong et al.'s model [123], Xie et al.'s model [124] and Sohrabi et al.'s model [125]) considered the effect of the nanolayer as well. These models will not be discussed in this work, since it is beyond the aim. The major purpose of this current study involves the experimental study on the effect of functionalized Ag NPs on the thermal conductivities of ethylene glycol, distilled water and hexane base fluids.

5.3. EXPERIMENTAL

Nanofluids were prepared via two-step method; with basically adding synthesized nanoparticles in base solvents. Oleic acid & oleylamine coated Ag NPs (Ag10/o) and gum arabic coated Ag NPs (Ag10/w), both explained in Chapter 2, were used to prepare nanofluids. The nanoparticles were then dissolved in hexane (AnalaR, NORMAPUR®), distilled water and ethylene glycol (BDH, VWR Analytical, < 99). Nanoparticle concentrations in solvents were altered from 0.037 to 0.99; 0.25 to 1 and 1 to 2 per cent (by weight) for water, ethylene glycol and hexane respectively. Mass fractions of the solutions were converted to volume fractions with taking the densities constant as 10.5 g/ml for Ag NPs, 0.655 g/ml for hexane, 1.115 g/ml for ethylene glycol and 0.998 g/ml for distilled water. The nanoparticle concentration and solvent combinations can be seen in Table 5.2.

Transient hot wire technique (THW) was used to measure thermal conductivity of samples. Flucon GmbH Lambda thermal conductivity meter equipped with PSL Systemtechnik LabTemp 30190 temperature controller, which is able to measure thermal conductivity over a temperature range of -30 °C to 190 °C, was used. The temperature was kept constant with use of tap water as cooling medium. Thermal conductivity values were directly read from samples and recorded in mW/m.K for each 10 °C intervals with an accuracy of 0.1 °C. Only small amounts of sample (ca. 50 ml) are sufficient to execute reliable measurements. Each measurement was repeated for a minimum of three times.

Table 5.2. Prepared nanofluids for thermal conductivity experiments

Nanofluid sample	Solvent type	NP type	NP Concentration (per cent)	
			Weight (by wt)	Volume (by vol)
Hex/Ag-1	Hexane	Ag10/o	1	0.063
Hex/Ag10-2			2	0.127
DW/Ag10-0.037	Distilled Water	Ag10/w	0.037	0.0035
DW/Ag10-0.11			0.11	0.011
DW/Ag10-0.33			0.33	0.033
DW/Ag10-0.66			0.66	0.066
DW/Ag10-0.99			0.99	0.099
EG/Ag10-0.25	Ethylene glycol	Ag10/w	0.25	0.027
EG/Ag10-0.50			0.50	0.054
EG/Ag10-0.75			0.75	0.079
EG/Ag10-1			1	0.107

Viscosity measurements were performed using a Brookfield DV-III Ultra Programmable Rheometer, which measures fluid parameters of shear stress and viscosity at given shear rates. The measurements were repeated for 3 times at room temperature and rheometer was auto zeroed prior to each measurement.

5.4. RESULTS AND DISCUSSION

Previously synthesized Ag NPs having an average diameter of 10 nm were used to investigate the effect of nanoparticles on thermal conductivity of base fluids. Three types of solvents were selected as base fluids; hexane, distilled water and ethylene glycol. Thermal conductivity data was recorded every 10 °C and repeated for several times. The agglomerations of nanoparticles were observed for the nanofluids with higher

concentrations, thus the nanofluids with higher Ag concentrations than presented could not be studied.

5.4.1. Enhanced Effective Thermal Conductivity for Hex/Ag and EG/Ag Nanofluids

Figure 5.3.a shows the increase in thermal conductivity of hexane with addition of Ag10/o NPs at a ratio of 1 and 2 per cent (by wt). The thermal conductivity of pure hexane was measured as 119.1 ± 0.14 mW/m.K at 20 °C and the decay to 112.2 ± 0.21 mW/m.K was observed at 40 °C, while it was predicted at around 111 mW/m.K [126] and 117 mW/m.K [102] at room temperature. With a similar manner, Altan et al. studied the effect of magnetite nanoparticles on thermal conductivity of various alkane based fluids and found that the thermal conductivity of hexane decreases rapidly with increasing temperature [126]. In this present work, consistent results were found with literature; the thermal conductivity of the base fluid tends to decrease with increasing temperature, if the solvent is oil based. Consequently, the same decreasing trend as in thermal conductivity of neat hexane was observed for Ag/Hexane nanofluids with increase of temperature for all Ag10/o concentrations.

Figure 5.3.b shows the temperature dependency of EG based nanofluids. Whereas pure ethylene glycol's thermal conductivity was measured at 293.4 ± 0.13 mW/m.K at 20 °C, an enhancement to 298.8 ± 0.32 mW/m.K was observed for the same solvent at 50 °C. This time thermal conductivity of the base fluid increase with increasing temperature since the fluid is polar. The trend for temperature dependency for EG/Ag10-0.25, EG/Ag10-0.5, EG/Ag10-0.75 and EG/Ag10-1 is also same with pure ethylene glycol which is also presented in Figure 5.3.b. The effect of Ag NPs on thermal conductivity of EG was previously studied [119, 127], yet the temperature dependency was not investigated. Here we present both.

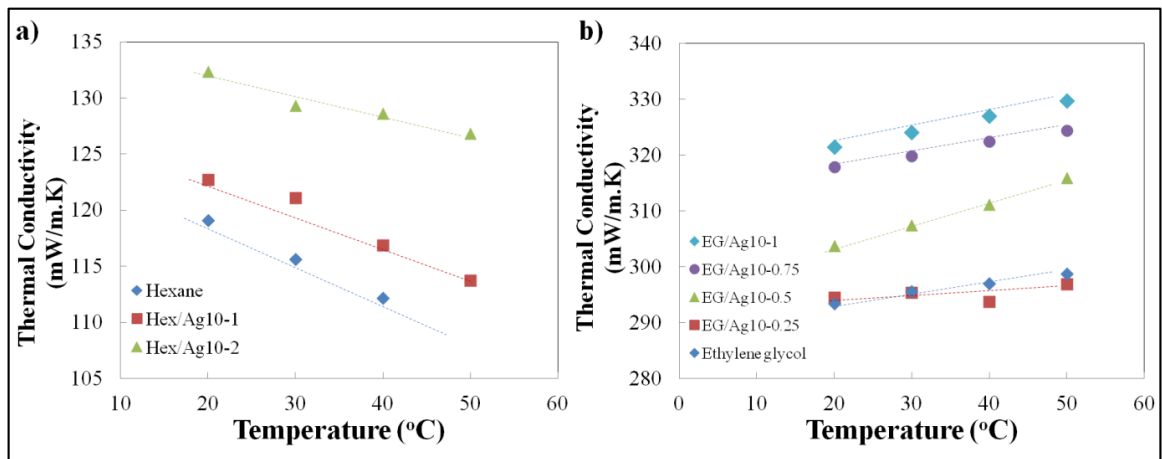


Figure 5.3. Thermal conductivity of (a) Hex/Ag10 and (b) EG/Ag10 nanofluids at different concentrations as a function of temperature

Relative thermal conductivity is defined with the ratio of thermal conductivity of nanofluid to pure solvent (k_{eff}/k_{BF}). Comparing to thermal conductivity of carrier fluid (hexane and EG) themselves, an improvement has been found with addition of Ag NPs. For the thermal conductivity of EG/Ag-1 (0.107 per cent, by vol) nanofluid, an increase of 9.7 per cent was recorded with respect to neat EG at 20 °C. At the same temperature, the increase was recorded as 3.1 per cent for Hex/Ag-1 (0.063 per cent, by vol) and 11.3 per cent for Hex/Ag-2 (0.127 per cent, by vol). It can be roughly said that, addition of Ag NPs at identical volume concentrations to EG and hexane yields similar results (See Figure 5.4).

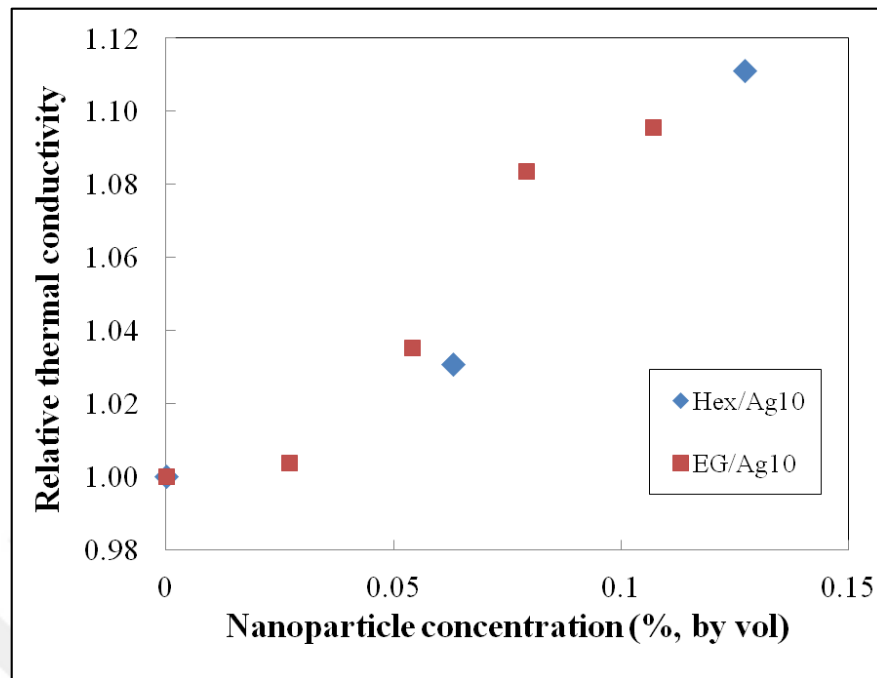


Figure 5.4. Relative thermal conductivities of Ag10/o NPs in hexane and Ag10/w NPs in ethylene glycol at 20 °C.

Relative thermal conductivity of hexane and ethylene glycol is found to be improved with increasing Ag NP concentration. The greater volume that the spherical particles occupy, it is more likely to molecules collide and transfer the heat. But a linear relationship between relative thermal conductivity and NP concentration cannot be proposed. For instance, relative thermal conductivity of EG initially increases slowly. But after Ag NP concentration of 0.054 per cent (by vol), a rapid increase in thermal conductivity is observed. But then, the rate of increase declines for higher concentrations. Similar S shape is also seen in hexane case, but it should be supported with further data. The enhancement in relative thermal conductivity with addition of Ag NPs to hexane and ethylene glycol is mainly due to relatively high thermal conductivity of Ag NPs with respect to base fluids. (k_{hex} and k_{EG} is recorded as 117 and 253 mW/m.K, whereas it is 429000 mW/m.K for Ag NPs [102]. The interactions between carrier fluid molecules and solid particles, thermal diffusion and Brownian motion of NPs are responsible for enhanced heat transfer. On the other hand, deceleration in rate of increase in thermal conductivity is seen for higher concentrations. It is attributed to agglomerations of particles. As the nanoparticles

aggregate, some of them will settle; consequently the particle concentration adjacent to hot wire (where the measurements are taken) decreases.

5.4.2. Deterioration in Relative Thermal Conductivity of DW/Ag Nanofluids

Although, there are several studies in the literature that cover thermal conductivity of aqueous nanofluids with metal oxides like copper oxide, aluminum oxide and iron oxide (magnetite), it is rare to find an article on the effect of metals, either itself or nanoparticle of bulk metals, on thermal conductivity of water. Previous works involving enhanced thermal conductivity of water usually comprises addition of copper oxide [114, 128, 129] aluminum oxide [107, 115, 129, 130] and iron oxide [131, 132] to water and all agreed on enhancement in thermal conductivity upon addition of NPs.

In recent researches those investigate thermal conductivity of Au and Ag dispersed aqueous nanofluids; nanoparticles were capped with several surfactants; i.e., citrate [108, 112] poly (acryl-amide-*co*-acrylic acid) [119], poly (vinylpyrrolidone) (PVP) [117]. Most of them found a considerable increase in thermal conductivity of nanofluids [108, 119], except no considerable affect was observed for TC of water when citrate coated AuNPs at a concentration of 0.00025 per cent (by vol) were added at 40 °C [112].

Deterioration in thermal conductivity was only found and published in the work of Altan et al., in which effective thermal conductivity was measured for aqueous magnetic fluids [133]. In this work of ours, effect of gum arabic coated Ag NPs on the thermal conductivity of water is investigated.

Figure 5.5 demonstrates the change in thermal conductivity of water with temperature for nanofluids having different Ag10/w concentrations. Thermal conductivity of water was recorded as 595.5 ± 1.50 mW/m.K at 20 °C and found to elevate to 627.3 ± 2.46 mW/m.K at 60 °C. The increasing behavior of water with temperature is expected, just like other polar solvent; ethylene glycol. Water based nanofluids having Ag10/w NPs up to a concentration of 0.33 per cent (by wt) displayed a similar temperature dependency trend with pure water. An increase in thermal conductivity with elevating temperature is

observed for just three nanofluids with low NP concentrations (DW/Ag-0.037, DW/Ag-0.11 and DW/Ag-0.33).

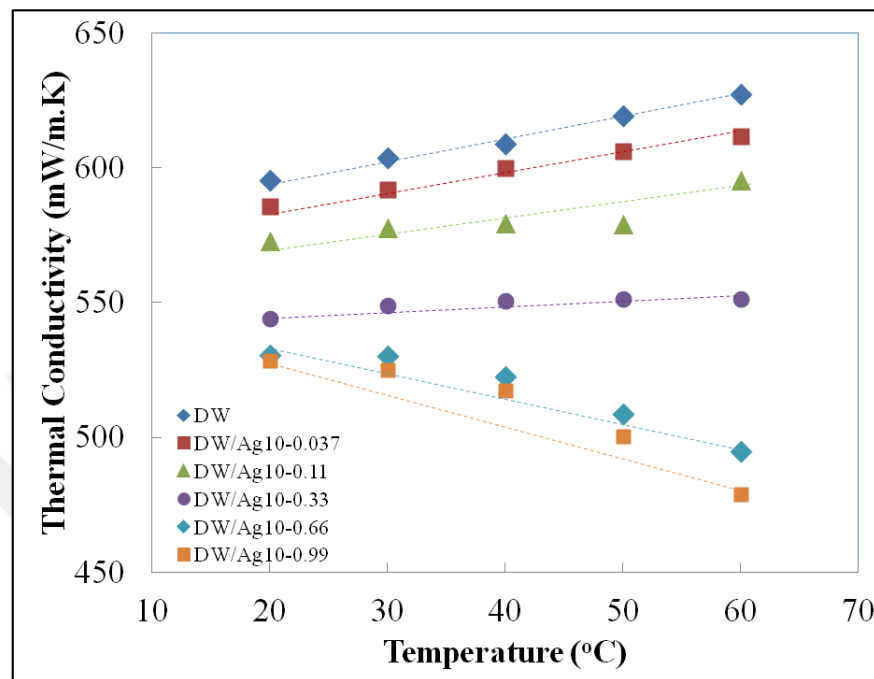


Figure 5.5. Thermal conductivity of Ag10/w NPs dispersed in water at different concentrations as a function of temperature.

However, for the nanofluids having Ag10/w concentration of 0.66 and 0.99 per cent (by wt.), a decrease in thermal conductivity was observed with increasing temperature (See Figure 5.5.). The temperature dependency of water based nanofluids will be discussed in section 5.4.3.

Another abnormal trend in Ag10/w dispersed in water nanofluids was detected for relative thermal conductivities. Despite the fact that the thermal conductivity of silver ($k_{Ag} = 429$ W/m.K) is almost 700 times of water ($k_{water} = 0.613$ W/m.K) [102], the addition of Ag10/w NPs to water reduces its relative thermal conductivity.

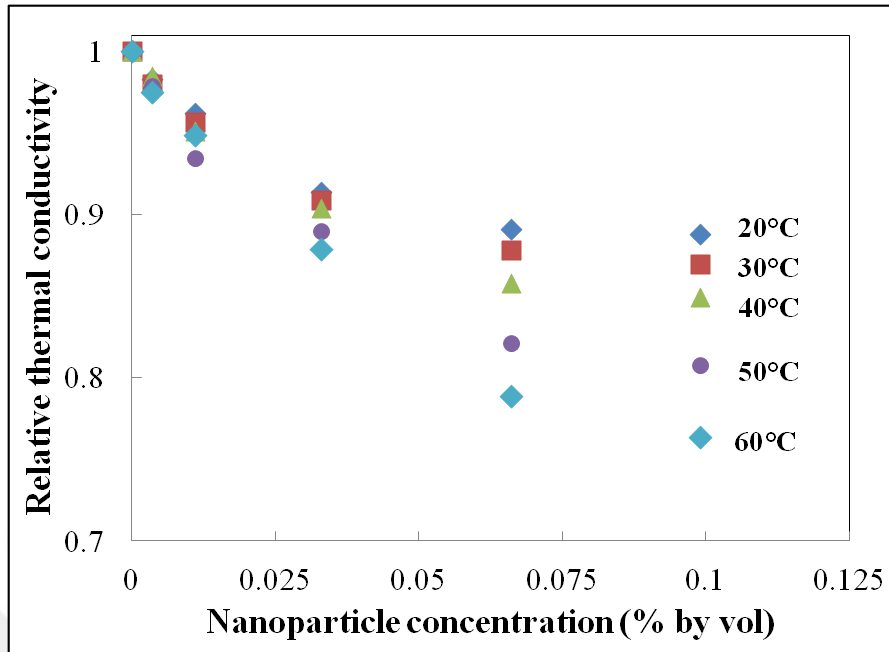


Figure 5.6. Relative thermal conductivity of Ag10/w NPs in water

This fall can be seen in Figure 5.6. For low Ag NP concentrations, the decrease in TC is observed for each temperature. However, the deterioration in thermal conductivity reaches a plateau after a certain concentration, i.e. 0.06 per cent (by vol). Also, with the increase of temperature, the rate of fall in TC is dramatically increased. The significant fall in thermal conductivity (at 20 °C) was recorded as 11.2 per cent for nanofluid sample which has Ag10/w concentration of 0.099 per cent (by vol). In other words, the addition of Ag10/w nanoparticles at 0.099 per cent (by vol) to water results a decrease in thermal conductivity by 11.2 per cent at 20 °C. Moreover, the fall in TC reaches up to 23.6 per cent at 60 °C for that concentration.

As it was mentioned before, the fall in effective thermal conductivity of magnetic nanofluids was first recorded by Altan et al. [133]. They tried to relate this decline with interfacial thermal resistance (R). In classical EMT models, usually the interfacial thermal resistance is neglected by analyzing particles and fluids separately. The insufficiency of these models is derived from under-predicting presence of interfacial thermal resistance in between the nanoparticles and the surrounding fluid molecules. The interfacial thermal resistance is referred to the equivalent thickness (h) and given as in eqn. 5.8;

$$h = \frac{k_{BF}}{G} \quad (5.8)$$

where, G is the interfacial conductance [134]. Although there are not many studies cover the interfacial conductance of silver water system, it has been widely estimated as 200 MW/m²K for nanoparticle-water systems [135]. Therefore, h is calculated as 3.07 nm for Ag NPs with a diameter of 7.3 ± 2.5 nm. The model developed by Putnam et al. [134] suggests effective thermal conductivity by imposing the interfacial thermal resistance by;

$$\frac{k_{eff}}{k_{BF}} - 1 = 3f \left(\frac{\gamma - 1}{\gamma + 2} \right) \quad (5.9)$$

γ is the ratio of nanoparticle radius to equivalent thickness and found as 1.21 with using the equation below.

$$\gamma = \frac{r_p}{h} \quad (5.10)$$

However, k_{eff} calculated from Putnam's EMT model does not fit the experimental data recorded. For instance, it suggests a k_{eff} value of 639 mW/m.K, while it was experimentally found to be 479.1 mW/m.K for DW/Ag10-0.99 sample at 60 °C. Therefore, the deterioration in effective thermal conductivity cannot be solely explained by the interfacial thermal resistance between particles and the base fluid. Some other parameters should be addressed.

5.4.3. Temperature Dependency Comparison for Hex/Ag, EG/Ag and DW/Ag Nanofluids

In the work of Timofeeva et al., the increase was reported in thermal conductivity of water and ethylene glycol when Al_2O_3 nanoparticles were added to these solvents [130]. They also pointed out that the thermal conductivity of nanofluids increase in the range from 20 °C to 60 °C. However, they concluded that rise with increasing temperature comes from the base fluid rather than from behavior associated with the nanoparticles. Therefore the outcome is; the enhancement in nanofluids relative to base fluids is essentially temperature independent.

With a similar way of thinking, normalized graphs are presented (Figure 5.7) in order to see the effect of temperature on relative thermal conductivity of hexane, ethylene glycol and water. The data for nanofluids are normalized to TC of pure solvents at that temperature in order to neglect the temperature dependency of base fluid and only nanofluids with the highest amount of Ag NP are presented. The charts showed that temperature has no effect on thermal conductivity of nanofluids of hexane and EG regardless of nanoparticle concentration. The trend is also same for the water based nanofluids with low Ag concentration (DW/Ag10-0.037). However, the thermal conductivity of water based nanofluids was found to depend on temperature significantly for higher NP concentrations (DW/Ag10-0.66; data not shown and DW/Ag10-0.99).

The thermal conductivity of metals is known to decrease with increasing temperature [115], therefore for concentrated nanofluids, the NPs are predominantly responsible for the temperature trend, rather than the corresponding base fluid. As a consequence, the temperature trend is found similar to water for nanofluids with low NP concentration (i.e., lower than Ag concentration of 0.33 per cent, by wt).

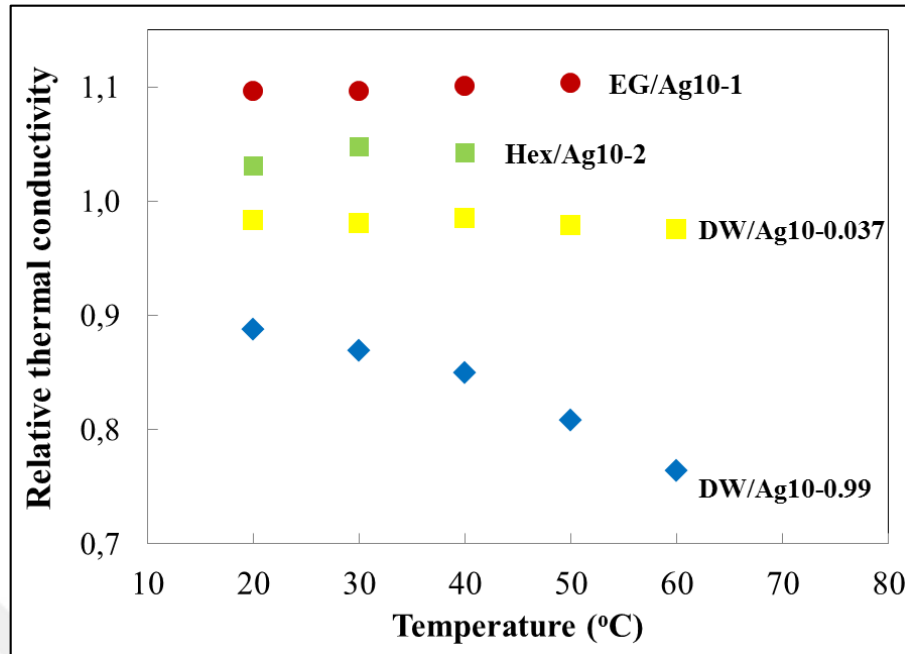


Figure 5.7. Temperature dependency of effective thermal conductivity of nanofluids

Temperature dependent thermal conductivity variation could possibly indicate the critical role of Brownian motion of Ag NPs in water. Increase in thermal conductivity with temperature is expected for polar carrier fluids [133], which is supported with thermal conductivity of water data presented in Figure 5.5. However, reverse trend is observed for Ag/w concentration of 0.66 per cent (by wt) and above. As the Brownian motion is directly proportional to temperature and inversely proportional to viscosity, viscosity of the nanofluid might have significantly affected TC. The decrease in k_{eff} with increasing temperature can be correlated with viscosity of nanofluid if and only if the fluid is enormously viscous such that it hinders the temperature effect.

In order to synthesize Ag NPs in water, certain amount of AgNO_3 and surfactant is put into a reaction (section 2.3.1). After washing of excess reagents, the mass ratio of gum arabic to Ag molecules in reaction yield is predicted to be 42:1; which means the mass of gum arabic layer is considerably high relative to the mass of NPs. That much of gum arabic should be the major responsible in viscosity increase. This claim was supported via viscosity measurements and results indicated that the viscosity of the water is significantly enhanced with addition of gum arabic. The increase in NP concentration, resultantly

increase in mass of gum arabic, might be contributor to the reverse temperature trend in thermal conductivity of highly concentrated aqueous nanofluids.

Table 5.3. Viscosity measurements for gum arabic / water solutions

Gum arabic concentration in water (per cent, by wt)	Viscosity at 25 °C (cP)
0	0.95
3.85	4.10
7.41	8.17

5.5. CONCLUSION

Although the effect of metal oxides on thermal conductivity of base fluids is intensively studied, there is a lack of knowledge on nanoparticles of bulk metals due to the difficulty of stabilization. Here we investigated the thermal conductivity of common heat transfer fluids; water, ethylene glycol and hexane; with addition of relatively low concentration of Ag NPs. Thermal conductivity of nanofluids were measured using hot wire technique. The thermal conductivity of nonpolar organic solvent, hexane, was found to decrease with increasing temperature. At 20 °C, the addition of Ag10/o NPs to hexane made an enhancement of 3.1 and 11.3 per cent at volume concentration of 0.063 and 0.127 per cent respectively. On the other hand, ethylene glycol, a polar solvent, displayed increasing thermal conductivity trend with elevation of temperature. The enhancement in effective thermal conductivity of ethylene glycol was also observed. 9.7 per cent of increase was recorded for EG based nanofluid with Ag10/w concentration of 0.107 per cent (by vol). Temperature dependency of EG and hexane is similar with data found from literature. Also the effective thermal conductivity of nanofluids was found to increase with addition of Ag NPs even at low concentration (maximum 0.127 per cent, by vol). The increase in k_{eff} is attributed to Brownian motion and thermal diffusion of NPs added, also the enhancement in TC can be achieved with increasing NP concentration. However, the rate of increase in TC slows down at higher NP concentration, which is due to the possible NP agglomerations.

On the other hand, the measurements on the thermal conductivity of aqueous Ag nanofluids were contradictory with previous studies [108, 112, 117, 119]. The thermal conductivity of water was found to increase with temperature for nanofluids with low concentrations, however exactly the opposite trend was recorded for aqueous nanofluids with Ag10/w concentration of 0.066 per cent (by vol) and above. Another abnormality was observed with fall in effective thermal conductivity of nanofluids with addition of Ag NPs. The effective thermal conductivity of DW/Ag10-0.99 was found to decrease by 11.2 per cent at 20 °C, in fact the decline reaches up to 23.6 per cent at 60 °C. Addition of Ag NPs to water not only deteriorated k_{eff} , but also influenced the temperature dependency of water unfavorably. These unexpected results were tried to be correlated with presence of interfacial thermal resistance due to organic surfactant layer. EMT model modified by Putnam et al. [134] was used with considering the effect of equivalent thickness of surface layer of NPs. However, the theoretical estimations from Putnam's model did not fit the experimental data. Deterioration in TC of aqueous nanofluids with Ag can only be explained via domination of Brownian motion of particles. The extreme viscosity of the nanofluid due to gum arabic surfactant is suggested to be responsible for influence of interfacial thermal resistance, viscosity of surfactant layer, and/or other parameter combinations can be effective. Although the mechanism of deterioration in thermal conductivity of Ag - water system cannot be fully explained, they can still be proposed as coolers in heat exchangers, however application can be supported with detailed economic analysis.

6. MEASUREMENT OF TEMPERATURE AND CRYSTALLINITY THROUGH CONFORMATIONAL AND STRUCTURAL CHANGES IN PEO VIA RAMAN SPECTROSCOPY

6.1. INTRODUCTION

Measurement of temperature at the nanoscale has become an important goal because of the development of nanoscale devices and our need to control and manipulate structure and properties of materials that form these devices. In many cases, nano - sized tracers are used to measure temperature at the nanoscale, however, the presence of nanoscale tracers could alter the structure and properties of materials at these length scales, therefore, methods those do not require the use of tracers are constantly being sought out.

A semi-crystalline polymer consists of heterogeneous structure including crystalline and amorphous regions. Due to the heterogeneity, properties of the material are highly influenced by degree of crystallinity. PEO is one of the semi-crystalline polymers, which is also a perfect candidate to be studied via Raman spectroscopy due to its C-C backbone. Also the previous Raman studies [37,136, 137] on PEO showed that, the helical structure of this semi-crystalline polymer is strongly influenced by temperature and can be easily detected via conformational changes.

In this part of the study, the use of Raman spectroscopy to measure the temperature of PEO without the use of tracers was demonstrated. Neat PEO films were heated from 30 °C to 70 °C and Raman spectra were collected every 10 °C intervals. Structural information of the polymer is used to determine the temperature. Results indicate that by tracking Raman peaks of conformations that are sensitive to crystalline or amorphous domains, it is possible to measure the temperature of the sample. In addition, the information obtained is used to infer changes in crystallinity and could be used to monitor the molecular events taking place at the amorphous-crystal interfaces.

6.2. RAMAN SPECTROSCOPY BASICS AND APPLICATIONS

Raman spectroscopy is a major tool for the analysis of materials and can be used for both quantitative and qualitative analysis. Since the Raman spectra can provide information on chemical structure and composition, it can be used to monitor polymerization processes, polymer degradation mechanisms as well as crystallite dimension and orientation. Raman scattering is inelastic scattering of a light and was first reported by Raman in 1928 [138].

6.2.1. Raman Scattering

The scattering of light, basically, is a redirection of light that takes place when an electromagnetic (EM) wave (i.e. an incident light) encounters the obstacle material (solid, liquid or gas). As the EM wave interacts with non-homogeneities within the material, as shown in Figure 6.1, the electron orbits within the constituent molecules are perturbed periodically with the same frequency (ν_0) as the electric field of the incident wave. The oscillation or perturbation of the electron cloud results in a periodic separation of charge within the molecules, which causes a phenomenon called an induced dipole moment. As the induced dipole oscillates, it creates an EM radiation wave pointed in some new direction

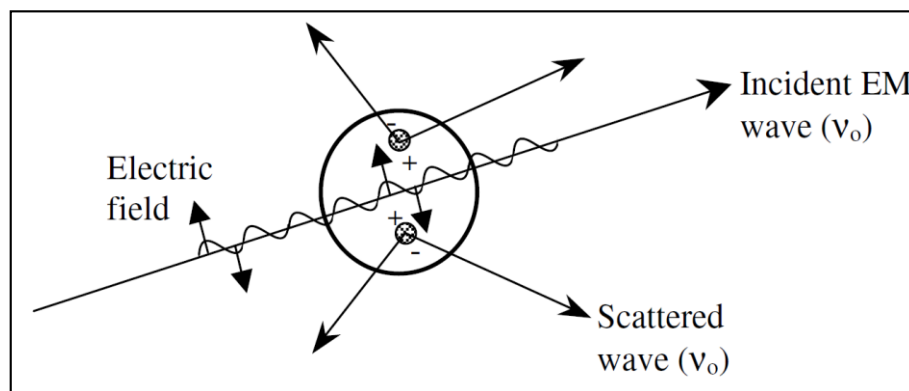


Figure 6.1. Schematic representation of an induced dipole and resultant scattered light

[139]

which is scattered light. Mostly, the light scattered has the identical frequency (ν_0) of the incident light, a process referred to as elastic scattering. However, at some cases, additional light is scattered at different frequencies, a process referred to as inelastic scattering. Raman scattering is one such example of inelastic scattering [139].

A Raman spectroscopy is generally performed via excitation source; most likely a laser with intense collimated monochromatic light. Therefore, measurements of small Raman shifts are enabled and Raman signal intensity is increased. In general, the Raman signal intensity is orders of magnitude weaker than the elastic scattering intensity, hence stray light can be a considerable issue. The difference between elastic and inelastic scattering can be 10^6 times for solid samples. While spectrometers are generally used to separate the elastic scattering and Raman scattering signals, the large mismatch in scattering intensity can enable the elastically scattered light to dominate the Raman light via stray light. Therefore, notch filters or edge filters (sharp cut-off high pass filters) are used to reject the elastically scattered light prior to entering the spectrometer [139]. Another problem associated with Raman spectroscopy is the fact that most polymers fluorescence strongly when exposed to laser irradiation. The problem can be reduced by using Fourier transform and resonance Raman techniques [140].

6.2.2. Applications of Raman Spectroscopy to the Study of Polymers

The use of Raman spectroscopy for the analysis of polymers become preferable choice, because the C-C and C=C bonds are found in many polymer backbones and Raman is the most convenient method to investigate C-C vibrational modes. In polymers, atoms are all linked together to form long chains resulting additional vibrational modes than of small molecules. Furthermore, long chains can possess ordering along the chain as well as between neighboring chains. Due to all these difficulties related to Raman spectroscopy, the IR studies are more commonly found in literature [140].

Perhaps the most common application of vibrational Raman studies is chemical identification of polymeric materials. Polymer products are rarely composed of a single component. Usually there are additives present that aid in processing, appearance, adhesion, chemical stability or other properties important to the function of the final

product. Thus, Raman Spectroscopy is used for probing chemical composition of polymers for biomedical applications [141, 142], nanophotonics [143] and molecular sensors [144]. The second important information on polymers obtained using Raman spectroscopy is presence of rotational isomers. The presence of *cis* and *trans* configurations and the relative ratios of each can be determined using Raman particularly due to its enhanced sensitivity to the local environments around C-C bonds in the chain backbone [140]. The major study on conformation of PEO, which also become a great reference for current work, is published by Yoshihara et al. [145] and developed by Maxfield et al. [136]. The intensive analysis of PEO has been presented and the spectral features were assigned to particular isomeric configurations.

Raman spectroscopy can also be used to follow the polymerization process and provide information on the extent of polymerization and structural information on the end-product. Simply monitoring the decrease in peak intensities of monomers would give information about conversion as a function of time [146, 147].

As it was mentioned in Chapter 4, there are several methods to study the crystallinity of polymers experimentally. Modern technology enables us to obtain crystallinity via X-ray diffraction or DSC. However, Raman and infrared vibrational spectroscopies probe the conformational states of the polymers, thus differences in the vibrational spectrum of chains in crystals with a unique, regular helical conformation and chains in non-crystalline regions with conformational irregularities or non-helical conformations can also be considered [99, 148]. The application of Raman spectroscopy to the study of crystallinity in polymers has been examined for polyethylene [149, 150]; polypropylene [151]; poly(ether ketone) [152]; polystyrene [153]; polyamides [154] and poly(ϵ -caprolactam) [155].

Schenzel et. al studied a Raman crystallinity index of partially crystalline cellulose samples [156] and defined crystallinity (X_c) as ratio between the mass fraction of the crystalline domains (M_c) and the total mass of the material (M), which consists of crystalline and amorphous portions.

$$X_c = \frac{M_c}{M_{Total}} \text{ and } X_c = \frac{M_c}{M_c + M_a} \quad (6.1)$$

Taking this into account, a Raman crystallinity index $(X_c)_R$ was defined to determine the percentage crystallinity.

$$(X_c)_R/\% = \frac{I_c}{I_c + I_a} \quad (6.2)$$

where I_c and I_a represent the Raman intensities of crystalline and amorphous portions of cellulose I [156]. In a work of Alloin et al. [137], poly (ethylene oxide) and complexes of lithium trifluorosulfonate-poly (ethylene oxide) (LiTf-PEO) have been studied by Raman spectroscopy from room temperature up to 160 °C. The Raman spectra of PEO which was obtained by them is given below;

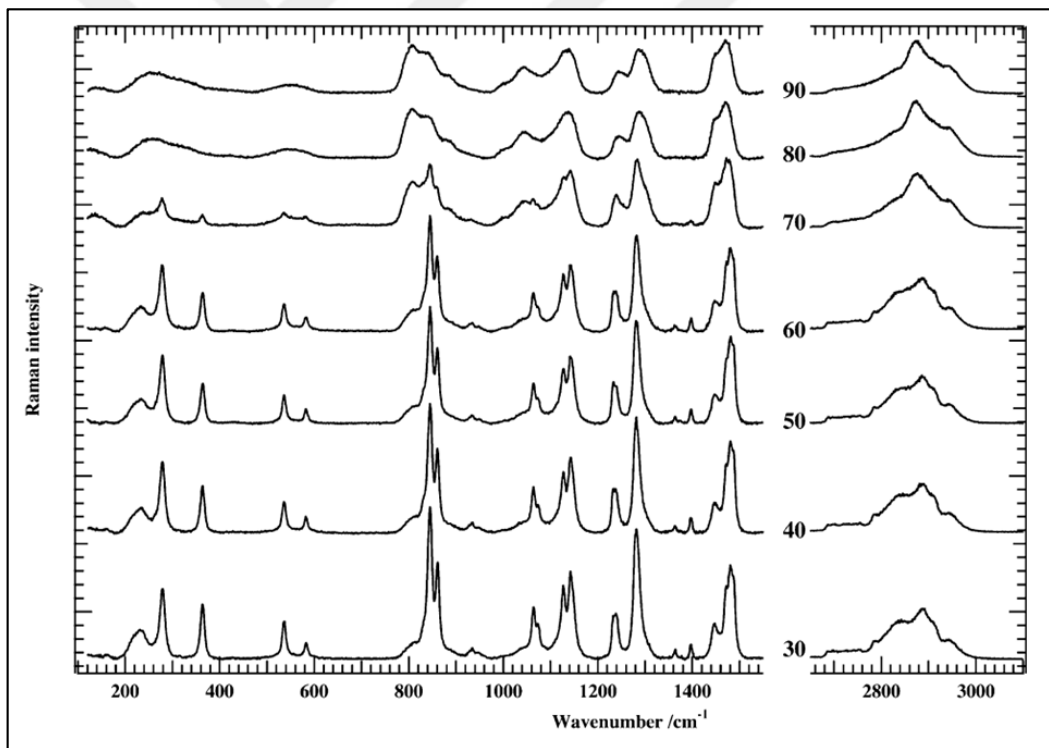


Figure 6.2. Raman spectra of PEO at various temperatures [137]

6.3. EXPERIMENTAL

Raman experiments of neat PEO film were performed as a function of temperature, which was controlled via a heating stage. In order to erase any prior thermal and process history, all samples were initially subjected to a heating/cooling cycle during which no data was collected. Raman spectra were collected during the third and fourth heating/cooling cycles at every 5 °C starting at 30 °C. All three heating/cooling cycles followed the same protocol as follows (also see Figure 6.3): Heating from room temperature to 80 °C at a rate of 3 °C/min; holding at 80 °C for 10 min; cooling to 30 °C for 30 min. During the cooling step, the heating stage was set to cool at a rate of 5 °C/min for 10 min, however, the sample does not necessarily cool at the same rate as the heating stage, therefore, a waiting period of 30 min was imposed between the onset of the cooling step and the start of the following heating step.

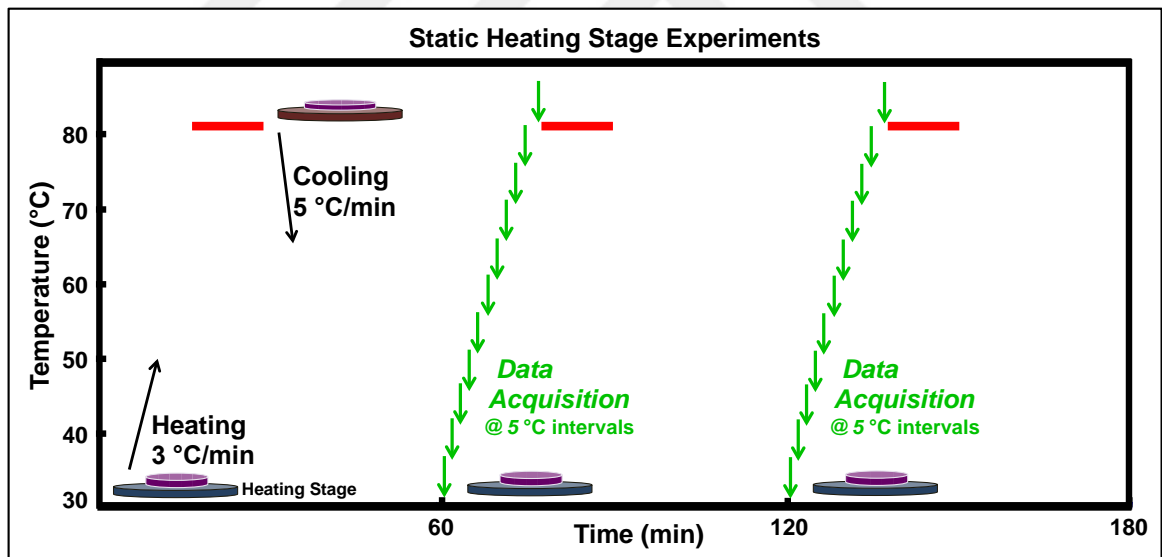


Figure 6.3. Raman spectrum was collected during second and third heating steps

A confocal raman microscopy (WITec 300R) equipped with 532 nm green light laser and CCD camera was used to collect raman spectra with 1 s integration time and 30 accumulations. The laser was set to operate at 16 mW and calibrated with a Newport Optical Power/Energy meter before each use. Since the Raman Spectrophotometer has its own heating stage, experiments could have been performed with single equipment.

6.4. RESULTS AND DISCUSSION

It is established that PEO crystallizes in a helical configuration (Yoshihara) and helical symmetry is shown in Figure 6.4. Filled (●) and blank (○) circles represent methylene groups and oxygen molecules respectively. The helical form of the polymer is constructed with succession of trans (CCOC), gauche (OCCO) and trans (COCC) conformers (tgt) along the chain [145]. Distribution of long chain lengths within the sample is being affected by increase in temperature and melting. Thus, changes in the spectrum are inevitable. The molten PEO spectrum is considerably different from that of the crystalline polymer. Such changes are to be expected in going from a highly ordered state to a disordered, essentially random structure. There are also some frequency shifts of existing bands, and the appearance of new bands, which can be associated with the formation of new conformational structure in the melt.

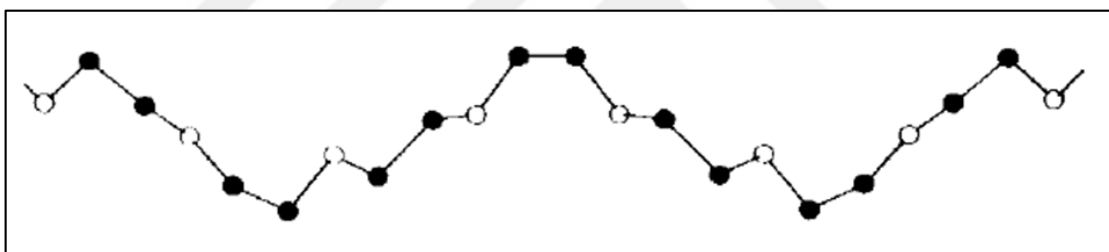


Figure 6.4. Molecular model of PEO with helical symmetry [157]

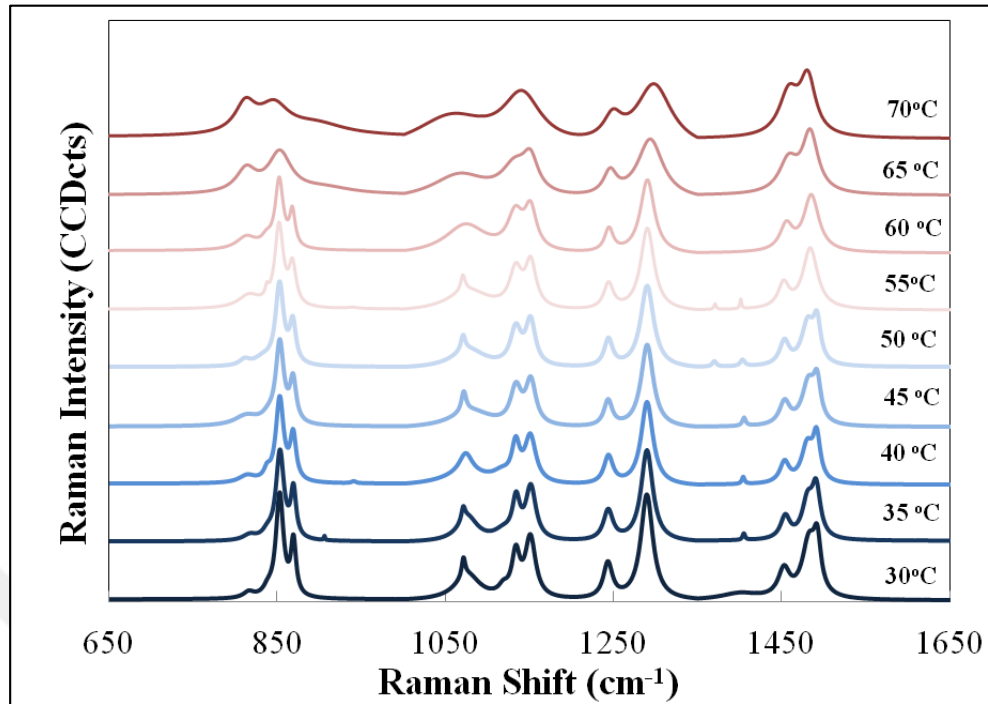


Figure 6.5. Raman spectra of PEO collected from 30 °C to 70 °C.

The conformational study of Maxfield et al. on solid and melt PEO [136] constitute the main motivation of this study. They listed the observed PEO Raman bands in the frequency range 800 cm^{-1} - 1500 cm^{-1} for the crystalline and melt structure and assigned these bands according to work of Yoshihara et al.[145]. Raman spectra of neat PEO ($M_w=600,000\text{ g/mol}$) film was collected as a function of temperature and shown in Figure 6.5. The band assignments are also adapted from above-mentioned studies and given in Table 6.1. The intensity of peaks decreases as the temperature of the sample increases. On the contrary, the width of the peaks broadens. The various well resolved band splittings observed in the spectra recorded at 30°C are a result of the ordered helical conformation [136] and disappear at the higher temperatures ($65\text{-}70^\circ\text{C}$). The very strong changes are observed after 60°C , which is close to the recorded melting temperature of PEO (67.9°C). Since the spectrum collected after 70°C is so smooth and the bands splittings are impossible to be detected, they are not presented here.

Table 6.1. Raman bands for crystalline and melt states of PEO. Mode assignments: r (rocking); τ (torsion); ν (stretching); w (wagging), δ (bending) [145]

Raman Shift (cm ⁻¹)		Assignment	Conformation
Crystal	Melt		
815	815	$r(\text{CH}_2)$	ttt
838	838	End groups	
852	852	$r(\text{CH}_2)$	tgt
869		$r(\text{CH}_2)\nu(\text{COC})$	tgt
	896		tgg, ggg
941		$r(\text{CH}_2)\nu(\text{COC})$	tgt
	1064	$r(\text{CH}_2)\nu(\text{COC})$	tgg
1071		$r(\text{CH}_2)\nu(\text{COC})$	tgt, ttt
1076	1074	$r(\text{CH}_2)\nu(\text{COC})$	tgt
1133		$\nu(\text{COC})$	tgt, ttt
1151		$\nu(\text{COC})$	t, g
1243	1243	$\tau(\text{CH}_2)$	tgt, ggg
1289	1289	$\tau(\text{CH}_2)$ $\tau(\text{CH}_2)$	ttt, tgt
1404		$w(\text{CH}_2)$ $\nu(\text{CC})$	tgt
1453	1453	$\delta(\text{CH}_2)$	tgg, tgt
1480	1480	$\delta(\text{CH}_2)$	tgt
1491		$\delta(\text{CH}_2)$	tgt

Considering the plots in Figure 6.5 and band assignments in Table 6.1, the Raman bands at 815, 852, 1076, 1243, 1289, 1453 and 1480 cm⁻¹ were found to appear for both crystalline & melt states and chosen for further analysis. The peak intensity of those bands was particularly studied.

The numerical analysis of the peaks was studied via Origin Pro 9.1. [158]. The best fit-curve was selected via Lorentzian curve fit function. Lorentzian curve fit function is utilized in spectroscopic curve fitting, mostly for polymer and carbon nanotube spectra [159-161]. It is a continuous probability density function suitable for manipulating non-linear curves. The parameters of Lorentzian curve fit function are given as;

$$y = y_0 + \frac{2A}{\pi} \frac{w}{4(x - x_c)^2 + w^2} \quad (6.3)$$

$$y_c = y_0 + \frac{2A}{w\pi} \quad (6.4)$$

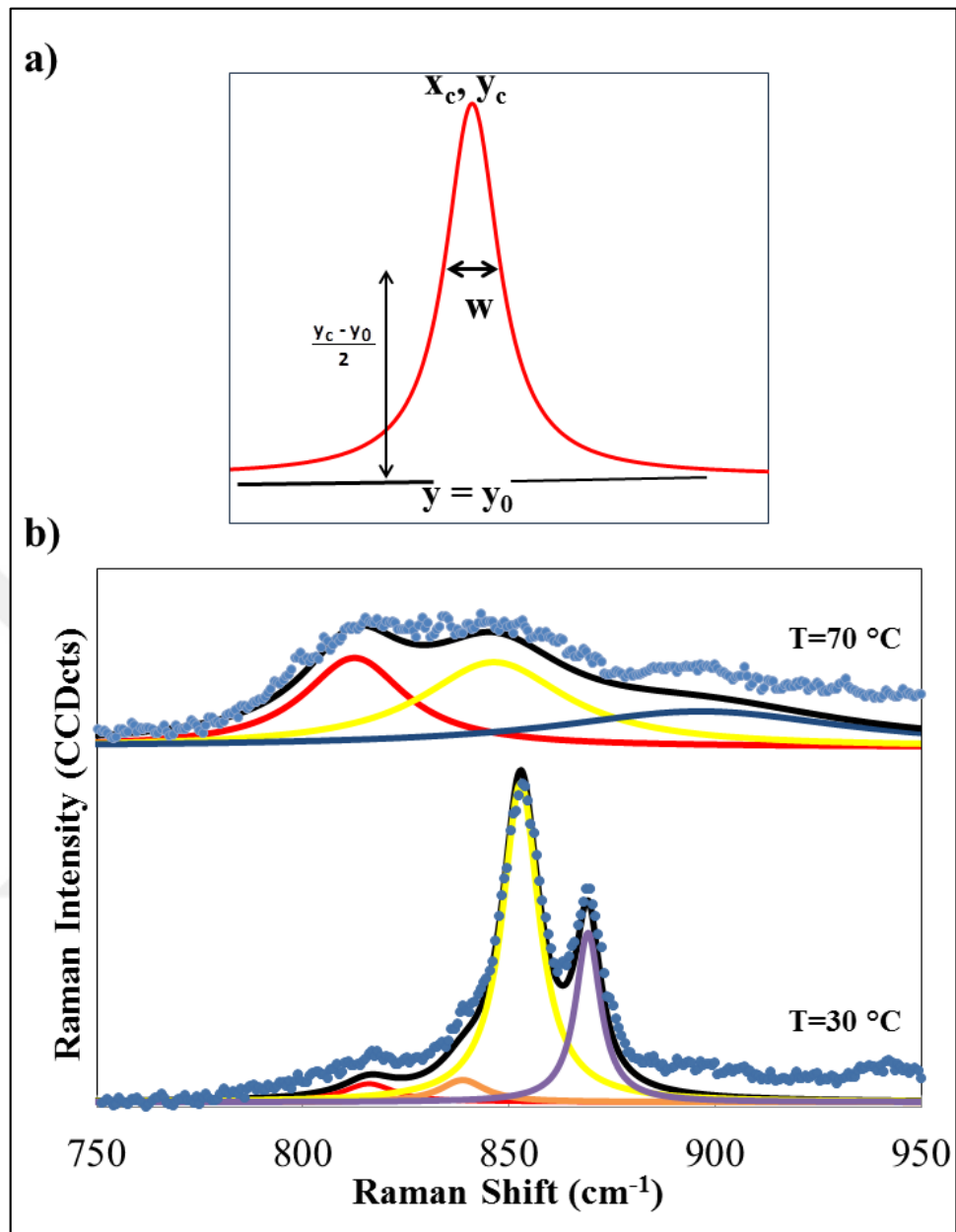


Figure 6.6. (a) Parameters defined in Lorentzian peak function; (b) Lorentzian curve fit to Raman spectra of PEO at 30 °C and 70 °C

Where A is area under the curve and w is width. Other parameters are given in Figure 6.6.a. In order for better understanding; consider blue dots in Figure 6.6.b representing raw PEO spectra recorded at 30 °C and 70 °C between frequency range of 750 cm^{-1} and 950 cm^{-1} . At 30 °C, four Lorentzian curves with $y_c = 815$ (red); 838 (orange); 852 (yellow) and 868 (purple) cm^{-1} are needed to fit the spectra, nevertheless peak at 838 cm^{-1} no longer

exist and peak at 868 cm^{-1} shifts to 898 (dark blue) cm^{-1} at higher temperatures. Thus, only three Lorentzian curves were enough to fit the spectra at $70\text{ }^\circ\text{C}$; $y_c = 815, 852$ and 898 cm^{-1} .

Raman intensity (x_c , in Figure 6.6.a.) data for specific peaks were normalized to their initial value at $T=30\text{ }^\circ\text{C}$ and presented in Figure 6.7. The intensities of bands with y_c of $1076, 1453$ and 1480 cm^{-1} do not change dramatically with temperature, even after T_m . It is known from literature that in the Raman scattering spectra the PEOs, in the conformation gauche about the C-C bond are assigned to the band at $852, 1243$ and 1289 cm^{-1} , while the PEOs in the

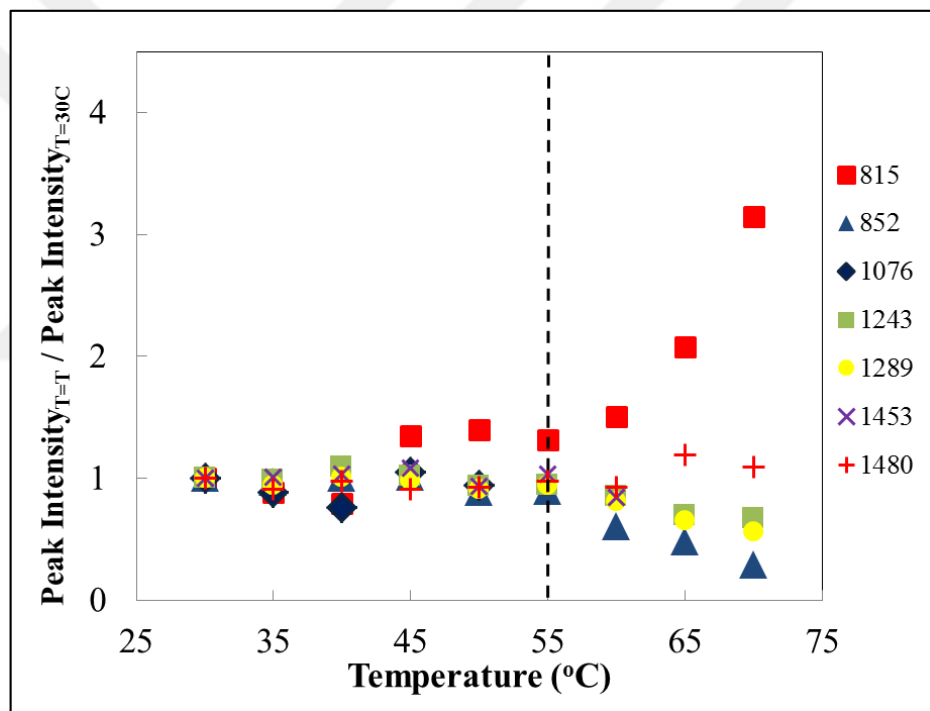


Figure 6.7. Normalized peak intensities recorded from $30\text{ }^\circ\text{C}$ to $70\text{ }^\circ\text{C}$

conformation trans about the C-C bond to the band at 815 cm^{-1} (See Table 6.1). That explains the reason why the intensity of band at 815 cm^{-1} increase with temperature. Recalling the gauche conformation in C-C backbone is dominant for crystalline state; number of gauche peaks is expected to decrease, eventually diminish, at elevated temperatures. On the other hand, amorphous chains will dominate the structure in melt state. It is because only the band at 815 cm^{-1} is responsible for trans conformation of C-C backbone, the intensity of this particular band radically increases at elevated temperatures.

Figure 6.8 represents the intensity change of bands at 815 and 852 cm^{-1} ; those are only responsible for trans and gauche conformations respectively.

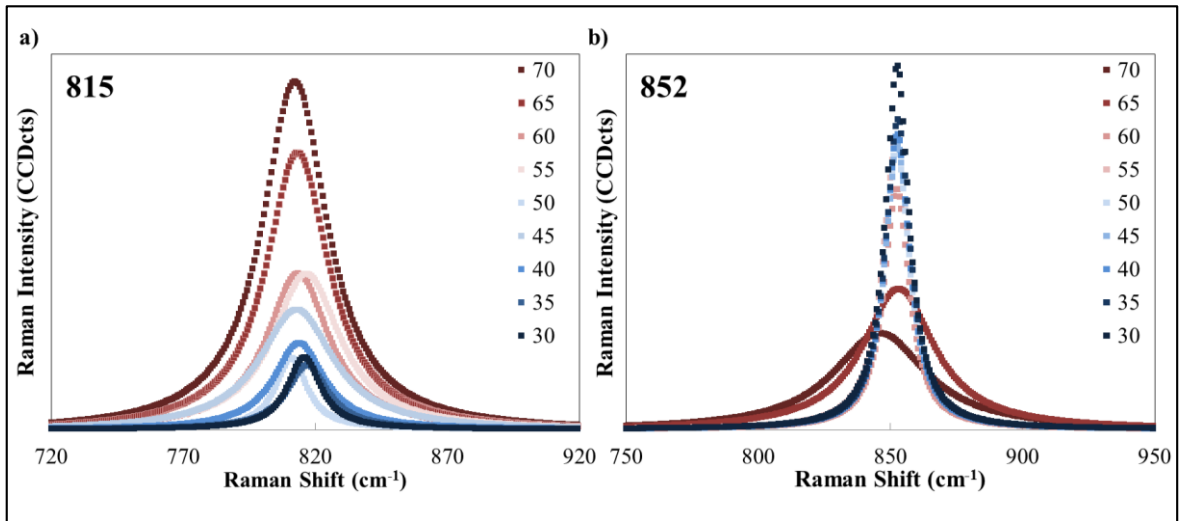


Figure 6.8. Intensity of (a) Trans and (b) Gauche peaks as a function of temperature

It is well known that semi-crystalline polymers consist of both amorphous and crystalline domains. PEO is also an example of semi-crystalline polymer and number of amorphous and crystalline chains would give an idea about Raman crystallinity index (X_c)_R of the sample as it was mentioned before. Crystallinity, X_c , in semi-crystalline components is defined as ratio of mass fraction of the crystalline domains over total mass of the material [156]. Using the eqn. 6.2, the crystallinity of PEO was calculated as a function of temperature and presented in Figure 6.9. Intensity of two selected peaks; trans ($y_c = 815$) and gauche ($y_c = 852$); were used as I_a and I_c respectively.

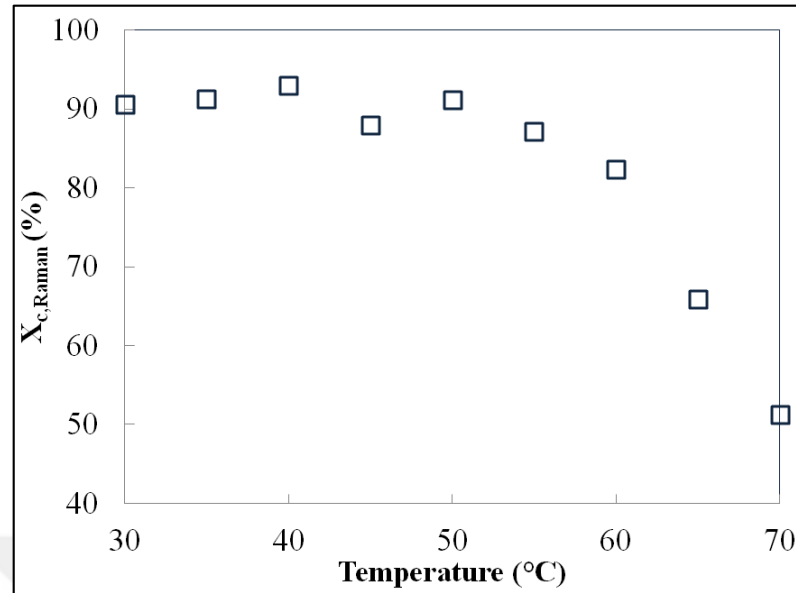


Figure 6.9. Raman crystallinity index of neat PEO as a function of temperature

Raman crystallinity of neat PEO film at 30 °C was recorded as 90.6 % and started to decrease after 55 °C. It reaches to 51.3 per cent at 70 °C and 43.3 per cent of decrease in crystallinity is attributed to increase in number of amorphous chains while PEO is getting melted. The major change; a decrease of 37.7 per cent in crystallinity; appear after 60 °C due to melting.

6.5. CONCLUSION

Conformational and crystallinity changes of PEO with temperature were investigated at this part of the study. In order to make a quantitative analysis, Raman spectra of the sample was recorded as a function of temperature and peak intensities were studied via Lorentzian curve fit function.

Raman spectra of neat PEO at 30 °C gave distinct and sharp band splittings. After analysis of the spectrum data with Lorentzian function, appropriate conformational assignments were customized to each specific Raman band with taking the work of Maxfield et al. [136] as a basis. The procedure was repeated for data collected at 10 °C intervals. The results were consistent with literature; increase in the width and decrease in intensity of the

peaks were detected via increasing temperature. After certain temperature, the spectral changes, loss of ordered modes and appearance of new bands were observed. Some of the bands were found in both crystalline and melt spectra, however some of them shifted or vanished after 60 °C. While the majority of peak intensities were found to decrease with temperature; one specific band exhibits tremendous increase. The very weak band appeared at 815 cm⁻¹, which is assigned to rocking vibration of ethylene bonds when the C-C backbone is at trans conformation, were particularly investigated. On the other hand, the neighboring band appeared at 852 cm⁻¹ were found to assign to rocking vibration, but this time for gauche conformation of ethylene bonds. With knowing the information that PEO crystals consist of helical structures having trans (CCOC), gauche (OCCO) and trans (COCC) conformations, it was concluded that the band at 852 cm⁻¹ is attributed to CH₂ rocking vibration of crystalline chains in PEO. Contrarily, the band at 815 cm⁻¹ arises due to CH₂ rocking of amorphous chains and the relatively low intensity of this band at melt state is quite straightforward. While the intensity of amorphous peak triples from 30 °C to 70 °C, almost 20 per cent of decrease in intensity of crystalline peak is recorded.

Moreover, it is possible to predict Raman crystallinity of PEO via temperature with placing the intensities of crystalline and amorphous peaks into equation that was developed by Schenzel et al. [156]. This calculation enabled us to make a quantitative analysis of crystallinity change via temperature. The crystallinity of PEO was found to decrease from 90.6 to 51.3 per cent with increasing temperature due to subsequent movements of unordered chains. The melting of the polymer also triggers the fall in crystallinity after 60 °C.

Here we presented a relationship between crystallinity and temperature of the PEO polymer. The one who studies Raman spectroscopy of polymers, can easily conduct a calibration curve which gives crystallinity of polymer as a function of temperature. Besides, nanofillers can be added to system and used to track the local temperature change using the calibration curve plotted.

7. ACTIVATION OF GOLD NANOPARTICLE/POLYMER SYSTEMS VIA PHOTOTHERMAL EFFECT TO DEVELOP SHAPE MEMORY POLYMERS

7.1. INTRODUCTION

Photothermal effect is a phenomenon that is generally associated with electromagnetic radiation leading to the release of thermal energy due to the photoexcitation of the material. This effect converts light energy into heat via coupling with the nanoparticle surface plasmon resonance (SPR); thus, metal nanoparticles can act as externally-driven, nano-sized thermal sources embedded in the material, providing efficient, selective, and remotely-controlled localized heating when the material (doped with a small fraction of nanoparticles) is irradiated with relatively weak light. This property of metal nanoparticles [162, 163] has been previously investigated [164-168] and utilized in aqueous environments for biomedical applications such as treatment of blood vessel lesions, laser resurfacing, laser hair removal, laser surgery, and cancer treatment [169-171]. However, few studies reported how the photothermal effect might be usefully applied to a solid medium for morphology control, processing, or (remote) actuation [172-174].

Shape memory polymers (SMP) emerge as a new class of smart materials which are capable of memorizing temporary shapes and reverting to their permanent shapes upon external stimulus. The recovery process is generally initiated through light, magnetic field and most commonly thermal energy [175]. Typical transition temperatures for SMPs are round 70 °C, which is easily attainable via photothermal heating. In addition, the particle concentration and illumination power intensity can be increased to sufficiently elevate the sample temperature for shape-memory polymer actuation. The heating is spatially selective to sample regions where the nanoparticles are placed; moreover, in side-by-side regions doped with nanoparticles of differing composition, the effect is also spectrally selective, enabling the possibility of multi-step or sequential actuations. Clearly, a wealth of complex, stimuli-responsive materials could be enabled by this technology: in situ

activation of shape-memory materials could be accomplished without significant warming of the surrounding environment.

In this part of the work, photothermal heating caused by gold nanoparticles dispersed in polymer matrices are investigated. A green laser operating at 532 nm was used to actuate the irradiation and local temperature profile of the polymer was estimated via fluorescence spectrophotometer. Previously synthesized magnetite nanoparticles were added to polymers; in order to show thermo responsive recovery and shape memory properties even though the original material does not exhibit these properties. On the other hand; a novel shape memory system is proposed which can be stimulated either by magnetic field and/or photothermal effect.

7.2. PHOTOTHERMAL EFFECT

Metals; both in nanoscale and bulk metals are defined by quasi-free electrons in the ground state, which are not bound to single atoms but to the metal bulk. These free electrons are responsible for the well-known properties of high electric conductivity and high optical reflectivity. Qualitatively, the free electrons of the metal behave like a gas of free charge carriers (plasma) and can be excited to sustain propagating plasma waves. These waves are longitudinal electromagnetic charge density waves and their quanta are referred as plasmons. They exist in two forms; bulk plasmons in the volume of plasma and surface plasmons, which are bound to the interface of plasma and a dielectric. Surface plasmons exist for metals like Au, Ag, Al and Cu, etc. [176]. Surface plasmon resonance (SPR) is a phenomenon which is due to the boundary conditions imposed on wave propagation by the limited spatial extent of the particle (see Figure 7.1.).

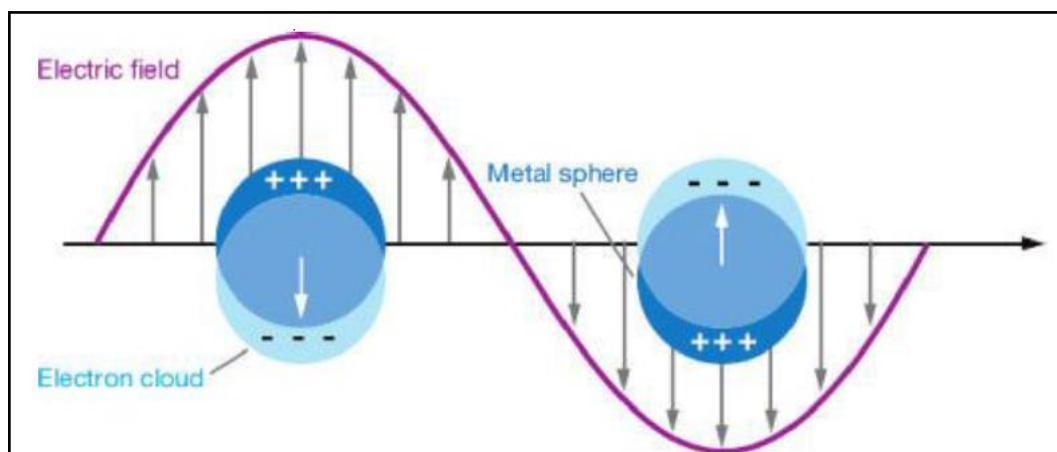


Figure 7.1. Schematic of surface plasmon resonance manifested by metal nanoparticles [177] (An external electromagnetic radiation disturbs the valence electron cloud leading to fluctuations/movement of electrons)

The excitation of material via electromagnetic irradiation and obtaining heat is called photothermal effect. It can be basically defined as conversion of light into heat. Photothermal effect evolves under surface plasmon resonance created by metal nanoparticles. This effect is generally used in various applications such as molecular sensing, tagging, focusing of light, near-field optical microscopy and sub-wavelength photonics [178]. The SPR frequency is strongly dependent upon the nanoparticle composition (i.e., dielectric constant of the noble metal), size and shape (e.g., aspect ratio) and to a lesser extent, the dielectric properties of the surrounding medium [166, 179]. This property allows “tuning” of the SPR-frequency to optimally match the transmission characteristics of the polymer medium within which the selected particle is embedded, i.e., choosing a nanoparticle such that its SPR-frequency matches the absorption minima of the material. As a general example of noble metal nanoparticle SPR frequencies, for gold spheres (10-80 nm in diameter) the absorbance maximum occur around 530 nm while similarly-sized silver nanoparticles exhibit a higher SPR frequency around 400 nm.

In the SPR-mediated heating process, application of light polarizes the metal nanoparticle, creating a non-equilibrium electron distribution that decays via electron-electron scattering. The hot electron gas rapidly equilibrates with lattice phonons, which subsequently relax this energy into the surrounding medium [180].

7.3. SHAPE MEMORY POLYMERS (SMP)

7.3.1. Shape Memory Effect (SME)

Shape memory effect is not an intrinsic property. Polymers do not show this property by themselves; the stimuli response is triggered via stimuli-sensitive switches and net points (Figure 7.2.). The netpoints determine the permanent shape of the polymer network and can consist of chemical (covalent bonds) or physical (intermolecular interactions) nature. The transition temperature (T_{trans}) for a SMP can be a glass transition (T_g) or a melting transition (T_m) [181]. When the SMP with an original shape (shape B) is heated above the T_{trans} and formed into a temporary shape by compression, extrusion or molding, they memorize the new shape.

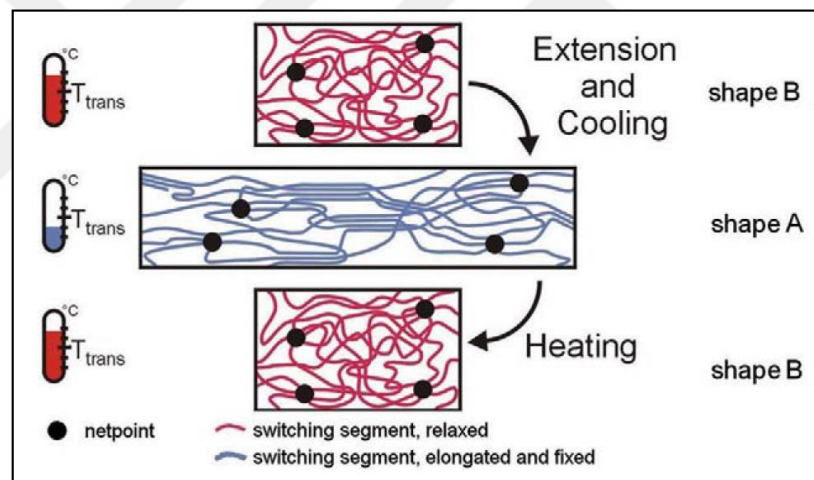


Figure 7.2. Shape memory effect [181]

The deformed shape is then cooled below T_{trans} (and fixed) while keeping the deformation (shape A, temporary shape). This process is called ‘shape memory creation procedure’ (SMCP) [182]. After creating the SMP, the temperature is again increased above T_{trans} and the SMP recover its original shape B. The recovery of the original shape is called ‘shape memory effect’ (SME). SMPs of the polyurethane (PU) series have been used in several fields of practical applications. The examples of applications according to the function of the materials can be listed as; temperature sensors for the variation in modulus of elasticity depending on temperature; medical catheters for their adaptability owing to its flexibility

and anti-thrombotic nature; a spoon or fork handle for a handicapped person for shape fixity and shape recoverability. The applications using these properties are also favorable; humidity permeability, volume expansion, damping property and refractive index [183].

Polystyrene (PS) has been widely used as hard segments in copolymers for nanocomposite design and applications, because of its low cost comparing to the other tough polymers such as PMMA, PU or polycarbonate, etc. Self-healing scheme was demonstrated by Nji et al., by fabricating a composite with thermoplastic particles dispersed in a shape memory polymer matrix (Veriflex Polystyrene) in which the confined shape recovery of the shape memory matrix is utilized for sealing (closing) cracks and the thermoplastic particles are used for molecular-length scale healing [184].

Another biomedical application of SMPs involves laser-activated device for the mechanical removal of blood clots [185] and biodegradable intragastric implants for obesity that inflate after an approximate predetermined time and provide the patient with a feeling of satiety after only a small amount of food has been eaten [186]. Shape-memory foams have been proposed as a measuring device to survey the shape of a human ear canal, so a hearing aid can be fitted properly [187].

7.3.2. Magnetic Nanocomposites with SME

Magnetite (Fe_3O_4) nanoparticles became essential after wide application area in industry as well as the biomedical field including drug delivery, magnetic hyperthermia and magnetic resonance imaging due to its unique magnetic and biocompatible properties [188]. Shape memory applications were previously studied on magnetite filled polymers. Razzaq et al. had shown that shape recovery of polyurethane filled with microsize magnetic particles by an electromagnetic field of low frequency and low field strength is possible [189]. Puig et al. had prepared uniformly dispersed oleic acid coated magnetite filled diglycidylether of bisphenol A (DGEBA) and demonstrated the shape memory effect with applying alternating magnetic field [190].

The nanocomposite composed of cross-linked poly (ϵ -caprolactone) (c-PCL) and magnetite nanoparticles showed excellent shape memory properties via application of magnetic field

[191]. The magnetic field induced shape recovery behavior of biocompatible poly (D, L-lactide) (PDLLA, $M_w = 152$ kDa)/magnetite nanocomposites of different composition was also investigated. The shape memory effect had been detected with the addition of magnetite nanoparticles to PDLLA, although the pure PDLLA does not present any shape memory effects [192].

7.4. EXPERIMENTAL

7.4.1. Preparation of Polymer Nanofilms with Perylene

In order to detect the fluorescence signals, perylene (Sigma Aldrich, > 99.5 %) molecules were randomly added to polymer matrices (not tethered). The procedure for preparing nanofilms dispersed with fluorescence molecules is as follows; 0.57 g of poly (ethylene oxide) (PEO, POLYOX™, WSR 205, $M_w=600,000$ g/mol) powder, 15 ml of chloroform (Sigma Aldrich, anhydrous, ≥ 99 %) and previously prepared Au NP (Au10/o, explained in Chapter 1) solution with required amount was mixed under magnetic stirring overnight in glass vial. Then perylene (at amount of 1.05 per cent by wt of PEO) was added to PEO/NP solution and glass vial was covered with aluminum foil in order to prevent exposure from light. After one hour of complete mixing, the solution was transferred to glass vial ($d= 5$ cm) and chloroform was left to evaporate in dark oven operating at 32 °C. Identical procedure was applied to prepare neat PEO films with perylene, only with PEO, chloroform and perylene. Resulted films have 5 cm of diameter and a thickness of 0.16 ± 0.03 mm.

7.4.2. Investigation of Local Temperature Profiles Induced by Photothermal Effect in Metal Nanoparticle/Polymer Nanocomposites via Fluorescence Spectrophotometry

The temperature change due to photothermal effect caused by Au NPs in PAu10-0.1 and PAu10-1 nanofilms were observed through fluorescence spectrophotometry. Fluorescence scanning measurements were performed via Cary Eclipse Fluorescence Spectrophotometer equipped with PCB-150 peltier water bath and single water thermo cell holder. A fluorescence cell with 10 mm depth and 3.5 ml liquid capacity was used. The nanocomposite films were cut into rectangular pieces with dimensions of 3 cm x 1 cm (height x width) and pasted on side of the fluorescence cuvette. The fluorescence cells were placed in single water thermo cell holder and an optic fiber was used to both excite and collect the fluorescence of the sample between 425 and 800 nm with an excitation wavelength of 420 nm. Prepared polymer films were first heated to 80 °C in oven, left to stand at this temperature for one hour and then cooled to room temperature to erase the thermal history prior to cutting.

Static heating experiments were conducted with heating the polymer films using the PCB-150 peltier water bath from 25 °C to 80 °C and collecting fluorescence spectrum every 5 °C. Photothermal heating experiments were performed with irradiating samples with green light at a wavelength of 532 nm. A 65 mW, 532 nm pulsed-wave diode laser (Kenar Mühendislik, SUA532-0100) was adjusted to shine the sample from distance of 2 cm and illumination area was found as 0.2 cm². Both laser and static heating experiments were repeated at least two times in order to ensure accuracy.

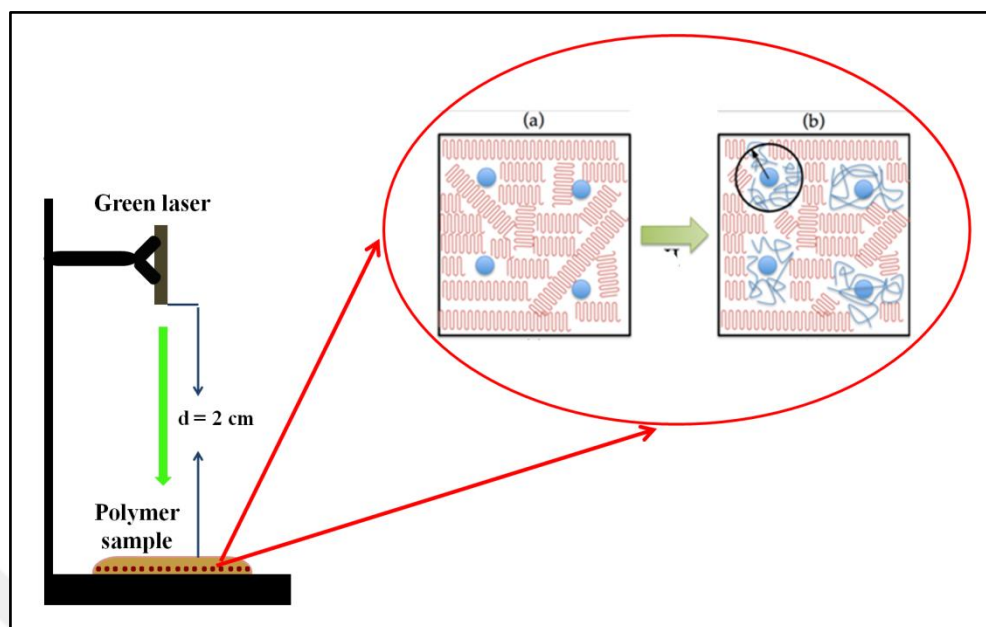


Figure 7.3. Neat PEO, PAu10-0.1 and PAu10-1 nanofilms are exposed to green light from a distance of 2 cm. (a) PEO chains (red) dispersed with Au NPs (blue); (b) After irradiation, NPs will provide effective heating and cause the movement of polymer chains and melting eventually.

7.4.3. Preparation of Shape-Memory Polymers (SMP) and Activation with Heat

Fe_3O_4 nanoparticles were synthesized by co-precipitation (or chemical precipitation) method which is a facile and simple technique that uses the stoichiometric mixing of ferrous and ferric ions (2/1) in an inert environment followed by the addition of base to precipitate superparamagnetic magnetite particles [188]. In a typical synthesis, 0.242 g of ferrous sulfate heptahydrate ($\text{FeSO}_4 \cdot 7\text{H}_2\text{O}$, Riedel-de Haen), 0.282 g of ferric chloride (FeCl_3 , Riedel-de Haen, anhydrous) and 2 ml of oleic acid (Aldrich, 65.0-88.0 %, GC) were dissolved in 80 mL ultrapure water at 80 °C, which was de-aerated for 30 minutes using a N_2 flow to remove dissolved oxygen, by mixing for 15 min using a mechanical stirrer at a constant stirring rate of 50 rpm. Addition of 0.514 g of NaOH (Merck, pure pellets) solution (20 mL) to the aqueous iron mixture caused immediate precipitation of magnetite as indicated by a rapid color change from yellow to black. The reaction was carried out for 30 minutes and the solution was left to cool to room temperature. The NP solution was washed, centrifuged with acetone for three times and finally supernatant was

removed. The particles were then dried in a vacuum oven at 60 °C for overnight. Formed nanoparticles are known to have a size distribution of 6-12 nm with various morphologies [188].

Polymer nanofilms were prepared using solvent evaporation method; 0.1 g of Poly(DL-lactide-co-glycolide) (PDLLA, Sigma Aldrich, Resomer® RG 503 H, $M_w = 50,000-75,000$ g/mol) was dissolved in 10 ml of dichloromethane (DCM, Sigma Aldrich, anhydrous, $\geq 99.8\%$) under magnetic stirring. The solution was transferred to petri dish ($d=3.5$ cm) and left to evaporate for overnight in oven operating at 32 °C. Fe₃O₄ filled PDLLA nanofilms were also prepared with adding dry Fe₃O₄ nanoparticles to PDLLA/DCM solution with magnetite concentrations varying from 0.25 to 5 per cent (by wt). Resulted nanofilms were named as; PMag0.25, PMag0.5, PMag1.25, PMag2.5 and PMag5.

Static heating experiments were performed with these films in order to see shape memory effect;

- The initial shape of the SMP is achieved via solvent evaporation of polymer solution at room temperature; which is *permanent* and *straight*.
- The SMP is then heated above T_{trans} (which was determined as 70 °C for PDLLA based nanocomposites) and deformed into a secondary shape by folding it. The secondary shape is *temporary* and *folded*.
- The twisted SMP is cooled below its T_{trans} (70 °C), and the shape is fixed at low temperature. The new shape becomes *fixed*.
- Then, the films are heated above their T_{trans} , and checked if they recover their initial (*permanent* and *straight*) shapes.

7.4.4. Activation of Shape-Memory Polymers (SMP) with Gold Nanoparticles

Previously prepared Au NPs (Au10/o, see Chapter 1) were added to SMP (PMag5) at different ratios. The nanofilm preparation method was again the same; magnetic stirring of DCM, magnetite particles and Au NP solution at desired amount (1, 2 and 5 per cent, by wt) and then leaving the solution at petri dish for solvent evaporation at 32 °C in oven. PMag nanofilms with and without Au NPs were first heated to 80 °C in oven, left to stand at this temperature for one hour and then cooled to room temperature to erase the thermal history prior to cutting.

Light induced stimulation of shape memory polymer (PMag) was aimed to actuate via irradiation with laser. Laser experiments were performed with irradiating samples with green light at a wavelength of 532 nm. A 65 mW, 532 nm pulsed-wave diode laser (Kenar Mühendislik, SUA532-0100) was adjusted to shine the sample from distance of 2 cm.

The procedure for laser heating experiments is as follows;

- The initial shape of the SMP is achieved via solvent evaporation of polymer solution at room temperature; which is *permanent* and *straight*.
- The SMP is then heated above T_{trans} (which was determined as 70 °C for PDLLA based nanocomposites) and deformed into a secondary shape by folding it. The secondary shape is *temporary* and *folded*.
- The twisted SMP is cooled below its T_{trans} (70 °C), and the shape is fixed at low temperature. The new shape becomes *fixed*.
- Then, the films are heated above **65 °C**, and checked if they recover their initial (*permanent* and *straight*) shapes.
- If heating to **65 °C** is not sufficient to shape recovery, films are irradiated with green light for 30 minutes and checked if they recover their initial (*permanent* and *straight*) shapes.

The laser shine experiments were conducted in an isolated reactor in order to avoid heat loss.

7.5. RESULTS AND DISCUSSION

7.5.1. Fluorescence Experiments

For the past few years, fluorescence spectrophotometer is being used to determine thermal transitions in polymer systems [193, 194]. Conventional techniques like differential scanning calorimetry record the response of a material while fluorescence spectroscopy records the response of specific fluorescent sites within a material [194].

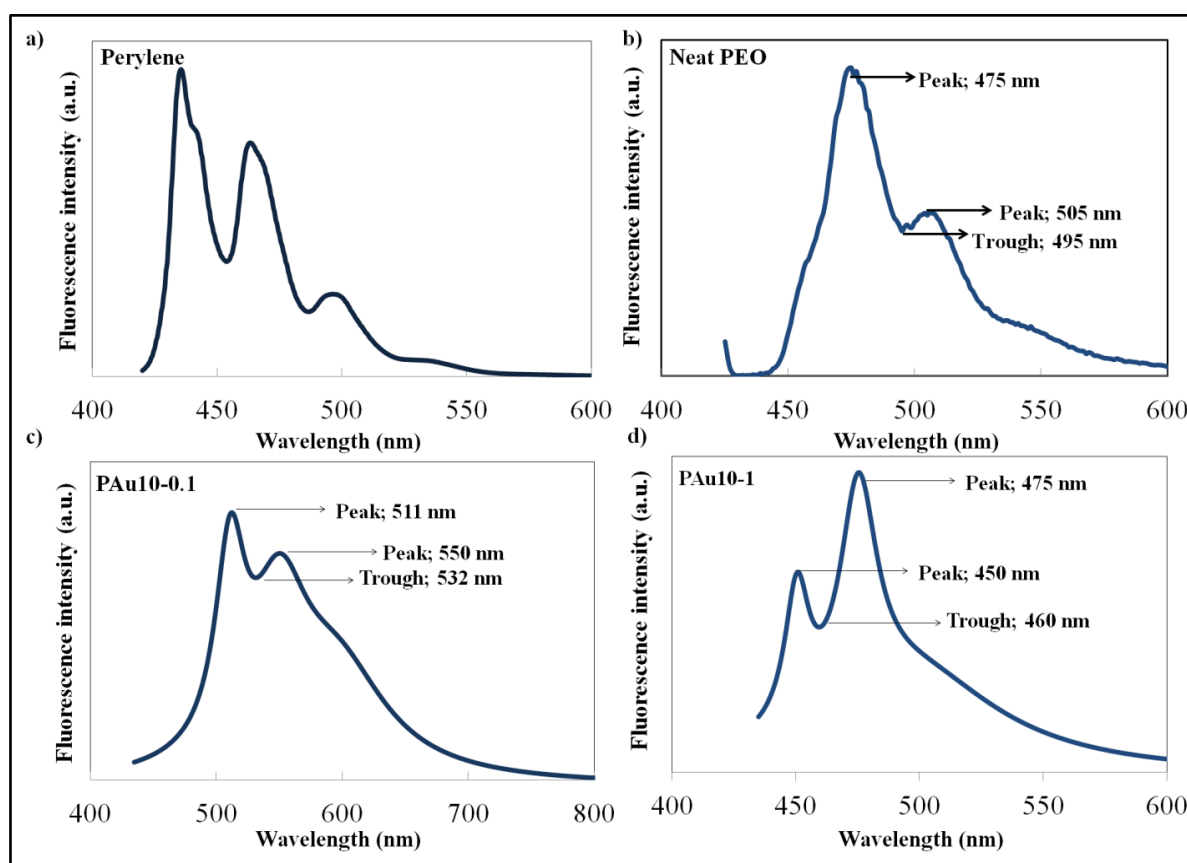


Figure 7.4. Fluorescence spectrums and peak locations for (a) Perylene solution [195]; (b) Neat PEO; (c) PAu10-0.1 and (d) PAu10-1 at room temperature

It is because the fluorescence signal is taken from the adjacency of the fluorescent molecule (fluorophore), it represents the changes in local environment. In order to determine the quantitative method that is going to be followed during photothermal studies, all the nanofilm samples were scanned with spectrophotometer. It was known that

the peaks of perylene spectra are found in the region between 400 and 600 nm [195], therefore experiments were conducted in this range. The experiments at room temperature revealed that the spectra of perylene with same amount were similar in trend but the peaks change with concentration of Au NPs present. For example, the spectrum for perylene in neat PEO was recorded as two 'peaks' at 475 nm (high) and 505 nm (low), one 'trough' between them at 495 nm (See Figure 7.4.b). However, for the PAu10-1 sample, the curve found to be symmetrical to the one in neat PEO's.

A fluorophore is a component that causes a molecule to absorb energy of a specific wavelength and then re-emit energy at a different but equally specific wavelength [196]. The amount and wavelength of the emitted energy depend on both the fluorophore and the chemical environment of the fluorophore. As it was explained in mechanical properties of polymer films (Chapter 4), the interactions between polymer chains and nanofillers change with increasing NP concentration. The conformational changes get dominant at higher NP concentrations. At our case, the intramolecular interactions between fluorophores, NPs and PEO chains would significantly affect the spectrum. In the work of Cossello et al. [197], it was mentioned that the shifts in the fluorescence spectra can be caused by; (i) the conformational changes of the polymer chain; (ii) the formation of aggregates and (iii) interaction with solvent; which is predominantly responsible for shifts in spectrum might occur during further solvent evaporation process. Therefore calibration curves were plotted for each specific nanofilm sample in order to be able to evaluate each sample in itself.

Another handicap during the experiments was derived from the fluorescence quenching property of Au NPs. The quenching [198, 199] or enhancement [200] of fluorescence was explained by the energy transfer between fluorophores and Au NPs by several researchers. Therefore, the fluctuated and noisy output data from the spectrophotometer software was smoothed using Origin Pro 9.1. [158]. Peaks evaluated in this study are listed in table below:

Table 7.1. List of peaks evaluated for fluorescence experiments

Sample	Peak locations (nm)	
	λ_{Trough}	$\lambda_{\text{Low peak}}$
Neat PEO	495	505
PAu10-0.1	532	550
PAu10-1	460	475

7.5.1.1. Fluorescence Experiments with Neat PEO

Static (conventional) heating experiments were performed first to see the changes in fluorescence spectra of adjacent perylene molecules with temperature. The photothermal heating of PEO was also performed to check whether perylene molecules or PEO chains get affected from laser light. The ratio of amplitudes of trough (495) to low peak (505) was evaluated and normalized plots are presented for better visualization.

Fluorescence amplitude ratio of trough to peak for static heating neat PEO was found to increase with elevation of temperature. The ratio reaches its maxima (almost 111.5 per cent of its initial value) at 80 °C. The increase in temperature causes relaxation of polymer chains and subsequent movements. Therefore the dispersed perylene molecules relocate. A nonuniform dispersion of fluorophores results variations in emission spectrum in consequence of altered local perylene concentrations. Also the emission pathways are affected dependently on photo-physical properties of fluorophores and polymer relaxation processes [201].

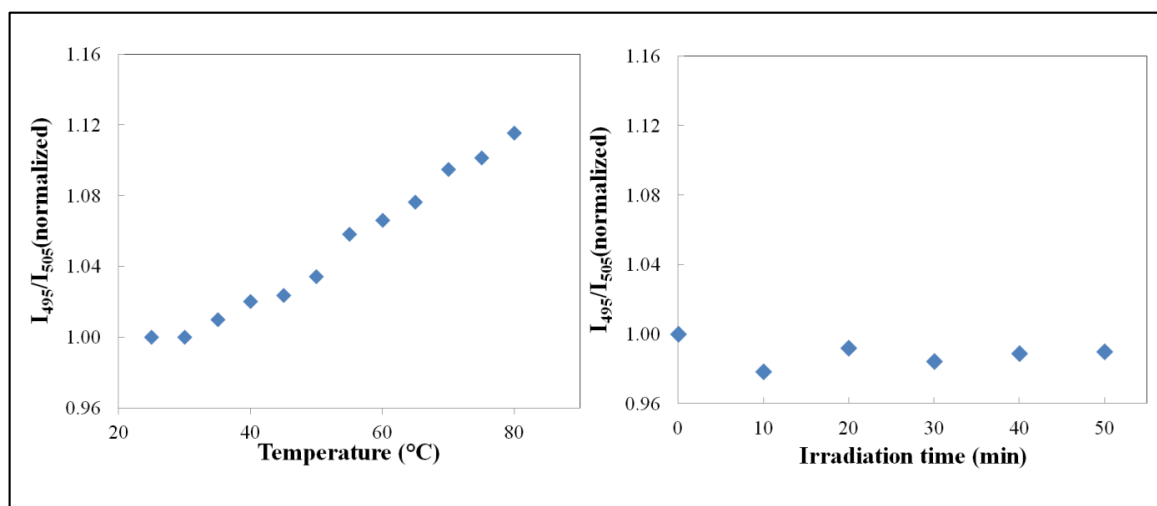


Figure 7.5. Fluorescence amplitude ratios of trough to peak for static and photothermal heating of neat PEO.

The linear increase in peak ratios states that the spectra of perylene become smooth with the increase of temperature. The laser irradiation, on the other hand, has no effect on perylene spectrum. After 50 minutes of green light exposure, the peak ratio still remained same. The result was expected; it was proved that any change in spectra of nanofilm will not occur due to polymer chain or perylene in the presence of green light exposure.

7.5.1.2. Fluorescence Experiments with PAu10-0.1 and PAu10-1

The identical procedure for static and photothermal heating experiments were also conducted on nanofilms containing Au NPs with different concentrations. However, fluorescence is quenched for higher temperatures ($T > 40$ °C) so it was not possible to collect the data at elevated temperatures. This is again a result of movements of polymer chains due to high temperature; consequent relocations and agglomerations of perylene molecules. Therefore, the distribution of the Au NPs is again nonuniform, some are more susceptible to quenching, some are more protected [201]; but still inadequate to display a reasonable spectra.

Both PAu10-0.1 and PAu10-1 samples were subjected to conventional heating and fluorescence spectrums were collected in every 5 °C, starting from 25 °C to 40 °C. Figure

7.6 displays static and laser heating results simultaneously. While y axis represents normalized trough to peak ratios; lower x axis (black) and upper x axis (red) stand for static heating in celcius degrees and irradiation in minutes respectively. This important point should be noted; both two experiments are independent of each other; just presented in the same chart for comparison.

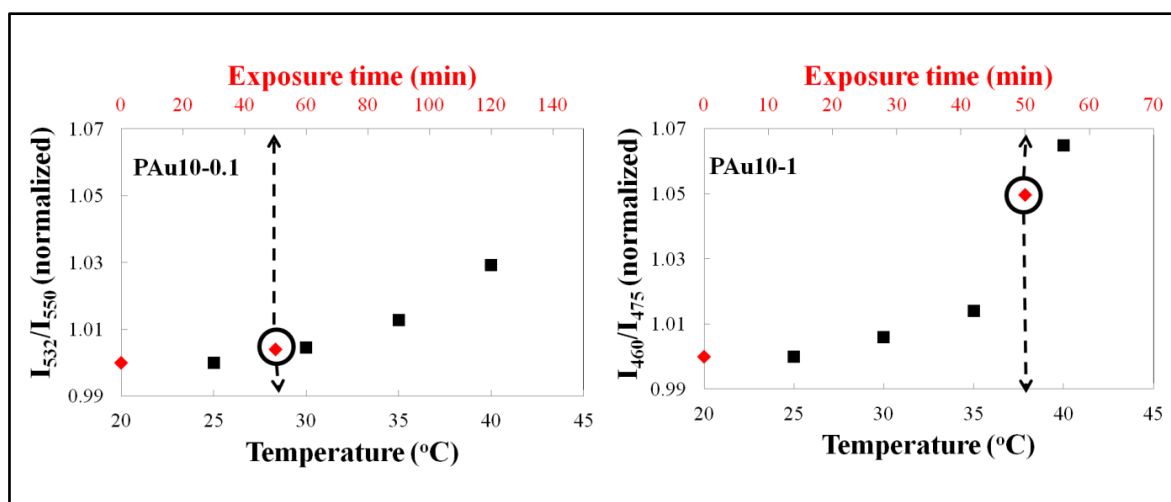


Figure 7.6. The conventional and photothermal heating of PAu10-0.1 and PAu10-1 nanofilms

The conventional heating data is shown with black squares in figure above. After heating of PAu10-0.1 nanofilm to 40 °C, the fluorescence ratio was found to increase 1.029 times than to those at 25 °C. This ratio was calculated as 1.065 for PAu10-1 and 1.020 for neat PEO. This is another indicator that presence of Au NPs triggers the changes in the spectra.

Same samples were then subjected to green light ($\lambda = 532$ nm) operating at 65 mW for 50 minutes. Before and after photothermal heating spectrums gave remarkable differences. With holding all the laser irradiation parameters same; i.e. exposure time, distance and power, fluorescence curves were plotted for nanofilms containing Au NPs both at 0.1 and 1 per cent (by wt). The fluorescence ratio was found to be 1.004 for PAu10-0.1 after 50 minutes of irradiation. Regarding the calibration curve for PAu10-0.1, 1.004 fits a place between 25-30 °C, implying that irradiation of Au NPs resulted temperature difference between 2-5 °C (encircled in chart at the left).

Increasing the Au NP concentration to tenth of its initial amount improved the heat caused by photothermal effect; the ratio reached 105 per cent of its initial value. Considering the calibration curve for PAu10-1, it is obvious that the temperature difference is higher. The final temperature (T_f) of the nanofilm is estimated at 37 - 40 °C. Since the calibration curves for the static heating of nanofilms do not perfectly fit the linear line equation, it would not be right to say the exact temperature that the films had reached implicitly. However, the effective heating of the nanofilms could also be experienced with naked hand contact.

The effective heating caused by photothermal effect via irradiation with light having a wavelength of 532 nm (which is spectrally equal to the SPR curve's maxima for Au NPs) was observed for nanofilms. While PEO films without Au NPs do not respond to green light, physical and spectral changes were observed for the ones having embedded Au NPs. As it was explained before, released heat is derived from the photo-excitation of surface electrons. The surface plasmon oscillation induces a strong absorption of light, as seen in the UV-vis spectrum (See Figure 2.8.b) The SPR condition is dependent of the particle size, shape, structure, the dielectric properties of the metal, or the surrounding medium, as these factors affect the electron charge density on the particle surface [81]. In the current work, the spherical gold nanoparticles with average diameter of 10 nm exhibit a SPR band maximum at 530 nm. Due to the SPR excitation, a light which is absorbed by gold nanoparticles is converted into thermal energy, which causes an elevation in temperature. In order to observe this temperature change in polymer film, a thermo responsive PEO / Au NPs nanofilm was prepared. Perylene molecules were randomly dispersed in the polymer matrix. The absorbed and reemitted fluorescence signals were collected and assumed to represent the average of the signals coming perylene molecules located at specific area that the light had hit. Since the light exposure area is calculated as 0.2 cm², roughly 1.77×10^{16} Au molecules are present in illumination area of PAu10-0.1, if the uniform distribution is assumed. The fluorescence signal is assumed to predominantly come from the adjacent perylene molecules to Au NPs.

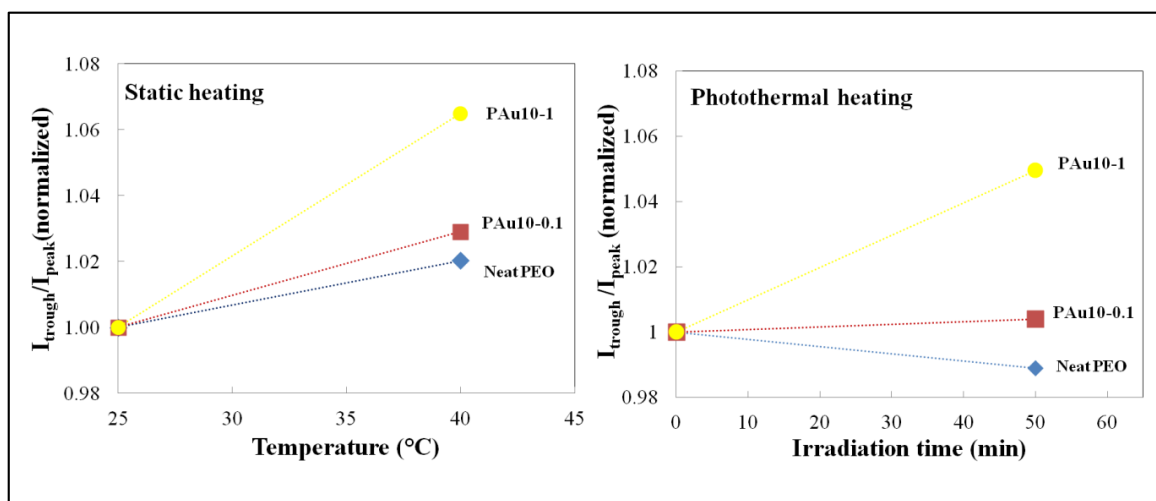


Figure 7.7. Fluorescence ratios for static and photothermal heating of neat PEO, PAu10-0.1 and PAu10-1

The amplitudes of 'trough' to 'peak' ratios were followed for each sample during static and photothermal heating procedures. The conventional heating of samples from 25 °C to 40 °C results an increase in fluorescence ratios as; 2.0 per cent for neat PEO, 2.9 per cent for PAu10-0.1 and 6.5 per cent for PAu10-1. Although the phase separation between nanofillers and polymer matrix is expected in high Au NP concentrations, PAu10-1 showed the maximum increase in fluorescence ratio at 40 °C. The Au NPs are responsible for conformational changes even in the presence of agglomerations.

On the other hand, irradiation of neat PEO, PAu10-0.1 and PAu10-1 samples with green light yielded differences in fluorescence spectra of samples. With keeping the laser intensity, exposure distance and duration constant, the effect of nanoparticle concentration on photothermal effect was investigated. The increments of fluorescence ratios were calculated as 0.4 per cent for PAu10-0.1 and 5 per cent for PAu10-1. The huge jump in fluorescence ratio for Au10-1 sample is a consequence of photo-excitation of greater extent of metal nanoparticles. The formed temperature difference between irradiation of PAu10-0.1 and PAu10-1 nanofilms is almost 10 °C.

7.5.2. Shape Memory Experiments

7.5.2.1. Activation of PDLLA/Magnetite Nanofilms with Heat

Pure PDLLA polymer does not present any shape memory property since there is no inductive heating of magnetic nanoparticles neither by magnetic nor photothermal effects [192]. Synthesized magnetite particles were dispersed in PDLLA matrix at various concentrations and each film were heated above its T_g and static heating experiment procedures were applied (See section 7.4.3.). Previously, glass transition temperature of PMag was determined at around 60-65 °C, whereas it was found at 50 °C for pure PDLLA via dynamic mechanical analyzer (DMA) experiments.

Our studies also confirmed PMag showed good shape memory properties while pure PDLLA does not exhibit any effect. Also the threshold concentration for was determined as 2.5 per cent (by wt). Nanocomposites with concentrations less than 2.5 per cent of magnetite did not show any shape memory properties. The schematic representation for the route followed during PMag shape memory experiments is given below;

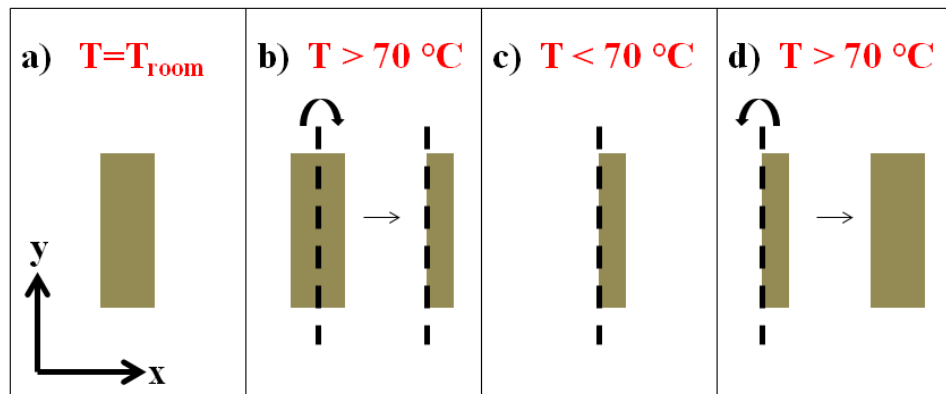


Figure 7.8. Shape memory behavior of PMag nanofilms

The PMag nanofilms are cut into rectangular shape. The permanent shape of the polymer at room temperature is shown in Figure 7.8.a. Then the films are heated above 70 °C and folded along the y axis that cuts the x axis from the middle. The folded piece in Figure 7.8.b. is heated below 70 °C in order to fix this temporary shape (Figure 7.8.c). Finally, the

folded piece is again heated above 70 °C and checked if the film turns back to its original shape in Figure 7.8.d. The recovery of the initial shape could not be provided for pure PDLLA, PMag nanofilms at 0.25, 0.5 and 1.25 % (by wt). Nevertheless, PMag2.5 and PMag5

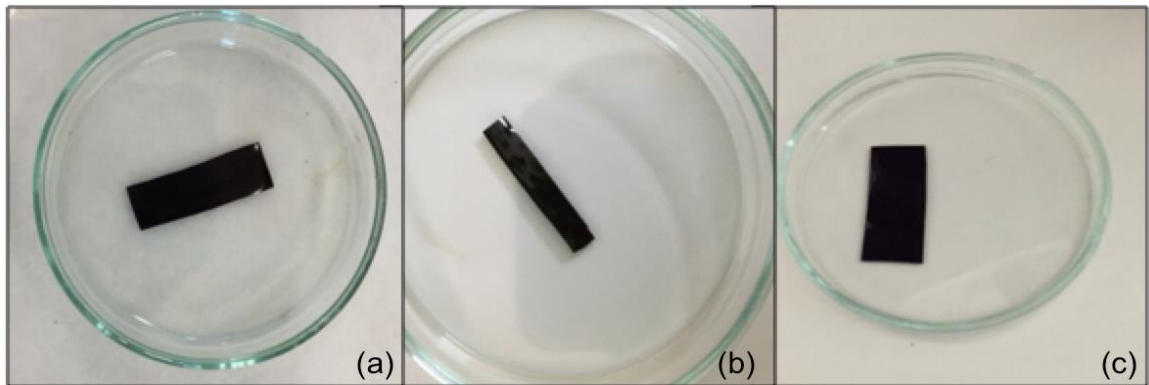


Figure 7.9. The process of shape memory recovery of PMag2.5;

- (a) Permanent shape of PMag2.5 at room temperature; (b) Folded shape of PMag2.5 at (b) $T < 70\text{ }^{\circ}\text{C}$; (c) PMag2.5 recovers its shape at $T > 70\text{ }^{\circ}\text{C}$

nanofilms successfully recovered their initial shapes, implying that the shape memory properties can be achieved via addition of magnetite nanoparticles to PDLLA after certain concentration, minimum 2.5 % by wt of magnetite in our case. Figure 7.9. and 7.10 show the shape recovery steps of PMag2.5 and PMag5 nanofilms while applying external heat.

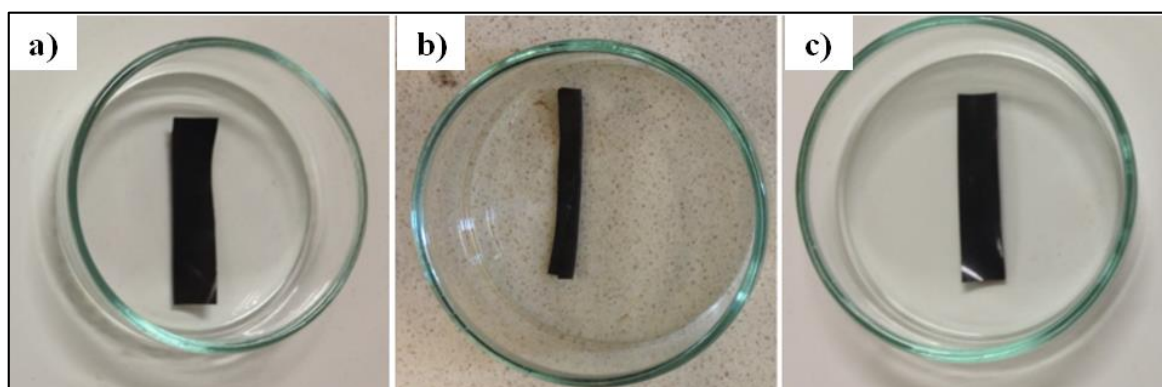


Figure 7.10. The process of shape memory recovery of PMag5;

- (a) Permanent shape of PMag5 at room temperature; (b) Folded shape of PMag5 at $T < 70\text{ }^{\circ}\text{C}$; (c) PMag5 recovers its shape at $T > 70\text{ }^{\circ}\text{C}$

7.5.2.2. Activation of PDLLA/Magnetite/Au Nanofilms with Laser Irradiation

The heating of polymer and subsequent recovery of initial shape is aimed via photothermal effect released from Au NPs in this part of the study. Several studies cover the shape memory effect caused by actuation of magnetite nanoparticles through magnetic field [189-192]. We aimed to improve shape memory properties by applying electromagnetic field on nanocomposites dispersed with metal nanoparticles. In this manner, it will be possible to control the properties by induction of both magnetic field and also light.

The addition of magnetite nanoparticles at concentration of 2.5 and 5 per cent (by wt) provides shape memory properties for PDLLA. With taking the shape memory advantage of magnetites, PMag5 nanofilm was used for photothermal experiments. Au NPs were used to trigger the thermal induction. Our previous studies (see section 7.5.1) showed that it is possible to heat the PEO matrix by external irradiation up to $10\text{ }^{\circ}\text{C}$. This was possible with adding 1 per cent (by wt) of Au NPs to PEO and shining the sample with green laser. Since the glass transition temperature of PMag nanofilms are recorded between $60\text{-}65\text{ }^{\circ}\text{C}$, it might not be possible to attain the temperature raise of $40\text{ }^{\circ}\text{C}$ (from room temperature to T_{trans}) considering the inevitable heat loss due to convection. So, PMag5 nanofilm doped with 5 per cent (by wt) of Au NPs (PMag5-Au5%) was heated up to $65\text{ }^{\circ}\text{C}$ conventionally and subjected to laser light after this temperature (See Figure 7.11).

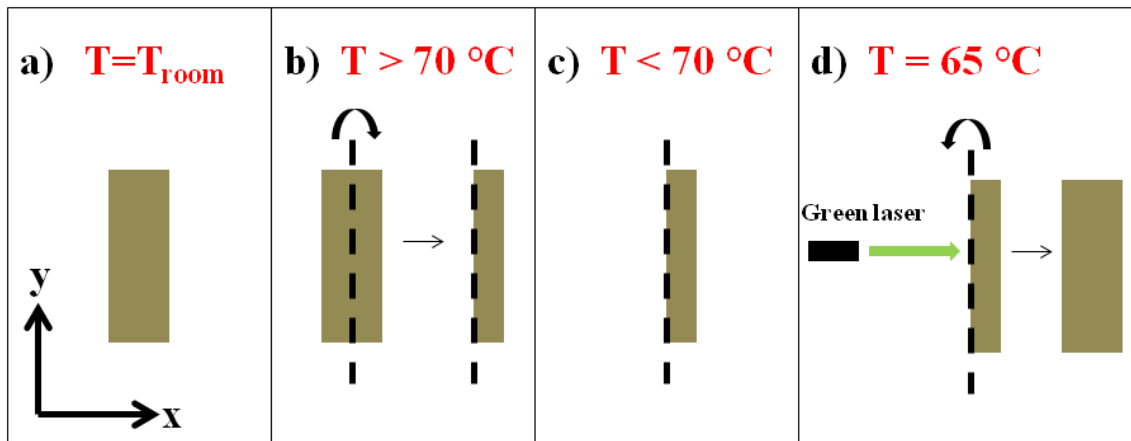


Figure 7.11. Shape memory behavior of PMag5-Au5% irradiated with green laser

After applying external stress (folding) and cooling the PMag5-Au5% below T_g , the nanofilm was heated to 65 °C to check if the shape recovery will be possible under T_{trans} . However, PMag5-Au5% did not recover its original shape at that temperature. So, laser irradiation was applied to heat the sample using heat caused by photothermal effect. Shining PMag5-Au5% sample with green light which has a wavelength of 532 nm for 30 minutes enabled the film turn back to its original shape. It can be concluded that the irradiation of PMag5-Au% nanofilm for 30 minutes lead to a temperature increase of a minimum of 5 °C resulting in the shape recovery of the shape memory nanocomposites.

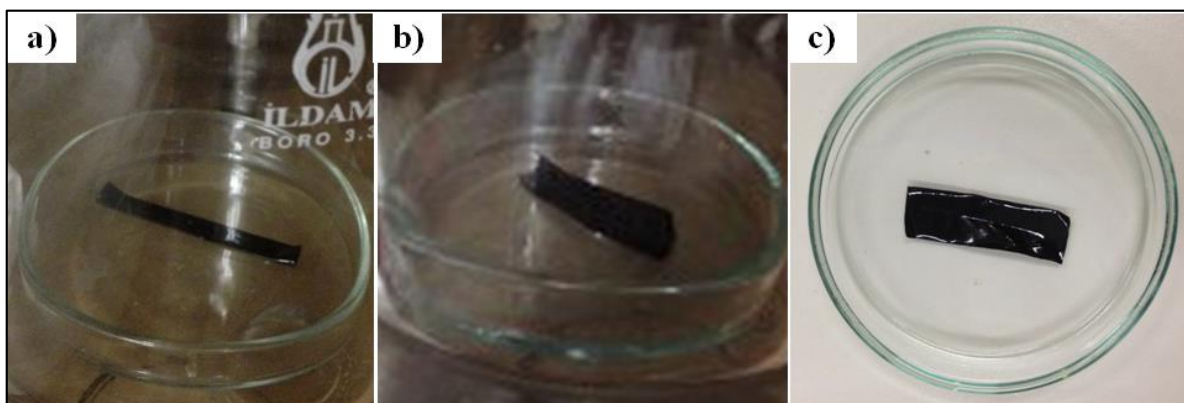


Figure 7.12. The process of shape memory recovery of PMag5-Au5%; (a) Folded shape of PMag5-Au5% at $T < 70\text{ }^{\circ}\text{C}$; (b) PMag5-Au5% could not recover its shape at $65\text{ }^{\circ}\text{C}$; (c) Shape recovery completed after 30 min of irradiation at $65\text{ }^{\circ}\text{C}$

7.6. CONCLUSION

Photothermal effect of nanoparticles dispersed in polymer matrix and the use of subsequent heat released for shape memory applications were studied in this chapter. The ability of some polymers to respond to heat or light is a significant scientific and technological phenomenon and allows a new class materials emerge as shape memory polymers. In this work, experiments on photothermal effect released by irradiation of Au10/o NPs in PEO were performed and resulting temperature change was monitored via fluorescence spectroscopy. With using the surface plasmon resonance of Au10/o NPs, the activation of shape memory polymers was then demonstrated.

Au10/o NPs in PEO (with concentration of 0.1 and 1 per cent, by wt) and perylene molecules were used as nanoactuators and fluorophores respectively. The fluorescence spectra of Au10/o and perylene added PEO gave some specific peaks and troughs. Fluorescence intensities of these specific peaks were followed during static and photothermal heating of polymer. The green laser used in the study has a wavelength of 532 nm and operating power of 65 mW. The static heating of samples from $25\text{ }^{\circ}\text{C}$ to $40\text{ }^{\circ}\text{C}$ result an increase in fluorescence ratios of 2.0, 2.9 and 6.5 per cent for neat PEO, PAu10-0.1 and PAu10-1 respectively. While laser irradiation of PAu10-0.1 and PAu10-1 samples for 50 minutes makes an enhancement in fluorescence ratio of 0.4 and 5 per cent, any

significant change was not observed for neat PEO. Whereas the temperature of the Au doped films increase due to photothermal heating, fluorescence light has no remarkable effect on neat polymer spectra. 2-5 °C of increase was achieved with shining Au10/o NPs in PEO with concentration of 0.1 per cent (by wt) and the difference in temperature was found around 12-15 °C for nanofilms having 1 per cent (by wt) of Au10/o; the higher nanofiller content results increase in heat released due to photothermal effect.

It was known and also confirmed via experiments that poly (DL-lactide-co-glycolide) (PDLLA) does not exhibit shape memory properties. So, magnetite nanoparticles having a diameter of 6-12 nm were added to PDLLA at various amounts and nanofilms were tested whether they recover their original shape after heating above T_{trans} . PDLLA films which have magnetite concentration of 2.5 and 5 per cent (by wt) was found to display shape memory effect, therefore the photothermal experiments were carried out on PDLLA sample doped with magnetite nanoparticles at 5 per cent (by wt), which are named as PMag5. Shape recovery of PMag5 was demonstrated by both static and photothermal heating. Exposure of green light on PMag5-Au5% for 30 minutes made the sample recover its original shape successfully.

The photothermal heating was demonstrated with addition of Au10/o NPs to polymers even at concentration of 0.1 per cent (by wt). Releasing heat can be altered via changing the NP content and concentration. As a future work, other parameters influence the photothermal effect will be investigated. And also the shape memory effect of PMag nanocomposites will be supported with numerical analysis using fluorescence spectrophotometric methods.

8. CONCLUDING REMARKS

The ultimate goal of this work is to actuate shape memory polymers via using photothermal effect caused by metal nanoparticles. Gold and magnetic nanoparticles were simultaneously dispersed in poly (DL-lactide-co-glycolide) matrix where remote actuation of the nanocomposite was achieved by laser irradiation of dispersed gold nanoparticles and the presence of magnetite was responsible for the shape memory behavior of the polymer that otherwise does not exhibit this property. The stimuli response of this particular polymer could have been achieved by magnetic field, but we presented a light induced model in this work. However, dual actuation can be possible in further studies. The photothermal effect of gold nanoparticles on poly (ethylene oxide) was also investigated with using fluorescence probes as thermal sensors. It was found that the local temperature of PEO can be varied with shining the gold nanoparticles with green light and this change can be tracked via fluorescence spectrophotometer. The method used to infer changes in crystallinity in PEO was demonstrated using Raman peaks. This method enabled us to monitor molecular events, in situ. Also, characterization, mechanical and thermal experiments were performed on PEO nanofilms. Gold and silver nanoparticles with average diameter of 10 and 30 nm were shown to display homogeneous dispersion in PEO matrix, however the agglomerations are inevitable above a threshold concentration. The phase separation between polymer and nanoparticles enables the mechanical properties of polymers enhance only up to a certain point. The influence of silver nanoparticles on thermal conductivity of base fluids was also investigated. The effective thermal conductivity of hexane and ethylene glycol was found to increase with addition of silver nanoparticles, however the deterioration was recorded for water. Silver nanoparticles can be used to improve heat transfer using ethylene glycol and hexane, but cannot be proposed for water. As a conclusion, gold and silver nanoparticles are proposed to be used as nano-tracers and besides that enhance the thermal and mechanical properties of final product.

REFERENCES

1. M. Cartwright, “Gold in Antiquity, Ancient History Encyclopedia”, <http://www.ancient.eu/gold/> [retrieved 4 April 2014].
2. F. Antonii, *Panacea Aurea-Auro Potabile; Bibliopolio Frobeniano*, Hamburg, 1618.
3. M. Faraday, The Bakerian Lecture: Experimental Relations of Gold (and Other Metals) to Light, *Philosophical Transactions of the Royal Society*, 147:145-181, 1857.
4. T. P. Sau and A. L. Rogach, Colloidal Synthesis of Noble Metal Nanoparticles of Complex Morphologies, In: T. G. Sau and A. L. Rogach, editors, *Complex Shaped Metal Nanoparticles*, Wiley, 2012.
5. R. C. Birtcher, S. E. Donnelly and S. Schlutig, Nanoparticle Ejection from Gold During Ion Irradiation, *Nuclear Instruments and Methods in Physics Research Section B*, 215:69–75, 2004.
6. J. K. Lung, J. C. Huang, D. C. Tien, C. Y. Liao, K. H. Tseng, T. T. Tsung, W. S. Kao, T. H. Tsai, C. S. Jwo, H. M. Lin and L. Stobinski, Preparation of Gold Nanoparticles by Arc Discharge in Water, *Journal of Alloys and Compounds*, 434:655–658, 2007.
7. V. Amendola, M. Meneghetti, G. Granozzi, S. Agnoli, S. Polizzi, P. Riello, A. Boscaini, C. Anselmi, G. Fracasso, M. Colombatti, C. Innocenti, D. Gatteschi and C. Sangregorio, Top-down Synthesis of Multifunctional Iron Oxide Nanoparticles for Macrophage labelling and manipulation, *Journal of Materials Chemistry*, 21:3803, 2011.
8. D. T. Nguyen, D. Kim and K. Kim, Review: Controlled Synthesis and Biomolecular Probe Application of Gold Nanoparticles, *Micron*, 42:207-227, 2011.

9. J. Turkevitch, P. C. Stevenson and J. Hillier, Nucleation and Growth Process in the Synthesis of Colloidal Gold, *Discussions of the Faraday Society*, 11:55-75, 1951.
10. G. Frens, Controlled Nucleation for the Regulation of the Particle Size in Monodisperse Gold Suspensions, *Nature*, 241:20-22, 1973.
11. M. Brust, M. Walker, D. Bethell, D. J. Schiffrin and R. Whyman, Synthesis of Thiol Derivatized Gold Nanoparticles in a 2-phase Liquid-Liquid system, *Journal of the Chemical Society, Chemical Communications*, pp. 801–802, 1994.
12. N. R. Jana, L. Gearheart and C. J. Murphy, Evidence for Seed-Mediated Nucleation in Chemical Reduction of Gold Salts to Gold Nanoparticles, *Chemistry of Materials*, 13:2313–2322, 2001.
13. J. A. Dahl, B. L. S. Maddux and J. E. Hutchison, Toward Greener Synthesis, *Chemical Reviews*, 107:2228-2269, 2007.
14. P. Anastas and J. Warner, *Green Chemistry: Theory and Practice*; Oxford University Press: New York, 1998.
15. I. Medina-Ramirez, S. Bashir, Z. Luo and J. L. Liu, Green Synthesis and Characterization of Polymer-Stabilized Silver Nanoparticles, *Colloids and Surfaces B: Biointerfaces*, 73:185-191, 2009.
16. S. D. Salomon, M. Bahadory, A. V. Jeyarajasingam, S. A. Rutkowsky, C. Boritz and L. Mulfinger, Synthesis and Study of Silver Nanoparticles, *Journal of Chemical Education*, 84:322-325, 2007.
17. H. Hiramatsu and F. Osterloh, A Simple Large Scale Synthesis of Nearly Monodisperse Gold and Silver Nanoparticles with Adjustable Sizes and with Exchangeable Surfactants, *Chemistry of Materials*, 16:2509-2511, 2004.

18. X. Liu, M. Atwater, J. Wang, Q. Dai, J. Zou, J. Brennan and Q. Huo, A Study on Gold Nanoparticle Synthesis Using Oleylamine as Both Reducing Agent and Protecting Ligand, *Journal of Nanoscience and Nanotechnology*, 7:3126-3133, 2007.
19. M. Abramoff, P. Magelhaes and S. Ram, Image Processing with ImageJ, *Biophotonics International*, 11:36-42, 2004.
20. N. K. Sahu, A. Prakash and D. Bahadur, Ce³⁺ Sensitized GdPO₄:Tb³⁺ with Iron Oxide Nanoparticles: a Potential Biphasic System for Cancer Theranostics, *Dalton Transactions*, 43:4892, 2014.
21. X. W. Wu, C. Liu, L. Li, P. Jones, R. W. Chantrell and D. Weller, Nonmagnetic Shell in Surfactant-Coated FePt Nanoparticles, *Journal of Applied Physics*, 95:6810, 2004.
22. Z. Xu, C. Shen, H. Yanglong, G. Hongjun and S. Sun, Oleylamine as Both Reducing Agent and Stabilizer in a Facile Synthesis of Magnetite Nanoparticles, *Chemistry of Materials*, 21:1778-1780, 2009.
23. W. K. Lewis, A. T. Rosenberger, J. R. Gord, C. A. Crouse, B. A. Harruff, K. A. S. Fernando, M. J. Smith, D. K. Phelps, J. E. Spowart, E. A. Guliants and C. E. Bunker, Multispectroscopic (FTIR, XPS, and TOFMS-TPD) Investigation of the Core-Shell Bonding in Sonochemically Prepared Aluminum Nanoparticles Capped with Oleic Acid, *Journal of Chemical Physics C*, 114:6377, 2010.
24. B. M. Da Conceição, M. A. S. Costa, C. Luiz, S. M. De, M. R. Silva and S. H. Wang, A Study of the Initiator Concentration's Effect on Styrene-Divinylbenzene Polymerization with Iron Particles, *Polímeros: Ciência e Tecnologia*, 21:5, 2011.
25. P. Roonasi and A. Holmgren, A Fourier Transform Infrared (FTIR) and Thermogravimetric Analysis (TGA) Study of Oleate Adsorbed on Magnetite Nanoparticle Surface, *Applied Surface Science*, 255:5891-5895, 2009.

26. W. Haiss, N. T. K. Thanh, J. Aveyard and D. G. Fernig, Determination of Size and Concentration of Gold Nanoparticles from UV-Vis Spectra, *Analytical Chemistry*, 79:4215-4221, 2007.
27. C. Sanchez, B. Julián, P. Belleville and M. Popall, Applications of Hybrid Organic-Inorganic Nanocomposites. *Journal of Materials Chemistry*, 15:3559-3592, 2005.
28. C. Sanchez, H. Arribart and M. M. Giraud Guille, Biomimetism and Bioinspiration as Tools for the Design of Innovative Materials and Systems, *Nature Materials*, 4:277-288, 2005.
29. B. K. G. Theng, *Formation and Properties of Clay Polymer Complexes*, Elsevier, NY, 1979.
30. A. R. Payne, Effect of Dispersion on the Dynamic Properties of Filler-Loaded Rubbers, *Journal of Applied Polymer Science*, 9:2273-2284, 1965.
31. A. A. Gusev, Micromechanical Mechanism of Reinforcement and Losses in Filled Rubbers, *Macromolecules*, 39:5960-5962, 2006.
32. A. R. Payne, A Note on the Conductivity and Modulus of Carbon Black-Loaded Rubbers, *Journal of Applied Polymer Science*, 9:1073-1082, 1965.
33. Z. Ounaiesa, C. Park, K. E. Wiseb, E. J. Siochic and J. S. Harrison, Electrical Properties of Single Wall Carbon Nanotube Reinforced Polyimide Composites, *Composites Science and Technology*, 63:1637-1646, 2003.
34. R. Udayabhaskar, R. V. Mangalaraja, D. Manikandan, V. Arjunan and B. Karthikeyan, Room Temperature Synthesis and Optical Studies on Ag and Au Mixed Nanocomposite Polyvinylpyrrolidone Polymer Films, *Spectrochimica Acta Part A: Molecular and Biomolecular Spectroscopy*, 99:69-73, 2012.

35. A. Okada and A. Usuki, Twenty Years of Polymer-Clay Nanocomposites, *Macromolecular Materials and Engineering*, 291:1449-1476, 2006.
36. M. Böhning, H. Goering, N. Hao, R. Mach and A. Schönhals, Polycarbonate/SiC Nanocomposites-Influence of Nanoparticle Dispersion on Molecular Mobility and Gas Transport, *Polymers for Advanced Technologies*, 16:262-268, 2005.
37. Q. Zhang, Investigating Polymer Conformation in Poly (Ethylene Oxide) (PEO) Based Systems for Pharmaceutical Applications, Chalmers University of Technology, Department of Applied Physics, MSc. Thesis, Sweden, 2011.
38. C. J. Van Oss and R. F. Giese, On the Structure of Poly-(Ethylene Oxide) When Immersed in Water, *Journal of Dispersion Science and Technology*, 31:1697, 2010.
39. S. Ibrahim and M. R. Johan, Thermolysis and Conductivity Studies of Poly (Ethylene Oxide) (PEO) Based Polymer Electrolytes Doped with Carbon Nanotube, *International Journal of Electrochemical Science*, 7:2596 – 2615, 2012.
40. G. B. Appetecchi, M. Montanino, A. Balducci, S. F. Lux, M. Winterb and S. Passerini, Lithium Insertion in Graphite From Ternary Ionic Liquid-Lithium Salt Electrolytes: I. Electrochemical Characterization of the Electrolytes, *Journal of Power Sources*, 193: 599-605, 2009.
41. H. M. Azeredo and M. C. Henriette, Nanocomposites for Food Packaging Applications, *Food Research International*, 42:1240-1253, 2009.
42. J. M. Garcés, D. J. Moll, J. Bicerano, R. Fibiger and D. G. McLeod, Polymeric Nanocomposites for Automotive Applications, *Advanced Materials*, 12:3, 2000.
43. I. Brigger, C. Dubernet and P. Couvreur, Nanoparticles in Cancer Therapy and Diagnosis, *Advanced Drug Delivery Reviews*, 54:631-651, 2002.

44. J. Panyam and V. Labhasetwar, Biodegradable Nanoparticle from Drug and Gene Delivery to Cells and Tissue, *Advanced Drug Delivery Reviews*, 55:329-347, 2003.
45. Z. Cui and R. J. Mumper, Plasmid DNA-Entrapped Nanoparticles Engineered from Microemulsion Precursors: In Vitro and In Vivo Evaluation, *Bioconjugate Chemistry*, 13:1319-1327, 2002.
46. X. Cao, S. Lai and L. J. Lee, Design of a Self-Regulated Drug Delivery Device, *Biomedical Micro Devices*, 3:109-118, 2001.
47. D. Arzhakov, A. Artemenko, I. Gordeev, A. Choukourov, D. Slavinska, D. and H. Biederman, Nanocomposite Metal/Poly (Ethylene Oxide)-like Plasma Polymer Films and Their Properties, *WDS'10 Proceedings of Contributed Papers: Part III, Proceedings of the 19th Annual Conference of Doctoral Students*, Prague, 19–24, 2010.
48. B. H. Xu, B. Z. Lin, D. Y. Sun and C. Ding, Preparation and Electrical Conductivity of Polyethers/WS₂ Layered Nanocomposites, *Electrochimica Acta*, 52:3028-3034, 2007
49. D. Papahadjopoulos, T. M. Allen, A. Gabizon, E. Mayhew, K. Matthay, S. K. Huang, K. D. Lee, M. C. Woodle, D. D. Lasic, C. Redemann and F. J. Martin, Sterically Stabilized Liposomes: Improvements in Pharmacokinetics and Antitumor Therapeutic Efficacy, *Proceedings of National Academy of Sciences*, 88:11460, 1991.
50. L. M. Graham, Pegasparaginase: A Review of Clinical Studies. *Advanced Drug Delivery Reviews*, 55:1293–1302, 2003.
51. Y. Levy, M. S. Hershfield, C. Fernandez-Mejia, S. H. Polmar, D. Scudiero, M. Berger and R. U. Sorensen, Adenosine Deaminase Deficiency with Late Onset or Recurrent Infections: Response to Treatment with Polyethylene Glycol Modified Adenosine Deaminase, *Journal of Pediatrics*, 113:312–317, 1988.

52. P. Bailon, A. Palleroni, C. A. Schaffer, C. L. Spence, W. J. Fung, J. E. Porter, G. K. Ehrlich, W. Pan, Z. X. Xu, M. W. Modi, A. Farid, W. Berthold and M. Graves, Rational Design of a Potent, Long Lasting Form of Interferon: a 40kDa Branched Poly-Ethylene Glycol-Conjugated Interferon Alpha-2a for the Treatment of Hepatitis C., *Bioconjugate Chemistry*, 12:195–202, 2001.
53. Y.S. Wang, S. Youngster, M. Grace, J. Bausch, R. Bordens and D. F. Wyss, Structural and Biological Characterization of Pegylated Recombinant Interferon α -2b and Its Therapeutic Implications, *Advanced Drug Delivery Reviews*, 54:547–570, 2002.
54. B. Maggio, Q. F. Ahkong and J. A. Lucy, Polyethylene Glycol, Surface Potential and Cell Fusion, *Biochemical Journal*, 158:647, 1976.
55. C. Toniolo, G. M. Bonora, M. Mutter and F. Maser, Self-Association and Solubility of Peptides. An Infra-red Absorption Method for Quantitative Titration of the Extent of Self-Association in Poly(ethylene glycol)-Bound Peptides, *Journal of Chemistry Society, Chemical Communications*, 9:1298, 1983.
56. G. Johansson and F. Tjerneld, In: G. Street, editor, *Highly Selective Separations in Biotechnology*, pp. 55–85, Blackie Academic & Professional, London, 1994.
57. M. Lu, P. A. Albertsson, G. Johansson and F. Tjerneld, Ucon/benzoyl Dextran Aqueous Two-Phase Systems: Protein Purification with Phase Component Recycling, *Journal of Chromatography B*, 680:65–70, 1996.
58. S. J. Higgins, Conjugated Polymers Incorporating Pendant Functional Groups - Synthesis and Characterization, *Chemical Society Reviews*, 26:247-257, 1997.
59. S. A. Ashraf, F. Chen, C. O. Too and G. G. Wallace, Bulk Electropolymerization of Alkylpyrroles, *Polymer*, 37:2811, 1996.

60. J. K. Kim and H. Ahn, Fabrication and Characterization of Polystyrene/Gold Nanoparticle Composite Nanofibers, *Macromolecular Research*, 16:163-168, 2008.
61. C. Pandis, E. Logakis, A. Kyritsis, P. Pissis, V. V. Vodnik, E. Dzunuzovic, J. M. Nedeljkovic, V. Djokovic, J. C. Rodriguez Hernandez and J. L. Gomez Ribelles, Glass Transition and Polymer Dynamics in Silver/poly(methyl methacrylate) Nanocomposites, *European Polymer Journal*, 47:1514–1525, 2011.
62. R. Montazami, C. Spillmann, J. Naciri and B. Ratna, Enhanced Thermomechanical Properties of a Nematic Liquid Crystal Elastomer Doped with Gold Nanoparticles, *Sensors and Actuators A: Physical*, 178:175, 2012.
63. M. Z. Rong, M. Q. Zhang, Y. X. Zheng, H. M. Zeng, R. Walter and K. Friedrich, Structure–Property Relationships of Irradiation Grafted Nano-Inorganic Particle Filled Polypropylene Composites, *Polymer*, 42:167–183, 2001.
64. T. Hanemann and D. V. Szabó, Polymer-Nanoparticle Composites: From Synthesis to Modern Applications, *Materials*, 3:3468-3517, 2010.
65. B. M. Novak, Hybrid Nanocomposite Materials-Between Inorganic Glasses and Organic Polymers, *Advanced Materials*, 5:422-433, 1993.
66. E. P. Giannelis, Polymer Layered Silicate Nanocomposites, *Advanced Materials*, 8:29-35, 1996.
67. M. A. Osman, J. E. P. Rupp and U. W. Suter, Effect of Non-Ionic Surfactants on the Exfoliation and Properties of Polyethylene-Layered Silicate Nanocomposites. *Polymer*, 46:8202-8209, 2010
68. A. C. Balazs, T. Emrick and T. P. Russell, Nanoparticle Polymer Composites: Where Two Small Worlds Meet, *Science*, 314:1707-1710, 2006.
69. R. A. Vaia and E. P. Giannelis, Lattice of Polymer Melt Intercalation In Organically Modified Layered Silicates, *Macromolecules*, 30:7990-7999, 1997.

70. R. A. Vaia and E. P. Giannelis, Polymer Melt Intercalation in Organically Modified Layered Silicates: Model Predictions and Experiment, *Macromolecules*, 30:8000-8009, 1997.
71. S. Li, M. M. Lin, M. S. Toprak, D. K. Kim and M. Muhammed, Nanocomposites of Polymer and Inorganic Nanoparticles for Optical and Magnetic Applications, *Nano Reviews*, 1:5214, 2010.
72. P. H. C. Camargo, K. G. Satyanarayana and F. Wypych, Nanocomposites: Synthesis, Structure, Properties and New Application Opportunities, *Materials Research*, 12:1-39, 2009.
73. K. Sooklal, L. H. Hanus, H. J. Ploehn and C. J. Murphy, A Blue-Emitting CdS/dendrimer Nanocomposite, *Advanced Materials*, 10:1083, 1998.
74. G. Jimenez, N. Ogata, H. Kawai and T. Ogihara, Structure and Thermal/mechanical Properties of Poly (ϵ -caprolactone) - Clay Blend, *Journal of Applied Polymer Science*, 64:2211-2220, 1997.
75. N. Ogata, G. Jimenez, H. Kawai, T. Ogihara and N. Ogata, Structure and Thermal/Mechanical Properties of Poly (l-lactide) - Clay Blend, *Journal of Polymer Science Part B: Polymer Physics*, 35:389-396, 1997.
76. H. Althues, J. Henle and S. Kaskel, Functional Inorganic Nanofillers for Transparent Polymers, *Chemical Society Reviews*, 36:1454, 2007.
77. M. Avella, M. W. Errico and E. Martuscelli, Novel PMMA/CaCO₃ Nanocomposites Abrasion Resistant Prepared by an In Situ Polymerization Process, *Nano Letters*, 1:213-217, 2001.
78. E. Bourgeat-Lami, Organic-Inorganic Nanostructured Colloids, *Journal of Nanoscience and Nanotechnology*, 2:1-24, 2002.

79. C. Lü, Y. Cheng, Y. Liu, F. Liu and B. Yang, A Facile Route to ZnS–Polymer Nanocomposite Optical Materials with High Nanophase Content via γ -Ray Irradiation Initiated Bulk Polymerization, *Advanced Materials*, 18:1188–1192, 2006.
80. M. M. Alvarez, J. T. Khoury, T. G. Schaaff, M. N. Shafigullin, I. Vezmar and R. L. Whetten, Optical Absorption Spectra of Nanocrystal Gold Molecules, *The Journal of Physical Chemistry B*, 101:3706-3712, 1997.
81. G. E. Yun and K. A. N. G. Bin, Surface Plasmon Resonance Scattering and Absorption of Biofunctionalized Gold Nanoparticles for Targeted Cancer Imaging and Laser Therapy, *Science China Technological Sciences*, 54:2358-2362, 2011.
82. Bucak, S. and D. Rende, *Colloid and Surface Chemistry: A Laboratory Guide for Exploration of the Nano World*, Baco Raton: CRC Press, 2013.
83. D. Ratna, T. N. Abraham and J. Karger-Kocsis, Studies on Polyethylene Oxide and Phenolic Resin Blends, *Journal of Applied Polymer Science*, 108:2156–2162, 2008.
84. Y. Long and R. A. Shanks, PP-elastomer–filler hybrids. I. Processing, Microstructure, and Mechanical Properties, *Journal of Applied Polymer Science*, 61:1877-1885, 1996.
85. Z. Bartczak, A. S. Argona, R. E. Cohena and M. Weinberg, Toughness Mechanism In Semi-Crystalline Polymer blends: II. High-density Polyethylene Toughened with Calcium Carbonate Filler Particles, *Polymer*, 40:2347–2365, 1999.
86. R. K. D. Misra, P. Nerikar, K. Bertrand and D. Murphy, Some Aspects of Surface Deformation and Fracture of 5-20 % Calcium Carbonate-Reinforced Polyethylene Composites, *Material Science and Engineering: A*, 384:284, 2004.
87. S. Tjong, Structural and Mechanical Properties of Polymer Nanocomposites, *Materials Science and Engineering: R: Reports*, 53:73-197, 2006.

88. A. G. El-Shamy, W. Attia and K. M. Abd El-Kader, The Optical and Mechanical Properties of PVA-Ag Nanocomposite Films, *Journal of Alloys and Componds*, 590: 309–312, 2014.
89. Y. Sun, Z. Zhang, K. S. Moon and C. P. Wong, Glass Transition and Relaxation Behavior of Epoxy Nanocomposites, *Journal of Polymer Science Part B: Polymer Physics*, 42:3849-3858, 2004.
90. A. Feyzi, K. Faghihi, A. Raesi, M. Koushki and M. Farahani, New Optically Active Organo-Soluble Poly(amide-imide)s from [N,N'-(4,4'-diphtaloyl)-bis-l-amino diacid]s and 1,2-bis[4,4'-aminophenoxy] Ethane: Synthesis and Characterization, *Journal of Chilean Chemical Society*, 58,2013.
91. W. D. Callister and D. G. Rethwisch, *Materials Science and Engineering, An Introduction*, 8th Edition, John Wiley & Sons, Inc., 2007.
92. J. J. Aklonis, Mechanical Properties of Polymers, *Journal of Chemical Education*, 58:892, 1981.
93. J. R. Fried, *Polymer Science & Technology*, 2nd Edition, Pearson Education, Inc., Prentice Hall, 2003.
94. J. R. Fried, S. Y. Lai, L. W. Kleiner and M. E. Wheeler, Experimental Assessment of the Thermodynamic Theory of the Compositional Variation of T_g : PVC systems, *Journal of Applied Polymer Science*, 27:2869, 1982.
95. N. G. McCrum, C. P. Buckley and C. B. Bucknall, *Principles of Polymer Engineering*, 2nd Edition, Oxford University Press, Oxford, 1997.
96. T. Murayama, *Dynamic Mechanical Analysis of Polymeric Material*, Elsevier, Amsterdam, 1978.

97. K. Menard, *Dynamic Mechanical Analysis: A Practical Introduction*, 2nd Edition, CRC Press, Florida, 2008.
98. B. Wunderlich, *Macromolecular Physics, Vol. 1*, Academic Press, New York, 1973.
99. G. R. Strobl, *The Physics of Polymers: Concepts for Understanding Their Structures and Behavior*, 3rd Edition, Springer, 2007.
100. C. Branca, S. Magazu, G. Maisano, F. Migliardo and G. Romeo, Study of Conformational Properties of Poly (Ethylene Oxide) by SANS and PCS Techniques, *Physica Scripta*, 67:551-554, 2003.
101. P. Rittigstein and J. M. Torkelson, Polymer–Nanoparticle Interfacial Interactions in Polymer Nanocomposites: Confinement Effects on Glass Transition Temperature and Suppression of Physical Aging, *Journal of Polymer Science: Part B: Polymer Physics*, 44:2935–2943, 2006.
102. S. U. S. Choi and J. A. Eastman, Enhancing Thermal Conductivity of Fluids with Nanoparticles, *ASME International Mechanical Engineering Congress & Exposition*, San Francisco, CA, 1995.
103. J. C. Maxwell, *A Treatise on Electricity and Magnetism*, Clarendon Press, 2nd Edition, Oxford, UK, 1881.
104. X. Wang and A. S. Mujumdar, Heat Transfer Characteristics of Nanofluids: A Review, *International Journal of Thermal Sciences*, 46:1–19, 2007.
105. G. K. Batchelor and R. W. O'Brien, Thermal or Electrical Conduction Through a Granular Material, *Proceedings of the Royal Society of London*, A355:313-333, 1977.
106. R. L. Hamilton and O. K. Crasser, Thermal Conductivity of Heterogeneous Two-Component Systems, *Industrial & Engineering Chemistry Fundamentals*, 1:187-191, 1962.

107. M. P. Beck, Y. Yuan, P. Warriar and A. S. Teja, The Effect of Particle Size on the Thermal Conductivity of Alumina Nanofluids, *Journal of Nanoparticle Research*, 11:1129-1136, 2009.
108. H. E. Patel, S. K. Das, T. Sundararajan, A. S. Nair, B. George and T. Pradeep, Thermal Conductivity of Naked and Monolayer Protected Metal Nanoparticles Based Nanofluids: Manifestation of Anomalous Enhancement and Chemical Effects, *Applied Physics Letters*, 8:2931, 2003.
109. V. Iranidokht, S. Hamian, N. Mohammadi and M. B. Shafii, Thermal Conductivity of Mixed Nanofluids Under Controlled pH Conditions, *International Journal of Thermal Sciences*, 74:63-71, 2013.
110. D. Wu, H. Zhu, L. Wang and L. Liu, Critical Issues in Nanofluids Preparation, Characterization and Thermal Conductivity, *Current Nanoscience*, 5:103-112, 2009.
111. I. Palabiyik, Z. Musina, S. Witharana and Y. Ding, Dispersion Stability and Thermal Conductivity of Propylene Glycol Based Nanofluids, *Journal of Nanoparticle Research*, 13:5049, 2011.
112. N. Shalkevich, W. Escher, T. Bürgi, B. Michel, L. Si-Ahmed and D. Poulikakos, On the Thermal Conductivity of Gold Nanoparticle Colloids, *Langmuir*, 26:663–670, 2010.
113. R. K. Sahu, S. H. Somashekhar and P. V. Manivannan, Investigation on Copper Nanofluid obtained through Micro Electrical Discharge Machining for Dispersion Stability and Thermal Conductivity, *Procedia Engineering*, 64:946-955, 2013.
114. H. Zhu, D. Han, Z. Meng, D. Wu and C. Zhang, Preparation and Thermal Conductivity of CuO Nanofluid via a Wet Chemical Method, *Nanoscale Research Letters*, 6:181, 2011.

115. X. Wang, X. Xu and S. U. S. Choi, Thermal Conductivity of Nanoparticle–Fluid Mixture, *Journal of Thermophysics and Heat Transfer*, 13:474– 480, 1999.
116. T. Teng, Thermal Conductivity and Phase-Change Properties of Aqueous Alumina Nanofluid, *Energy Conversion and Management*, 67:369–375, 2013.
117. J. M. Salehi, M. M. Heyhat and A. Rajabpour, Enhancement of Thermal Conductivity of Silver Nanofluid Synthesized by a One-Step Method with the Effect of Polyvinylpyrrolidone on Thermal Behavior, *Applied Physics Letters*, 102:231907, 2013.
118. J. M. Romano, J. C. Parker and Q. B. Ford, Application Opportunities for Nanoparticles Made from Condensation of Physical Vapors, *Advanced Powder Metallurgy Particulate Materials*, 2:12-13, 1997.
119. T. Cho, I. Baek, J. Lee and S. Park, Preparation of Nanofluids Containing Suspended Silver Particles for Enhancing Fluid Thermal Conductivity of Fluids, *Journal of Industrial and Engineering Chemistry*, 11:400-406, 2005.
120. S. P. Jang and S. U. S. Choi, Role of Brownian Motion in the Enhanced Thermal Conductivity of Nanofluids, *Applied Physics Letters*, 84:4316, 2004.
121. P. Keblinski, S. Phillpot and S. U. S. Choi, Mechanisms of Heat Flow in Suspensions of Nano-Sized particles (Nanofluids), *International Journal of Heat and Mass Transfer*, 45:855-863, 2002.
122. W. Yu and S. U. S. Choi, The Role of Interfacial Layers in the Enhanced Thermal Conductivity of Nanofluids: A Renovated Maxwell Model, *Journal of Nanoparticle Research*, 5:167–171, 2003.
123. K. C. Leong, C. Yang and S. M. S. Murshed, A Model for the Thermal Conductivity of Nanofluids – Effect of Interfacial Layer, *Journal of Nanoparticle Research* 8:245–254, 2006.

124. H. Q. Xie, M. Fujii and X. Zhang, Effect of Interfacial Nanolayer on the Effective Thermal Conductivity of Nanoparticle-Fluid Mixture, *International Journal of Heat and Mass Transfer*, 48:2926–2932, 2005.
125. N. Sohrabi, N. Masoumi, A. Behzadmehr and S. M. H. Sarvari, A Simple Analytical Model for Calculating the Effective Thermal Conductivity of Nanofluids, *Heat Transfer - Asian Research*, 39:141–150, 2010.
126. C. L. Altan, and S. Bucak, The effect of Fe₃O₄ Nanoparticles on the Thermal Conductivities of Various Base Fluids, *Nanotechnology*, 22:285713, 2011.
127. P. Sharma, I. Baeka, T. Chob, S. Parkc and K. B. Leed, Enhancement of Thermal Conductivity of Ethylene Glycol Based Silver Nanofluids, *Powder Technology*, 208:7–19, 2011.
128. Y. Xuan and L. Qiang, Heat Transfer Enhancement of Nanofluids, *International Journal of Heat and Fluid Flow*, 21:58-64, 2000.
129. H. A. Mintsu, G. Roy, C. T. Nguyen and D. Dominique, New Temperature Dependent Thermal Conductivity Data for Water-Based fluids, *International Journal of Thermal Sciences*, 48:363–371, 2009.
130. E. V. Timofeeva, A. N. Gavrilov, J. M. McCloskey and Y. V. Tolmachev, Thermal Conductivity and Particle Agglomeration in Alumina Nanofluids: Experiment and Theory, *Physical Reviews E*, 76:1-16, 2007.
131. L. S. Sundar, M. K. Singh and A. C. M. Sousa, Investigation of Thermal Conductivity and Viscosity of Fe₃O₄ Nanofluid for Heat Transfer Applications, *International Communications in Heat and Mass Transfer*, 44:7-14, 2013.
132. P. D. Shima, J. Philip and B. Raj, Synthesis of Aqueous and Nonaqueous Iron Oxide Nanofluids and Study of Temperature Dependence on Thermal Conductivity and Viscosity, *The Journal of Physical Chemistry C*, 114:18825-18833, 2010.

133. C. L. Altan, B. Gurten, N. A. J. M. Sommerdijk and S. Bucak, Deterioration in effective thermal conductivity of aqueous magnetic nanofluids, *Journal of Applied Physics*, 116:224904, 2014.
134. S. A. Putnam, D. G. Cahill, B. J. Ash and L. S. Schadler, High-Precision Thermal Conductivity Measurements as a Probe of Polymer/Nanoparticle Interfaces, *Journal of Applied Physics*, 94:6785-6788, 2003.
135. P. Keblinski, J. A. Eastman and D. G. Cahill, Nanofluids for Thermal Transport, *Materials Today*, 8:36-44, 2005.
136. J. Maxfield and I. W. Shepherd, Conformation of Poly (ethylene oxide) in the Solid State, Melt and Solution Measured by Raman Scattering. *Polymer*, 16:509, 1975.
137. F. Alloin, G. Hirankumar and T. Pagnier, Temperature-Dependent Raman Spectroscopy of Lithium Triflate-PEO Complexes: Phase Equilibrium and Component Interactions, *Journal of Physical Chemistry B*, 113:16465–16471, 2009.
138. C. V. Raman, A New Type of Secondary Radiation, *Nature*, 121:501, 1928.
139. D. W. Hahn, Raman Scattering Theory, Department of Mechanical and Aerospace Engineering, University of Florida,
[http://plaza.ufl.edu/dwhahn/Raman Scattering Theory.pdf](http://plaza.ufl.edu/dwhahn/Raman%20Scattering%20Theory.pdf) [retrieved 17 February 2007]
140. C. M. Snively and J. L. Koenig, Characterizing the Performance of a Fast FT-IR Imaging Spectrometer, *Applied Spectroscopy*, 53:170–177, 1999.
141. A. S. Haka, K. E. Shafer-Peltier, M. Fitzmaurice, J. Crowe, R. R. Dasari and M. S. Feld, Identifying Microcalcifications in Benign and Malignant Breast Lesions by Probing Differences in Their Chemical Composition Using Raman Spectroscopy, *Cancer Research*, 15:5375, 2002.

142. T. Vo-Dinh, K. Houck and D. L. Stokes, Surface-Enhanced Raman Gene Probes, *Analytical Chemistry*, 66:3379–3383, 1994.
143. R. Zhang, Y. Zhang, Z. C. Dong, S. Jiang, C. Zhang, L. G. Chen, L. Zhang, Y. Liao, J. Aizpurua, Y. Luo, J. L. Yang and J. G. Hou, Chemical Mapping of a Single Molecule by Plasmon-Enhanced Raman Scattering, *Nature*, 498:82–86, 2013.
144. K. Kim and K. S. Shin, Surface-Enhanced Raman Scattering: A Powerful Tool for Chemical Identification, *Analytical Sciences*, 27:775, 2011.
145. T. Yoshihara, H. Tadokoro and S. Murahashi, Normal Vibrations of the Polymer Molecules of Helical Conformation. IV Polyethylene Oxide and Polyethylene D4 oxide, *The Journal of Chemical Physics*, 41:2902, 1964.
146. G. Ćirić-Marjanović, M. Trchová and J. Stejskal, The Chemical Oxidative Polymerization of Aniline in Water: Raman Spectroscopy, *Journal of Raman Spectroscopy*, 39:1375–1387, 2008.
147. S. Parnell, K. Min and M. Cakmak, Kinetic Studies of Polyurethane Polymerization with Raman Spectroscopy, *Polymer*, 44:5137–5144, 2003.
148. M. Miyamoto, K. Naka, M. Shiozaki, Y. Chujo and T. Saegusa, Preparation and Enzymic Activity of Poly [(N-acylimino)ethylene]-Modified Catalase, *Macromolecules*, 23: 3201-3388, 1990.
149. H. W. Siesler and K. Holland-Moritz, *Infrared and Raman Spectroscopy of Polymers*, Marcel Dekker, NY, 1980.
150. D. L. Bower and W. F. Maddams, *The Vibrational Spectroscopy of Polymers*, Cambridge University Press, Cambridge, 1989.
151. A. S. Nielsen, D. N. Batchelder and R. Pyrz, Estimation of Crystallinity of Isotactic Polypropylene Using Raman Spectroscopy, *Polymer*, 43:2671-2676, 2002.

152. B. H. Stuart and B. J. Briscoe, The Effect of Crystallinity on the Scratch Hardness of Poly (ether ether ketone), *Polymer Bulletin*, 36:767-771, 1996.
153. C. H. Jones and I. J. Wesley, A Preliminary Study of the Fourier Transform Raman Spectra of Polystyrenes, *Spectrochimica Acta*, 47:1293-1298, 1991.
154. P. J. Hendra, W. F. Maddams, I. A. M. Royand, H. A. Willis and V. Zichy, The Application of Fourier-transform Raman Spectroscopy to the Identification and Characterization of Polyamides-I: Single Number Nylons, *Spectrochimica Acta*, 46A, 747, 1990.
155. P. Schmidt and P. J. Hendra, The Application of Fourier-Transform Raman Spectroscopy to the Determination of Conformation in Poly (ϵ -caprolactam) Chains, *Spectrochimica Acta Part A: Molecular Spectroscopy*, 50:1999-2004, 1994.
156. K. Schenzel, S. Fischer and E. Brendler, New Method for Determining the Degree of Cellulose I Crystallinity by Means of FT Raman Spectroscopy, *Cellulose*, 2:231, 2005.
157. Y. Takahashi and H. Tadokoro, Structural Studies of Polyethers, $-(\text{CH}_2)_m\text{-O-})_n$ X. Crystal Structure of Poly(ethylene oxide), *Macromolecules*, 6:672-675, 1973.
158. OriginLAB Corporation, "Origin 9.1: Graphing&Analysis", Northampton MA, USA, <http://www.originlab.com/> [retrieved 27 August 2014]
159. M. A. Pimenta, A. Marucci, S. A. Empedocles, M. G. Bawendi, E. B. Hanlon, A. M. Rao, P. C. Eklund, R. E. Smalley, G. Dresselhaus and M. S. Dresselhaus, Raman Modes of Metallic Carbon Nanotubes, *Physical Review B*, 58:24, 1998.
160. S. Selvasekarapandian, R. Baskaran, O. Kamishima, J. Kawamura and T. Hattori, Laser Raman and FTIR Studies on Li^+ Interaction in PVAc– LiClO_4 Polymer Electrolytes, *Spectrochimica Acta Part A.*, 65:1264, 2006.

161. H. Keles, A. Naylor, F. Clegga and C. Sammon, The Application of Non-Linear Curve Fitting Routines to the Analysis of Mid-Infrared Images Obtained from Single Polymeric Microparticle, *Analyst*, 139:2355, 2014.
162. C. Bohren and D. Huffman, *Absorption and Scattering of Light by Small Particles*, Wiley, New York, 1983.
163. U. Kreibig and M. Vollmer, *Optical Properties of Metal Clusters*, Springer-Verlag, Berlin, 1995
164. J. Cole, N. Mirin, M. Knight, G. Goodrich and N. Halas, Photothermal Efficiencies of Nanoshells and Nanorods for Clinical Therapeutic Applications, *Journal of Physical Chemistry C*, 113:12090-12094, 2009.
165. N. Harris, M. Ford and M. Cortie, Optimization of Plasmonic Heating by Gold Nanospheres and Nanoshells, *Journal of Physical Chemistry B*, 110:10701-10707, 2006.
166. K. Kelly, E. Coronado, L. Zhao and G. Schatz, The Optical Properties of Metal Nanoparticles: The Influence of Size, Shape and Dielectric Environment, *Journal of Physical Chemistry B*, 107:668-677, 2003.
167. B. Palpant, Y. Guillet, M. Rashidi-Huyeh and D. Prot, Gold Nanoparticle Assemblies: Thermal Behaviour Under Optical Excitation, *Gold Bulletin*, 41:105-115, 2008.
168. M. Daniel and D. Astruc, Gold Nanoparticles: Assembly, Supramolecular Chemistry, Quantum Size Related Properties and Applications Toward Biology, Catalysis and Nanotechnology, *Chemical Reviews*, 104:293-346, 2004.
169. E. Day, J. Morton and J. West, Nanoparticles for Thermal Cancer Therapy, *Journal of Biomechanical Engineering-Transactions of the Asme*, 131:5, 2009.

170. L. Paasonen, T. Laaksonen, C. Johans, M. Yliperttula, K. Kontturi and A. Urth, Gold Nanoparticles Enable Selective Light-Induced Contents Release from Liposomes, *Journal of Controlled Release*, 122:86-93, 2009.
171. V. Pustovalov, L. Astafyeva and B. Jean, Computer Modeling of the Optical Properties and Heating of Spherical Gold and Silica-Gold Nanoparticles for Laser Combined Imaging and Photothermal Treatment, *Nanotechnology*, 20:11, 2009.
172. A. Govorov and H. Richardson, Generating Heat with Metal Nanoparticles, *Nano Today*, 2:30-38, 2007.
173. H. Richardson, Z. Hickman, A. Govorov, A. Thomas, W. Zhang and M. Kordesch, Thermo-optical Properties of Gold Nanoparticles Embedded in Ice: Characterization of Heat generation and melting, *Nano Letters*, 6:783-788, 2006.
174. H. Richardson, A. Thomas, M. Carlson, A. Kordesch and A. Govorov, Thermo-Optical Responses of Nanoparticles: Melting of Ice and Nanocalorimetry Approach, *Journal of Electronic Materials*, 36:1587-1593, 2007.
175. M. Behl and A. Lendlein, Shape Memory Polymers, *Materials Today*, 10:20, 2007.
176. A. Hohenau, A. Leitner and F.R. Aussenegg, Near-Field and Far-Field Properties of Nanoparticle Arrays, In M.L. Brongersma and P.G. Kik, editors, *Surface Plasmon Nanophotonics*, Springer Series, Netherlands, 2007.
177. U. Kreibig and M. Vollmer, *Optical properties of metal clusters*, Springer-Verlag, Berlin, 1995.
178. D. M. Schaadt, B. Feng and E. T. Yub, Enhanced Semiconductor Optical Absorption via Surface Plasmon Excitation in Metal Nanoparticles, *Applied Physics Letters*, 86, 2005.
179. M. Blaber, M. Arnold, N. Harris, M. Ford and M. Cortie, Plasmon Absorption in Nanospheres: A Comparison of Sodium, Potassium, Aluminum, Silver and Gold, *Physica B*, 394:184-187, 2007.

180. S. Maier and H. Atwater, Plasmonics: Localization and Guiding of Electromagnetic Energy in Metal/Dielectric Structure, *Journal of Applied Physics*, 98:10, 2005.
181. A. Lendlein and S. Kelch, Shape-Memory Polymer, *Angewandte Chemie International Edition*, 41:2035-2057, 2002.
182. W. Wagermaier, K. Kratz, M. Heuchel and A. Lendlein, Characterization Methods for Shape-Memory Polymers, *Advances in Polymer Science*, 226:1-49, 2010.
183. H. Tobushi, S. Hayashi, A. Ikai and H. Hara, Thermomechanical Properties of Shape Memory Polymers of Polyurethane Series and their Applications, *Journal de Physique IV*, 6: C1-377, 1996.
184. J. Nji and G. Li, A Biomimic Shape Memory Polymer Based Self-Healing Particulate Composite, *Polymer*, 51: 6021-6029, 2010.
185. W. Small, P. Singhal, T. S. Wilson and D. J. Maitland, Biomedical Applications of Thermally Activated Shape Memory Polymers, *Journal of Materials Chemistry*, 20: 3356-3366, 2010.
186. A. Lendlein and R.S. Langer, "Self-expanding Device for the Gastrointestinal or Urogenital Area", Patent WO 2004073690 A1, 2004.
187. W. M. Huang, C. W. Lee and H. P. Teo, Thermomechanical Behavior of a Polyurethane Shape Memory Polymer Foam, *Journal of Intelligent Material Systems and Structures*, 17:753-760, 2006.
188. C. L. Altan, Chapter 1: Iron oxides and Magnetite, Biomimetic Synthesis, Magnetite Properties and Applications of Magnetite Nanoparticles, PhD Dissertation, Eindhoven University of Technology, 2014.
189. M. Y. Razzaq, M. Anhalt, L. Frommann and B. Weidenfeller, Thermal, Electrical and Magnetic Studies of Magnetite Filled Polyurethane Shape Memory Polymers, *Materials Science and Engineering*, A444:227-235, 2007.

190. J. Puig, C. E. Hoppe, L. A. Fasce, C. J. Perez, Y. Pineiro-Redondo, M. Banobre-Lopez, M. A. Lopez-Quintela, J. Rivas and R. J. J. Williams, Superparamagnetic Nanocomposites Based on the Dispersion of Oleic Acid – Stabilized Magnetite Nanoparticles in a Diglycidylether of Bisphenol A-Based Epoxy Matrix: Magnetic Hyperthermia and Shape Memory, *The Journal of Physical Chemistry*, 116:13421-13428, 2012.
191. X. Yu, S. Zhou, X. Zhen, T. Guo, Y. Xiao and B. Song, A Biodegradable Shape-Memory Nanocomposite with Excellent Magnetism Sensitivity, *Nanotechnology*, 20, 2009.
192. X. Zheng, S. Zhou, Y. Xiao, Y. Xiongjun, X. Li and P. Wu, Shape Memory Effect of Poly (D,L-lactide)/Fe₃O₄ Nanocomposites by Inductive Heating of Magnetite Particles, *Colloids and Surfaces B: Biointerfaces*, 71:67-72, 2009.
193. S. Maity, L. N. Downen, J. R. Bochinski and L. I. Clarke, Embedded Metal Nanoparticles as Localized Heat Sources: An Alternative Processing Approach for Complex Polymeric Materials, *Polymer*, 52:1674-1685, 2011.
194. K. Parker, R. T. Schneider, R. W. Siegel, R. Ozisik, J. C. Cabanelas, B. Serrano, C. Antonelli and J. Baselga, Molecular Probe Technique for Determining Local Thermal Transitions: The Glass Transition at Silica/PMMA Nanocomposite Interfaces, *Polymer*, 51:4891-4898, 2010.
195. J. M. Dixon, M. Taniguchi and J. S. Lindsey, PhotochemCAD 2. A Refined Program with Accompanying Spectral Databases for Photochemical Calculations, *Photochemistry and Photobiology*, 81:212-213, 2005.
196. M. Sauer, J. Hofkens and J. Enderlein, Chapter 1: Basic Principles in Fluorescence Spectroscopy, *Handbook of Fluorescence Spectroscopy and Imaging: From Ensemble to Single Molecules*, John Wiley & Sons, 2010.
197. R. F. Cossiello, L. Akcelrud and T. D. Z. Atvars, Solvent and Molecular Weight Effects on Fluorescence Emission of MEH-PPV, *Journal of Brazilian Chemical Society*, 16:74-86, 2005.

198. C. A. Sabatini, R. V. Pereira and M. H. Gehlen, Fluorescence Modulation of Acridine and Coumarin Dyes by Silver Nanoparticles, *Journal of Fluorescence*, 17:377-382, 2007.
199. U. S. Raikar, V. B. Tangod, B. M. Mastiholi and V. J. Fulari, Fluorescence Quenching Using Plasmonic Gold Nanoparticles, *Optics Communications*, 284:4761-4765, 2011.
200. B. M. Mastiholi, P. U. Raikar, V. B. Tangod, S. G. Kulkarni and U. S. Raikar, Fluorescence Enhancement of C 314 Laser Dye Based on ICT between C 314 Laser Dye and Green Synthesized Gold Nanoparticles, *Journal of Applied Physics*, 6:43-47, 2014.
201. R. A. Domingues, I. V. P. Yoshida and T. D.Z. Atvars, Synthesis, Photophysical Properties and Thermal Relaxation Processes of Carbazolyl-Labeled Polysiloxanes, *Journal of Photochemistry and Photobiology A: Chemistry*, 217:347-355, 2011.